Norwegian University
of Life Sciences

Master's Thesis 2022 30 ECTS
Faculty of Science and Technology

Seismic Analysis of a Multi-story Timber-Concrete Building with Focus on Reusability

Sivert Lie
Structural Engineering and Architecture

Preface

This thesis marks the completion of a Master of Science in Structural Engineering and Architecture with a specialization in Timber Engineering at the Norwegian University of Life Sciences (NMBU). The work has been challenging and educational and was motivated by a personal interest in seismic analysis, timber connections and reusability of structural elements.

I want to thank my supervisor, Associate Professor Themistoklis Tsalkatidis, for always being available, guiding me through the process using his expertise in hybrid structures and sustainable buildings. The thorough feedback every week has been invaluable. Thanks to future colleagues in Multiconsult for suggestions and information about the reference building.

Finally, I would like to thank my friends and family for the help and support to complete my master's degree. A special thanks to Rebecca for supporting me through all these years of studying, and even sticking with me the last months before delivery. This would not be possible without you.

Ås, 13th of May, 2022

Sivert Lie

Summary

The production of structural elements used in the construction industry is responsible for large parts of the global carbon dioxide production. Facilitating future reuse and implementation of reused elements should be an essential part of designing buildings. Reusing hollow core slabs is barely introduced in niche projects, but a recently published standard describes a standardized process to ensure the quality of reusable elements. By combining these with environmentally friendly materials like timber, the GHG emissions can be reduced.

This thesis investigates the dynamic behavior of an 8-story reference building designed with moment-resisting timber frames, CLT wall panels, and hollow core slabs through numerical modal analysis. In addition to pinned and rigid beam-to-column connections are four different connections from previous researches implemented in the model using rotational springs.

Results from the modal analysis show that when timber connections with low rotational stiffness are implemented, the building has a torsional mode as the fundamental mode. Two torsional modes are present when considering the number of modes necessary to reach 90% mass participation ratio in each main direction. As the rotational stiffnesses of the connections are increased, the first torsional mode is shifted to a higher frequency mode. Modal response spectrum analysis according to the Eurocode 8 is performed for all connection-cases using Complete Quadratic Combination. For a building located in a low-seismicity area, interstory drift and member capacity utilization are within limits for all connection-cases.

The reuse potential of the components in each timber connection is discussed, evaluating the complexity of the connection, and the necessary man hours to assemble and disassemble the connection. The traditional bolted connection is found to offer the highest flexibility and reuse potential.

Sammendrag

Produksjon av bærende elementer brukt i bygg- og anleggsbransjen står for store deler av den globale karbondioksidproduksjonen. Tilrettelegging for fremtidig ombruk og implementering av ombrukte elementer burde være en viktig del i prosjekteringen av bygninger. Ombruk av hulldekker er anvendt i nisjeprosjekter, men nylig publiserte standarder beskriver behandlingsprosesser som skal sikre kvaliteten av ombrukbare elementer. Kombinasjonen av disse med andre miljøvennlige materialer, som tre, kan redusere klimagassutslippene.

Denne oppgaven ser på den dynamiske oppførselen til et 8-etasjers bygg med momentstive rammer, CLT vegger og hulldekke som etasjeskiller gjennom numerisk analyse. I tillegg til rotasjonsfritt og helt momentstivt knutepunkt blir fire ulike bjelke-søyle forbindelser fra tidligere forskning implementert i modellen og undersøkt ved bruk av rotasjonstive fjærer.

Resultatene viser at når forbindelser med lav rotasjonsstivhet implementeres i modellen er byggets første mode en torsjonsmode. Ved oppnåelse av 90% modal masse i de to globale hovedretningene er to torsjonsmoder innkludert. Ved å øke rotasjonsstivheten flyttes første torsjonsmode fra første mode til moder med høyere frekvens. Modal respons spektrum analyse etter Eurokode 8 er gjennomført for alle situasjoner ved bruk av komplett kvadratisk kombinasjon. For en bygning i områder med lav seismisk aktivitet er verken forskyvningene i bygget eller kapasiteten til elementene overskridet for alle forbindelsene.

Ombrukspotensialet til komponentene i alle forbindelsene er diskutert, og en evaluering av kompleksiteten og arbeidstimer knyttet til montering og demontering av forbindelsen er gjort. Den tradisjonelle boltede forbindelsen tilbyr størst fleksibilitet og høyest ombrukspotensiale.

Table of Contents

List of Figures

List of Tables

List of Abbreviations and Symbols

Abbreviations

AB	Angle Bracket
AD	Absolute drift
ALS	Accidental limit state
BX	Beam having its main direction in approximately global X-direction
BY	Beam having its main direction in approximately global Y-direction
CLT	Cross Laminated Timber
CM	Center of Mass
CNC	Computer Numerical Controlled
COR	Center of rotation
CQC	Complete Quadratic Combination
DCH	Ductility class high
DCL	Ductility class low
DCM	Ductility class medium
EC0	NS-EN 1990 Eurocode 0: Basis of structural design
EC1	NS-EN 1991 Eurocode 1: Actions on structures - Part 1-1: General actions - Densities, self-weight, imposed loads for buildings
EC1-1-3	NS-EN 1991-1-3 Eurocode 1: Actions on structures - Part 1-3: General actions - Snow loads
EC1-1-4	NS-EN 1991-1-4 Eurocode 1: Actions on structures - Part 1-4: General actions - Wind actions
EC2	NS-EN 1992 Eurocode 2: Design of concrete structures
EC3	NS-EN 1993 Eurocode 3: Design of steel structures
EC4	NS-EN 1994 Eurocode 4: Design of composite steel and concrete structures

EC5	NS-EN 1995 Eurocode 5: Design of timber structures
EC8	NS-EN 1998 Eurocode 8: Design of structures for earthquake resistance
EWP	Engineered Wood Product
FEM	Finite element method
FRP	Fibre Reinforced Polymers
GHG	Greenhouse gasses
GLT	Glued Laminated Timber
HCS	Hollow Core Slabs
HDB	Hold-down Bracket
ID	Interstory drift
KD	Center of rigidity
KS	Center of rotation
$M_{\mathrm{Eff.Rz}}$	Mass Participation Ratio about global Z
$M_{\mathrm{Eff.Ux}}$	Mass Participation Ratio in Global X
$M_{\mathrm{Eff.Uy}}$	Mass Participation Ratio in Global Y
MDOF	Multi Degree of Freedom
MRSA	Modal Response Spectrum Analysis
NLA	Non-linear analysis
PSA	Pseudo-acceleration
RHCS	Reused Hollow Core Slabs
SDOF	Single Degree of Freedom
TCC	Timber-concrete composite

Greek Symbols

β	Frequency ratio
ω_D	Damped natural frequency
ω_n	Natural frequency
$\bar{\boldsymbol{\epsilon}}$	Corresponding virtual strains
$\boldsymbol{\phi}$	Mode shape matrix
$\boldsymbol{\phi}_{i.\theta}$	Torsional mode shape matrix
$\boldsymbol{\phi}_{i.x}$	Mode shape matrix in X
$\boldsymbol{\phi}_{i.y}$	Mode shape matrix in Y
$\psi_{E,i}$	Combination factor for variable actions in seismic loading

φ	Modification factor for variable actions
ζ	Damping ratio

Other Mathematical Symbols

$\mathbf{C}$	Damping matrix for MDOF system
$\mathbf{K}$	Stiffness matrix for MDOF system
$\mathbf{M}$	Mass matrix for MDOF systems
$\mathbf{Q_c}$	Transformation matrix for axial threaded rods in column
$\bar{\boldsymbol{U}}$	Virtual displacements
A_c	Cross sectional area of column in shear
a_g	Design ground acceleration
b_c	Width of the column under compression
d_1	Core diameter of an embedded rod
d_{net}	Diameter in free length a rod
E	Modulus of elasticity
E_{90}	Modulus of elasticity perpendicular to grain
EI_b	Flexural rigidity
F_b	Base shear force
$F_{ax.Rk}$	Withdrawal capacity of the fastener
$f_{h.k}$	Characteristic embedment strength of the timber
G_w	Shear modulus of column
h_c	Depth of GLT column
h_r	Distance from bolt row to center of compression
I	Moment of inertia
$I_{\theta.i}$	Moment of inertia of floor segment
K_c	Compressive stiffness of connection
k_c	Initial compressive stiffness
K_t	Tensile stiffness of connection
k_t	Initial tensile stiffness
K_u	Fastener Ultimate Slip modulus
k_v	Foundation modulus of laterally loaded rod
K_{bc}	Stiffness of glulam beam in compression
K_{cc}	Transverse stiffness of glulam column

K_{CF}	Bearing stiffness of column face
K_{cs}	Shear stiffness of glulam column
$K_{eff,r}$	Effective stiffness of bolt row
K_{HB}	Hollo-bolt axial stiffness
K_{srtc}	Initial stiffness of steel box
$l_{cc,eff}$	Effective length of the area under compression of the GLT column
m_i	Mass of floor segment
$M_{y.Rk}$	Characteristic yield moment of the fastener
q	Behavior factor
R_i	Radius from CM of the segment to CM of the floor
r_i	Distance from center of rotation to fastener
S	Soil factor
$S_d(T)$	Design spectrum
$S_e(T)$	Elastic horizontal ground acceleration spectrum
$S_{De}(T)$	Elastic displacement spectrum
$S_{xx/yy}$	Compliance terms representing stiffness in global coordinates
T_1	Fundamental period
t_1	Thickness of the connected timber
T_B	Lower limit of the constant spectral acceleration branch
T_C	Upper limit of the constant spectral acceleration branch
T_D	Damped natural period
T_D	Value defining the beginning of constant range of the spectrum
T_n	Natural period
z_{eq}	Equivalent lever arm

1. Introduction

1.1 Background

The construction industry and the production of structural elements play a huge part in global carbon dioxide (CO_2) production (Ghayeb et al., 2020). To limit the increasing global temperature due to greenhouse gasses (GHG), the reuse of structural elements should become an essential part of an engineer's daily practice. While being a big part of the building's mass (Eberhardt et al., 2018), Peretti et al. (2019) found that the use of emerging or innovative materials for structural elements is generally considered harder than for other parts of the building. Thus, increasing the knowledge around this field is necessary to enhance sustainability in the industry and introduce standard procedures of designing for this cause.

Ghayeb et al. (2020) state that the production of new materials has significantly influenced the CO_2 emissions when constructing new buildings. de Castilho et al. (2005) present a yearly production of 150 million cubic meters of new Hollow Core Slabs (HCS) on average, and if reused HCS could replace even a small portion of these, it would be positive for the reduction in CO_2 production. Huuhka et al. (2015) highlight the importance of seeing buildings already built as reserves for resources to reduce the amount of waste produced when demolishing it to build new buildings. BEF (2011b) indicates that HCS are the most commonly used element as floor for new buildings in Norway, and reused HCS are barely introduced in niche projects. The recent publishing of *NS 3682:2022 Hulldekker av betong til ombruk* (Hollow core slabs for reuse) introduces a standardized handling process of HCS for reuse, and is an important step for large scale implementation.

The concept of designing a building to be disassembled in the future is a crucial factor in the development of sustainable buildings. By combining this concept with sustainable materials like reused HCS and timber elements, the GHG emissions from the construction industry can be reduced. The most crucial factor in the design process is that the building and its components must possess quality and reliability. This includes durability in seismic-prone areas, as the concept should be applicable worldwide. The lack of standardized procedures regarding reusable elements are limiting the broad implementation of the concept.

1.2 Scope

This thesis investigates the concept of designing buildings for reusability and the aspect of seismic design in the European Standard through the following research questions:

- How does the dynamic response vary with the type of timber connection and the level of demountability?
- How does a building designed by the concept of reusable structural elements comply with the European Standard for earthquake loadings?
- How can a building be designed by utilizing reused elements and the concept of designing for future reuse?

1.3 Limitations

This thesis aims to investigate the dynamic behavior of a multi-story timber-concrete building subjected to earthquake according to EC8. As the reference building is located in Oslo, input values related to this location are used.

In addition to two reference cases, there are four beam-to-column connections implemented in the numerical model. The selection of connections was done in early phase and connections with different geometry and properties were desirable. Thorough investigation of each connection was prioritized over increasing the number of connections. The same dimensions of structural elements are used for all cases in order comparable results.

2. State-of-the-Art

This chapter describes the State-of-the-Art, including the general practice of modular building, the widespread of this phenomenon and areas where research is lacking.

2.1 Multi-story modular buildings

The concept of modular buildings is introduced in this section, the advantages and disadvantages of the process, and the opportunities that lies within this field and method of construction.

2.1.1 Concept of modular buildings

Modular buildings consist of off-site manufactured structural elements, called modules, often made in factories. The elements are then transported to a construction site and assembled into a complete building structure. This form of construction is well established for low-rise buildings, and utilizing the strategy for high-rise buildings has been adopted (Ferdous et al., 2019). Among the earliest examples of modular buildings is the Building of Crystal Palace in Great Britain in mid 19th century, which was constructed in a few months (Velamati, 2012). Lawson et al. (2012) highlight the economic benefits of scale in manufacturing multiple equal units with the added quality of the product, speed of installation on-site, and the possibility of dismantling the elements for future reuse. The same authors found a potential of 70% reduction in landfills when modular construction is used.

2.1.2 Drawbacks for modular building

Memari and Ramaji (2013) identify several issues with modular buildings and highlight that these problems become more complicated for multi-story than low-rise buildings. The lack of specific codes for modular buildings and the unique behavior of each type of modular building causes new challenges when predicting the behaviour under structural loads.

Multi-story buildings require lateral loads resisting systems for wind, earthquake, or other accidental loads. The parameters affected by the materials in the buildings become significant in the non-linear design. This includes joints designed to plastify and dissipate seismic energy. Different behavior is based on this expected, caused by additional flexibility in a modular system than in a traditional non-modular building (Memari and Ramaji, 2013).

2.2 Hybrid buildings

This section introduces the general concept of hybrid buildings, the range of applications, and a particular focus on buildings consisting of both timber and concrete. The material differences are highlighted and some benefits and disadvantages are presented.

2.2.1 Introduction

The general idea of hybrid structures is based on utilizing the strengths of different materials to improve the overall performance of the structure (Tesfamariam and Stiemer, 2014). The concept of hybrid buildings has been for a long time. There are traces of using hybrid structures consisting of timber frames with masonry infill back in ancient Rome (Bağbanci and Bağbanci, 2018), called *Ottoman House* by Porcu (2017).

Morino (1998) classifies hybrid structures into five groups: hybrid members, hybrid assemblages, hybrid systems, half precast, and other constructions. Pan et al. (2021) highlight that the traditional composite high-rise buildings consist of steel and concrete.The guidelines for this type of building are well established, e.g., *NS-EN 1994 Eurocode 4: Design of composite steel and concrete structures*. The combination of a need to reduce GHG emissions and the rapid population increase requires constructing high-rise buildings with more environmentally friendly materials like timber.The standardization of hybrid buildings combining materials materials than steel and concrete is lacking.

Figure 2.1 shows two projects from modern times using hybrid structures. Brock Commons in Vancouver, Canada, in Figure 2.1a, consists of a mass timber construction and two concrete stair cores. A Working Lab in Gothenburg, Sweden, seen in Figure 2.1b, consists of timber floor and columns in addition to steel beams.

(a) Brock Commons, Vancouver, Canada. Mass timber building with concrete stair core (Think Wood, 2020).

(b) A Working Lab, Gothenburg, Sweden. Steel beams, timber floor, and timber columns (Efterklang, 2021).

Figure 2.1: Examples of modern modular and hybrid buildings.

2.2.2 Timber-concrete buildings

Timber-concrete composites have been of interest for a long time, and light-frame wood buildings with or without infill have shown significant resistance in earthquake prone areas due to different factors, like high lateral resistance (Bağbanci and Bağbanci, 2018) or ductility of nail fasteners (Pan et al., 2021).

Pan et al. (2021) highlight that requirements for high-rise buildings introduce the hybridization of wood to combine the advantagess of different materials. This can be done on two levels: *component level*, such as steel-GLT columns, or *system level*, such as CLT shear walls with steel frames. The research on the combination of timber and concrete on system level is reported by Gallo et al. (2021) to be relatively low. It is highlighted that the connection of concrete to timber must be constructed carefully, as several studies found this to be a weak spot.

2.2.3 Material properties

Traditionally, timber has often been considered weaker than reinforced concrete and steel. The introduction of processed timber elements, as GLT and CLT are, makes timber applicable for high-rise buildings. When compared to concrete, GLT and CLT are comparable to pure concrete in compression, and the strength-to-weight ratio in tension is comparable to steel. In recent years, the process of *delignification* has introduced timber products with a significantly higher capacity in both tension and compression, up to 225 MPa (Gallo et al., 2021).

When constructing with timber, Gallo et al. (2021) highlight that the dissipation of seismic energy is different in timber than in steel or reinforced concrete, as timber is a brittle material. This leads to energy dissipation in the connections between timber elements instead of in critical zones of the structural element itself, as is done when designing with steel or reinforced concrete. The yielding of steel or reinforced concrete to dissipate energy often leads to irreparable damage.

The introduction of lightweight timber flooring systems in hybrid buildings makes wind the governing design load rather than earthquake loadings (Tesfamariam and Stiemer, 2014). The same concept applies to hybrid buildings consisting of processed timber elements, as the earthquake loading is directly proportional to the mass of the building (Pan et al., 2021).

Memari and Ramaji (2013) highlight the importance of accounting for eccentricities and providing flexibility to the system by adding tolerance and allowance in the design. This includes considering internal forces in the modules or increasing safety factors. Marzaleh et al. (2018) list several reasons causing problems for concrete-timber buildings, including differences in tolerance for timber and concrete. This tolerance is mainly because GLT beams are cut with a Computer Numerical Controlled (CNC)-machine, giving a tolerance of $\pm mm$, while HCS are produced with a tolerance of $\pm cm$ (Ballast, 2007).

2.3 Hollow core Slabs

Hollow Core Slabs (HCS) are precast structural units produced off-site and mainly consisting of concrete. HCS can be produced various heights and lengths, making them applicable for a broad range of buildings. As seen in Figure 2.2, the slabs are hollow, making them lighter than traditional on-site casted concrete. The holes can be of different shapes, e.g., round, pseudo ellipsis, rectangular, and the standard width of an element is 120 cm (de Castilho et al., 2005). The slabs are traditionally reinforced with steel rebars in the bottom part, which can have an initial tension creating compression in the HCS (Al-Shaarbaf et al., 2018). After the HCS are mounted, a concrete topping can be applied, with or without reinforcement (Chang et al., 2006). This topping is not required for the flooring system to be considered a rigid diaphragm (Memari and Ramaji, 2013).

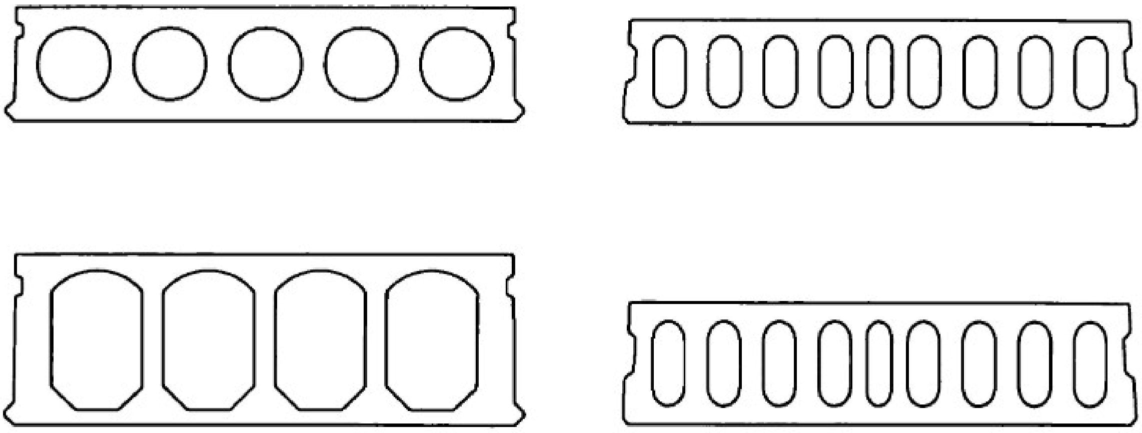

Figure 2.2: Example of HCS sections (de Castilho et al., 2005).

2.3.1 Process of installation

When erecting a building with HCS as the separating floor, the precasted HCS are delivered to the construction site and elevated into their place (Buettner et al., 1998). The process can be seen in Figure 2.3, where the elements produced in factories are transported to the construction site and elevated into its place.

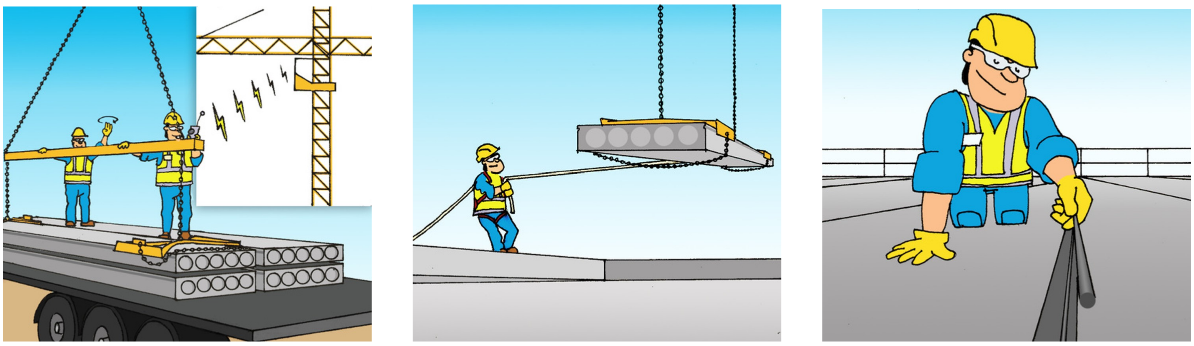

(a) Transported elements **(b)** Elevation of HCS. **(c)** Rebar placed in lateral void.

Figure 2.3: Process of installing HCS (BEF, n.d.).

A vital part of the mounting is the shear infill in the lateral void, seen in Figure 2.4, and the interconnection with the transverse resisting connection, seen in Figure 2.5. These infills are traditionally cement-based grout with steel rebars, cast on-site, ensuring that shear forces are resisted, as described in Section 3.3.3. This is one of the main reasons that disassembling a building so that elements are reusable is difficult (Volkov, 2019).

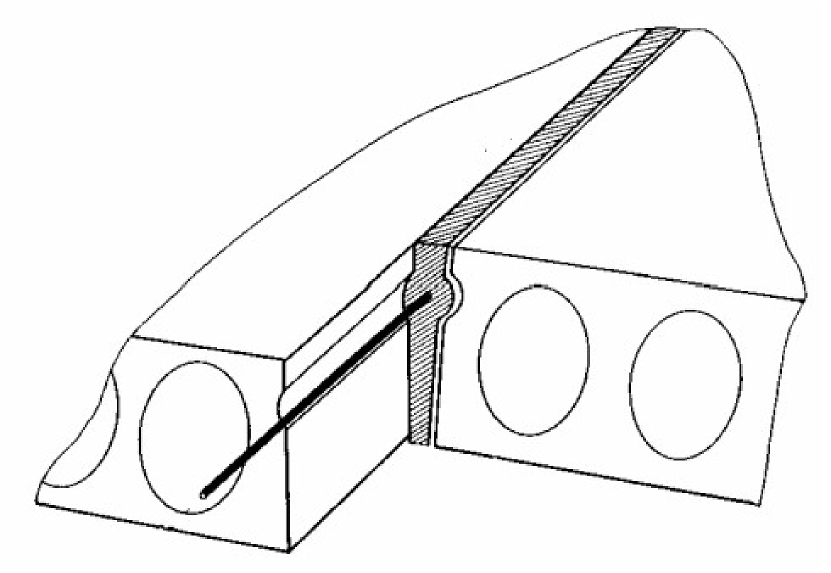

Figure 2.4: Lateral void filled with grout with longitudinal steel rebar (Engström et al., 2008).

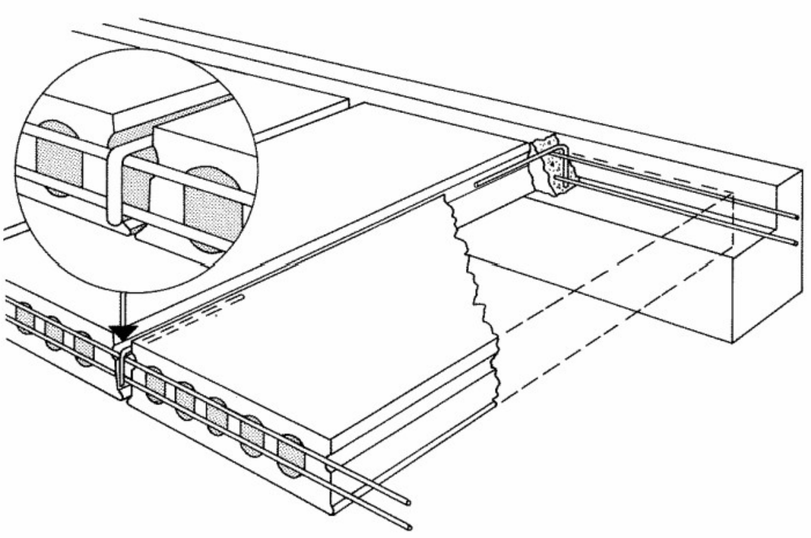

Figure 2.5: Connection of longitudinal rebars with transverse resisting steel rebars, voids filled with grout (Engström et al., 2008).

3. Theory

The following chapter describes the theory creating the base for the method of analysis. A general part, including the response of structural systems and the different aspects of an earthquake as a phenomenon, is presented before research regarding experimental results and numerical modeling of structural elements and components are described in detail.

3.1 Structural Dynamics

This section describes the different aspect of structural dynamics in civil engineering and presents factors that influence the response of buildings subjected to dynamic loadings.

3.1.1 Introduction

To analyze the dynamic response of structural buildings, a mathematical approach can describe both the exciting forces and the structure's response. The structure can be either a Single Degree of Freedom (SDOF)- or a Multi Degree of Freedom (MDOF)-system, and the response will be affected by several factors, such as stiffness, damping, or ductility.

3.1.2 Response of a vibrating system

A vibrating system can be generalized into two main categories; *free* and *forced* vibration. Free vibration means that no external forces are applied to the system, while forced vibration indicates that external forces are present and influence the system during vibration. For both cases, the system is either classified as *undamped* or *damped*, indicating if a viscous damping component is present or not. Viscous damping means that the damping rate is dependent on the velocity of the vibrating mass (Chopra, 2012).

A general equation for a system vibrating can be found by applying Newton's law of motion. From Figure 3.1, assuming the mass m has no stiffness or damping, the damping c has no mass or stiffness and the spring k has no mass or damping, the equation of motion (EOM) for the simplified SDOF-system subjected to an external force $p(t)$ can be expressed as:

$$m\ddot{u}(t) + c\dot{u}(t) + ku(t) = p(t) \tag{3.1}$$

This equation is valid for any $t > 0$.

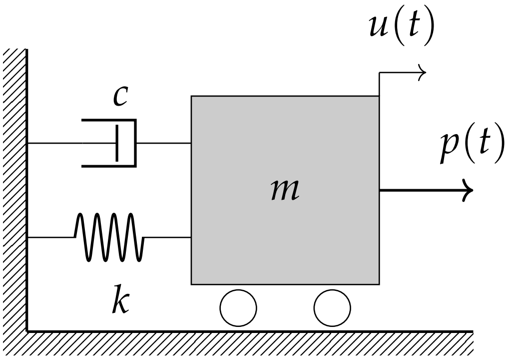

Figure 3.1: Simplified mass-spring-damper SDOF-system.

The natural frequency ω_n is defined by Chopra (2012) as:

$$\omega_n = \sqrt{\frac{k}{m}} \tag{3.2}$$

and the natural period T_n is defined as:

$$T_n = \frac{2\pi}{\omega_n} \tag{3.3}$$

The damping ratio ζ is defined as:

$$\zeta = \frac{c}{2m\omega_n} = \frac{c}{c_{cr}} \tag{3.4}$$

where c_{cr} is the critical damping coefficient. This is the smallest value of damping coefficient c that prevents a full oscillation cycle (Chopra, 2012).

3.1.2.1 Damped forced vibration

For a damped forced vibration, the solution to Eq. (3.1) is assumed to consist of two parts, a homogeneous solution $u_h(t)$ and a particular solution $u_p(t)$ (Chopra, 2012).

$$u(t) = u_h(t) + u_p(t) \tag{3.5}$$

The homogeneous solution is equal to the damped free vibration response given by Cook et al. (2002), who suggest that the structural damping ratio is typically $\zeta < 0.15$, and further theory is therefore restricted to the underdamped case. The homogeneous solution in Eq. (3.5) can be assumed to be:

$$u(t) = e^{-\zeta \omega_n t}(A\cos(\omega_D t) + B\sin(\omega_D t)) \tag{3.6}$$

where ω_D is the damped natural frequency and is defined as:

$$\omega_D = \omega_n \sqrt{(1-\zeta^2)} \tag{3.7}$$

The damped natural period is given by:

$$T_D = \frac{2\pi}{\omega_D} \tag{3.8}$$

Following the fact that structural damping is relatively small, we can see that $\omega_D \approx \omega_n$. Comparing the two natural periods, T_n and T_D, it can be seen that the damped natural period is lengthened with a factor of T_n/T_D (Cook et al., 2002).

The particular solution of Eq. (3.5) i assumed to be:

$$u_p(t) = C\sin(\omega t) + D\cos(\omega t) \tag{3.9}$$

Expressions for C and D can be found by differentiating Eq. (3.5) twice to find $\ddot{u}(t)$ and $\dot{u}(t)$ and substituting into Eq. (3.1). This leads to the following expressions for C and D:

$$C = \frac{p_0}{k}\frac{1-\beta^2}{[1-\beta^2]^2 + [2\zeta\beta]^2} \tag{3.10}$$

$$D = \frac{p_0}{k}\frac{-2\zeta\beta^2}{[1-\beta^2]^2 + [2\zeta\beta]^2} \tag{3.11}$$

This leads to the total solution for a damped forced vibration, where A and B can be found by applying the initial conditions u_0 and $\dot{u}_0$.

$$u(t) = \underbrace{e^{-\zeta\omega_n t}\,(A\cos(\omega_D t) + B\sin(\omega_D t))}_{\text{transient}} + \underbrace{C\sin(\omega t) + D\cos(\omega t)}_{\text{steady state}} \tag{3.12}$$

Chopra (2012) separates the two parts of the solution. The response due to free vibration becomes negligible after a while due to the negative exponential, while the steady state response is due to the external excitation and will remain. An important notice is that the maximum deformation peak may occur before the vibration has reached its steady state, as seen in Figure 3.2

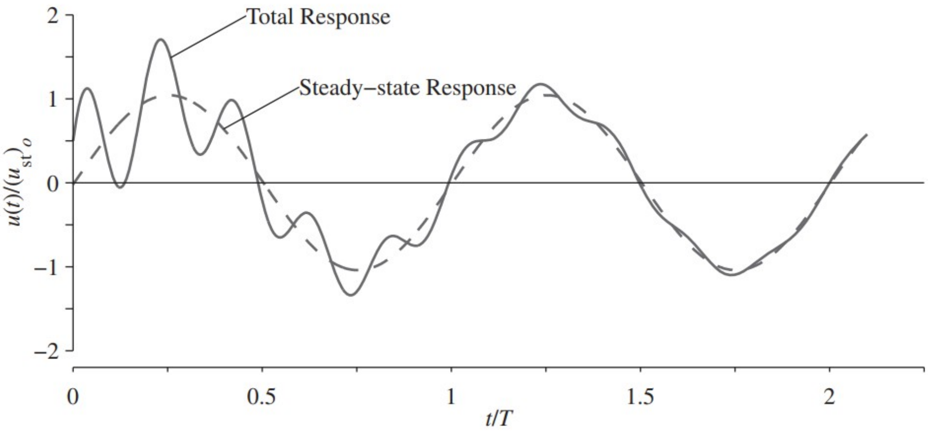

Figure 3.2: Response of damped system subjected to harmonic force, $\beta = 0.2$, $\zeta = 0.05$, $u_0 = 0.5p_0/k$ and $\dot{u}_0 = \omega_n p_0/k$ (Chopra, 2012).

When $\omega = \omega_n$, the damping factor ζ becomes crucial. If the frequency ratio $\beta = 1$, Eq. (3.10) gives $C = 0$ and Eq. (3.11) gives $D = -(u_{st})_0/2\zeta$. If the system is initially at rest, $u_0 = \dot{u}_0 = 0$, and from Eq. (3.12) this gives $A = (u_{st})_0/2\zeta$ and $B = (u_{st})_0/2\sqrt{1-\zeta^2}$. Inserting all constants A, B, C & D in Eq. (3.12) gives the total solution for a damped forced vibration at resonance (Chopra, 2012):

$$u(t) = (u_{st})_0 \cdot \frac{1}{2\zeta}\left[e^{-\zeta\omega_n t}\left(\cos(\omega_D t) + \frac{\zeta}{\sqrt{1-\zeta^2}}\sin(\omega_D t)\right) - \cos(\omega_n t)\right] \tag{3.13}$$

Chopra (2012) describes that for low damping ratios, the sinusoidal component in Eq. (3.13) is small, and the damped natural frequency $\omega_D \approx \omega_n$. This leads to the simplified response function for a damped forced vibration when $\omega = \omega_n$:

$$u(t) \simeq \underbrace{\frac{(u_{st})_0}{2\zeta}\left(e^{-\zeta\omega_n t} - 1\right)}_{envelope function}\cos(\omega_n t) \tag{3.14}$$

The envelope function in Eq. (3.14) gives the amplitude of the function. When $t \to \infty$, the envelope limits the response to the steady state amplitude, defined as:

$$u_0 = \frac{(u_{st})_0}{2\zeta} \tag{3.15}$$

The steady state amplitude's rate is attained strongly dependent on the damping ratio ζ. As seen in Figure 3.3, a lower damping ratio increases the size of the amplitude and the number of periods T_n completed before reaching steady state vibration (Chopra, 2012).

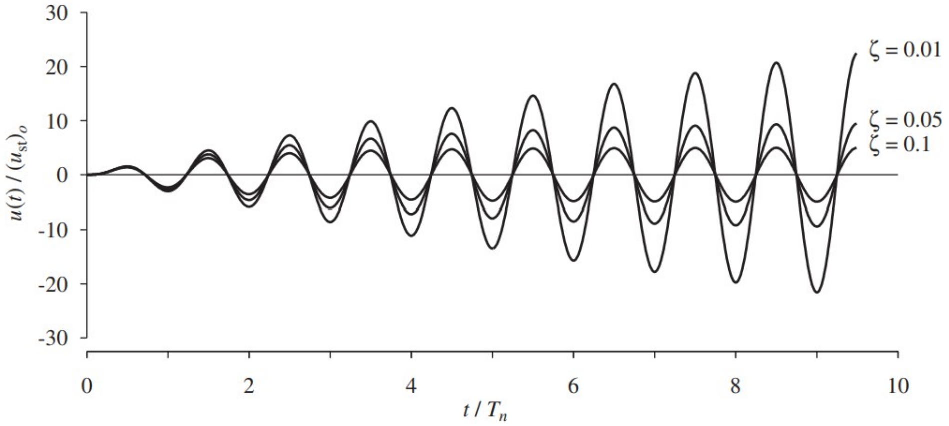

Figure 3.3: Response of three damped systems subjected to harmonic force, $\beta = 1$, $u_0 = \dot{u}_0 = 0$ (Chopra, 2012).

3.1.3 External force

The external force $p(t)$ that the system vibrating is subjected to can be an initial force, a periodic force harmonically varying with time, an impulse loading or an arbitrary excitation. In each case, and especially for the three latter cases, a mathematical approach is needed to convert the complex excitation to find the response of the system.

3.1.3.1 Static force

When a system is subjected to static force, it can be converted to initial displacement. This displacement is found by applying Hooke's law for springs, where in Eq. (3.16), F refers to the force, Δx refers to the displacement caused by the force, and k is a coefficient that represents the stiffness of the spring, as seen in Figure 3.4. The stiffness coefficient for a civil structure can be found using geometrical and material properties.

$$F = -k \cdot \Delta x \tag{3.16}$$

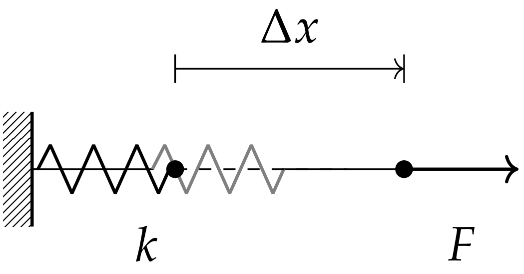

Figure 3.4: Hooke's law for a simple spring.

3.1.3.2 Periodic excitation

Exciting forces varying with time can be described as a sum of harmonic functions with respect to time using *Fourier series*. Chopra (2012) describes the method to do this conversion for any periodic function $p(t)$ with period T_0 if the function satisfies the following relationship:

$$p(t + nT_0) = p(t) \quad n \in \langle -\infty, \infty \rangle$$

If the function satisfies this relationship, Fourier series can be applied to separate the function into its harmonic components:

$$p(t) = a_0 + \sum_{n=1}^{\infty} a_n \cos(n\omega_0 t) + \sum_{n=1}^{\infty} b_n \sin(n\omega_0 t) \tag{3.17}$$

The components can be expressed in terms of $p(t)$ since sine and cosine are orthogonal:

$$a_0 = \frac{1}{T_0} \int_0^{T_0} p(t)dt \tag{3.18}$$

$$a_n = \frac{2}{T_0} \int_0^{T_0} p(t) \cos(n\omega_0 t)dt \tag{3.19}$$

$$b_n = \frac{2}{T_0} \int_0^{T_0} p(t) \sin(n\omega_0 t)dt \tag{3.20}$$

Where a_0 is the average value of the function, a_n and b_n are the amplitudes of the nth harmonic of the frequency $n\omega_0$. ω_0 is the frequency of the fundamental harmonic frequency (Chopra, 2012).

$$\omega_0 = \frac{2\pi}{T_0} \tag{3.21}$$

Theoretically, Fourier series will converge to $p(t)$ when the number of terms $n \to \infty$. Chopra (2012) highlights that in practice, a few terms are required to represent the function sufficiently. At points of discontinuity, the approximation converges to a value that is the average of values immediately to the right and left of the point of discontinuity.

3.1.3.3 Arbitrary excitation

If the force $p(t)$ varies arbitrarily with respect to time, Chopra (2012) represented the function as a sequence of infinite small impulses, where each impulse force $p(t) = 1/\epsilon$ starting at the time instant $t = \tau$ and with a duration of $\epsilon \to 0$. The *Dirac delta function* $\delta(t - \tau)$ mathematically defines a unit impulse centered at $t = \tau$, leading to the *unit impulse-response function* denoted by $h(t - \tau)$. If this exciting impulse force is ground motion, the function can be expressed as (Chopra, 2012):

$$h(t-\tau) = -\frac{1}{\omega_D} e^{-\zeta\omega_n(t-\tau)} \sin(\omega_d(t-\tau)) \tag{3.22}$$

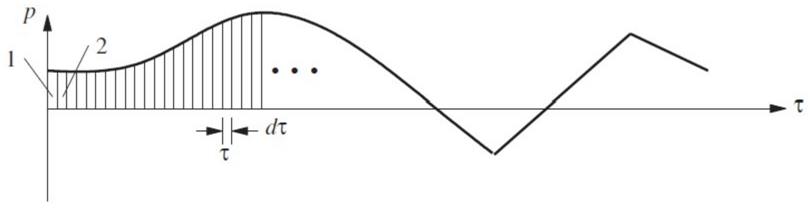

Figure 3.5: Arbitrary force function $p(t)$ represented by short impulses with duration of $d\tau$ at $t=\tau$.

The response $u(t)$ of the system when the arbitrary force seen in Figure 3.5 can be expressed by *Duhamel's integral*:

$$u(t) = \frac{1}{m\omega_D} \int_0^t p(\tau) e^{\zeta\omega_n(t-\tau)} \sin(\omega_D(t-\tau)) d\tau \tag{3.23}$$

It is highlighted by Chopra (2012) that this general results is only valid for linear systems as it is based on the principle of superposition. If $p(\tau)$ is a complicated function, a numerical evaluation of the integral is required.

3.1.4 Single degree of freedom structural systems

The structural system shown in Figure 3.6 can be assumed as an idealization of a one-story structure, where the properties mentioned in Section 3.1.2 are concentrated in three pure components: the mass component, representing the mass of the structure as a lumped mass, the stiffness component is representing the lateral stiffness of the structural members, and the damping component, representing damping in the structure caused by material damping, friction or other energy absorbing quantities (Chopra, 2012).

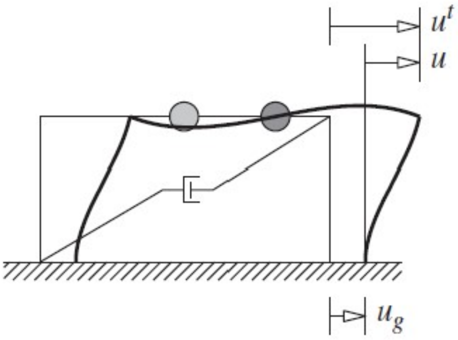

Figure 3.6: Idealized system with earthquake-induced motion.

The simplified structural system can be solved in the same manner as the mass-spring-damper system shown in Section 3.1.2, assuming that the frame moves only in the direction of the exciting force. From the solution presented in Eq. (3.12), $u(t)$ here represents the relative displacement between the mass and the ground (Chopra, 2012).

3.1.5 Multi degree of freedom structural systems

An idealized two-story shear frame with infinite rigid beams subjected to external forces is the simplest Multi Degree of Freedom (MDOF) system . It can be used to illustrate the EOM for MDOF systems. The mass is concentrated in the floor levels, and viscous damping is assumed. As seen in Figure 3.7, the displacements of each floor u_1 and u_2 are the only degrees of freedom when the beam rotation is neglected (Chopra, 2012).

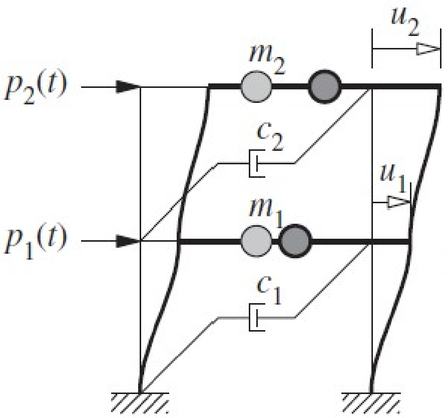

Figure 3.7: Simplified two-story frame considered as a MDOF system (Chopra, 2012).

Using Newton's second law of motion and the same procedure as for SDOF-systems, a matrix formulation is necessary to represent the EOM for the simplified system shown in Figure 3.7.

$$\begin{bmatrix} m_1 & 0 \\ 0 & m_2 \end{bmatrix} \cdot \begin{Bmatrix} \ddot{u}_1 \\ \ddot{u}_2 \end{Bmatrix} + \begin{bmatrix} c_1 + c_2 & -c_2 \\ -c_2 & c_2 \end{bmatrix} \cdot \begin{Bmatrix} \dot{u}_1 \\ \dot{u}_2 \end{Bmatrix} + \begin{bmatrix} k_1 + k_2 & -k_2 \\ -k_2 & k_2 \end{bmatrix} \cdot \begin{Bmatrix} u_1 \\ u_2 \end{Bmatrix} = \begin{Bmatrix} p_1(t) \\ p_2(t) \end{Bmatrix} \tag{3.24}$$

For a MDOF system with n floors that is being subjected to the base excitation $\ddot{u}_g$ in the direction of $\mathbf{r}$, the response can be describe by the following equation from Ψυχάρης (2016):

$$\mathbf{M}\ddot{\mathbf{u}} + \mathbf{C}\dot{\mathbf{u}} + \mathbf{K}\mathbf{u} = -\mathbf{M}\mathbf{r}\ddot{x}_g \tag{3.25}$$

The displacement vector $\mathbf{u}$ for these equations consists of $3 \cdot n$ components:

$$\mathbf{u} = \{\underbrace{u_{1.x} \quad u_{1.y} \quad \theta_1}_{1st floor} \quad \underbrace{u_{2.x} \quad u_{2.y} \quad \theta_2}_{2nd floor} \quad \dots \quad \underbrace{u_{n.x} \quad u_{n.y} \quad \theta_n}_{nth floor}\}^T \tag{3.26}$$

In Eq. (3.25), $\mathbf{M}$ is a diagonal matrix consisting of three sub-matrices $\mathbf{m_x}$, $\mathbf{m_y}$ and $\mathbf{I_\theta}$:

$$\mathbf{M} = \begin{bmatrix} \mathbf{m_x} & 0 & 0 \\ 0 & \mathbf{m_y} & 0 \\ 0 & 0 & \mathbf{I_\theta} \end{bmatrix} \tag{3.27}$$

$$\mathbf{m_x} = \begin{bmatrix} m_{1.x} & 0 & . & 0 \\ 0 & m_{2.x} & . & 0 \\ . & . & \ddots & \vdots \\ 0 & 0 & 0 & m_{n.x} \end{bmatrix} \mathbf{m_y} = \begin{bmatrix} m_{1.y} & 0 & . & 0 \\ 0 & m_{2.y} & . & 0 \\ . & . & \ddots & \vdots \\ 0 & 0 & 0 & m_{n.y} \end{bmatrix} \mathbf{I_\theta} = \begin{bmatrix} I_{1.\theta} & 0 & . & 0 \\ 0 & I_{2.\theta} & . & 0 \\ .. & . & \ddots & \vdots \\ 0 & 0 & 0 & I_{n.\theta} \end{bmatrix} \tag{3.28}$$

where

$m_{i.x}$ and $m_{i.y}$ are the masses in x- and y-direction, respectively. Normally, $m_{i.x} = m_{i.y}$

I_θ is the moment of inertia of the floor with respect to the vertical axis through center of mass (CM)

$\mathbf{I}_\theta$ for a regular building of dimensions L_xxL_y is expressed by Ψυχάρης (2016):

$$I_\theta = \frac{m \cdot \left(L_x^2 + L_y^2\right)}{12} \tag{3.29}$$

while for an irregular building, each floor should be divided into several segments with a moment of inertia with the radius R_i from the vertical axis trough CM, leading to the following expression:

$$I_\theta = \sum_i I_{\theta.i} + \sum_i m_i \cdot R_i^2 \tag{3.30}$$

where

$I_{\theta.i}$ for each floor segment is calculated by Eq. (3.29)

m_i is the mass of the floor segment

R_i is the radius from center of mass of the segment to center of mass of the whole floor

The stiffness matrix **K** and damping matrix **C** in Eq. (3.25) consist of sub-matrices in the same manner as **M**, where each sub-matrix describes the stiffness and damping, respectively, in each direction. The stiffness matrix is defined by $\Psi\upsilon\chi\acute{\alpha}\rho\eta\varsigma$ (2016) as:

$$\mathbf{K} = \begin{bmatrix} \mathbf{k}_x & \mathbf{k}_{xy} & \mathbf{k}_{x\theta} \\ \mathbf{k}_{xy} & \mathbf{k}_y & \mathbf{k}_{y\theta} \\ \mathbf{k}_{x\theta} & \mathbf{k}_{y\theta} & \mathbf{k}_\theta \end{bmatrix} \tag{3.31}$$

The damping matrix is defined as:

$$\mathbf{C} = \begin{bmatrix} \mathbf{c}_x & \mathbf{c}_{xy} & \mathbf{c}_{x\theta} \\ \mathbf{c}_{xy} & \mathbf{c}_y & \mathbf{c}_{y\theta} \\ \mathbf{c}_{x\theta} & \mathbf{c}_{y\theta} & \mathbf{c}_\theta \end{bmatrix} \tag{3.32}$$

$\Psi\upsilon\chi\acute{\alpha}\rho\eta\varsigma$ (2016) indicates that in practice, the damping matrix is hard to find an exact solution for, but for Idosyncratic analysis, it does not need to be calculated as it is present in the damping factor ζ.

The natural frequencies $\omega_{n.i}$ of the MDOF system from Eq. (3.25) can be found by solving the eigenvalue problem from the characteristic equation:

$$\det\left(\mathbf{K} - \omega_n^2 \mathbf{M}\right) = 0 \tag{3.33}$$

When subjecting the system to one of the natural frequencies, the corresponding mode shape $\boldsymbol{\beta_i}$ can be found by solving the equation:

$$\left(\mathbf{K} - \omega_i^2 \mathbf{M}\right) \boldsymbol{\beta}_i = \mathbf{0} \tag{3.34}$$

This equation is equivalent to a system of N equations with N unknowns, but because the determinant of Eq. (3.33) is zero, the system has an infinite number of solutions. By setting one of the unknowns $\beta_{j.i}$ equal to 1, the remaining unknowns of **fi$_\mathbf{i}$** can be found.

The mode shape can be normalized by dividing all modes $\beta_{j.i}$ by the maximum value of the upper floor $\beta_{N.i}$. This leads to the mode shape matrix $\boldsymbol{\phi}_i$ to the corresponding natural frequency $\omega_{n.i}$:

$$\boldsymbol{\phi}_i = \begin{Bmatrix} \boldsymbol{\phi}_{i.x} \\ \boldsymbol{\phi}_{i.y} \\ \boldsymbol{\phi}_{i.\theta} \end{Bmatrix} \tag{3.35}$$

Where $\boldsymbol{\phi}_{i.x}$, $\boldsymbol{\phi}_{i.y}$ and $\boldsymbol{\phi}_{i.\theta}$ are sub-matrices representing the mode shape in each direction for each story:

$$\boldsymbol{\phi}_{i.x} = \begin{Bmatrix} \phi_{1i.x} \\ \phi_{2i.x} \\ \dots \\ \phi_{Ni.x} \end{Bmatrix} \boldsymbol{\phi}_{i.y} = \begin{Bmatrix} \phi_{1i.y} \\ \phi_{2i.y} \\ \dots \\ \phi_{Ni.y} \end{Bmatrix} \boldsymbol{\phi}_{i.\theta} = \begin{Bmatrix} \phi_{1i.\theta} \\ \phi_{2i.\theta} \\ \dots \\ \phi_{Ni.\theta} \end{Bmatrix} \tag{3.36}$$

For buildings subjected to torsional effects, Ψυχάρης (2016) highlights that two points are important for the buildings behavior:

1. Center of rigidity (KD): If a force is given through the KD, the diaphragm will move purely in X- and/or Y-direction without twisting about a vertical axis.
2. Center of rotation (KS): The diaphragm will twist about the KS is a torsional moment is applied about a vertical axis.

In single-story buildings, the KD and KS will fall in the same point, while for multi-story buildings, the prediction of KD and KS can be more complex. Ψυχάρης (2016) provides a simplified conclusion that a building can be categorized as torsional if:

$$\omega_\theta \geq \omega_x \quad \text{and} \quad \omega_\theta \geq \omega_y \tag{3.37}$$

3.1.6 Damping

Damping is a phenomenon present in any dynamic system reducing the motion, and is the energy dissipation or redistribution of energy to surroundings through e.g. heat. de Silva (2005) separates damping into three main types. *Internal damping* refers to the energy dissipation in the material itself. This type of damping is typically modeled mathematically as viscoelastic or hysteretic damping. *Structural damping* refers to damping occurring in structural assemblies through friction, yielding of components, or other interaction of elements. The mathematical model of this is typically Coulomb damping. The third type is *fluid damping*, referring to damping between a structural element and a fluid, typically air or water. For a civil building, this type of damping is typically related to wind and is a complex phenomenon outside the scope of this thesis.

3.1.7 Ductility of structures

Ductility is related to the ability of a structural component to attain large deformations without loosing all strength. This is an important requirement in the design of a building as it allows redistribution of internal forces for connections with adequate ductility (Jorissen and Fragiacomo, 2011). The ductility ratio μ is the relationship between the maximum deformation u_{max} and the deformation at the yielding point u_y, as seen in Eq. (3.38).

$$\mu = \frac{u_{max}}{u_y} \tag{3.38}$$

3.2 Earthquake

This chapter contains an overview of earthquake as a phenomenon, how this phenomenon is considered when designing buildings, and the guidelines from Eurocode 8, with the additional National Annex. Accelerograms for historical earthquakes are presented.

3.2.1 Introduction to the concept of earthquake

Earthquake is a phenomenon that occurs when energy stored in the earth's crust is suddenly released. This is caused by the slip of two blocks of the earth in relation to each other. The surface where the slip occurs is defined by Alden (2016) as *fault plane*, and the starting point of the earthquake is refereed to as *hypocenter*. The location at the surface directly above the hypocenter is called the *epicenter*, as shown in Figure 3.8.

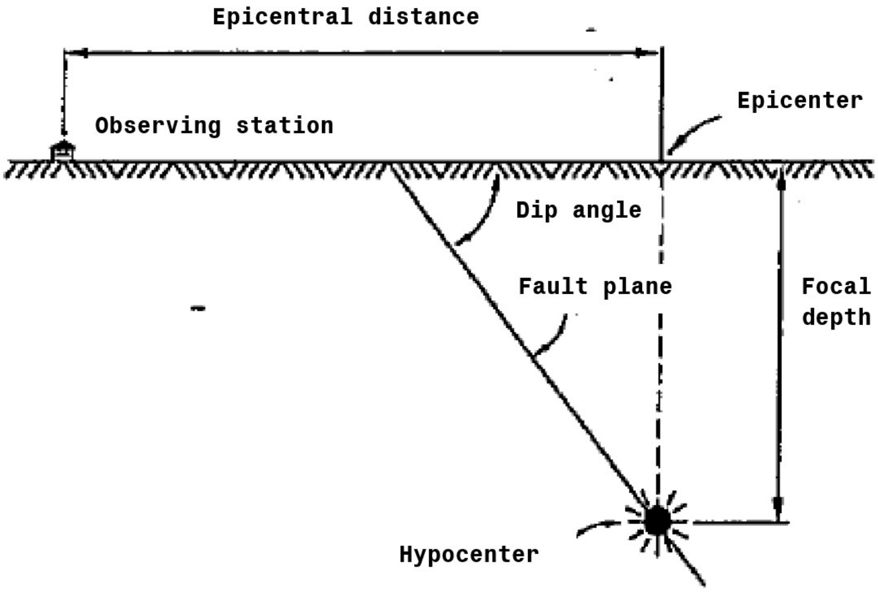

Figure 3.8: Explanation of earthquake terms, adopted after Lindeburg and McMullin (2014).

This release of energy is also called *fault* and happens when the tension in the plate boundary exceeds the yielding point of the weakest point in the boundary. Each side of the boundary moves to a new position through three different types of slip, shown in Figure 3.9.

(a) Normal fault - separation due to tension forces and results in extension of the crust

(b) Reverse fault - collision due to compressive forces and results in shortening of the crust

(c) Strike-slip - Lateral movement due to shear forces in the boundary

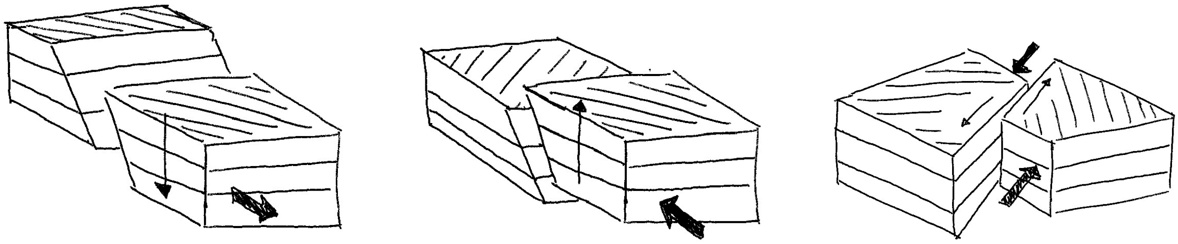
(a) Normal fault **(b)** Reverse fault **(c)** Strike-slip

Figure 3.9: Types of slip, adopted from Alden (2016).

3.2.2 Response and design spectra

The released energy from an earthquake travel through the soil and causes loads on the structure. These loads vary with time, and seismic loads can be characterized as dynamic loads. Some examples of registered ground motion during historical earthquakes can be seen in Figure 3.10.

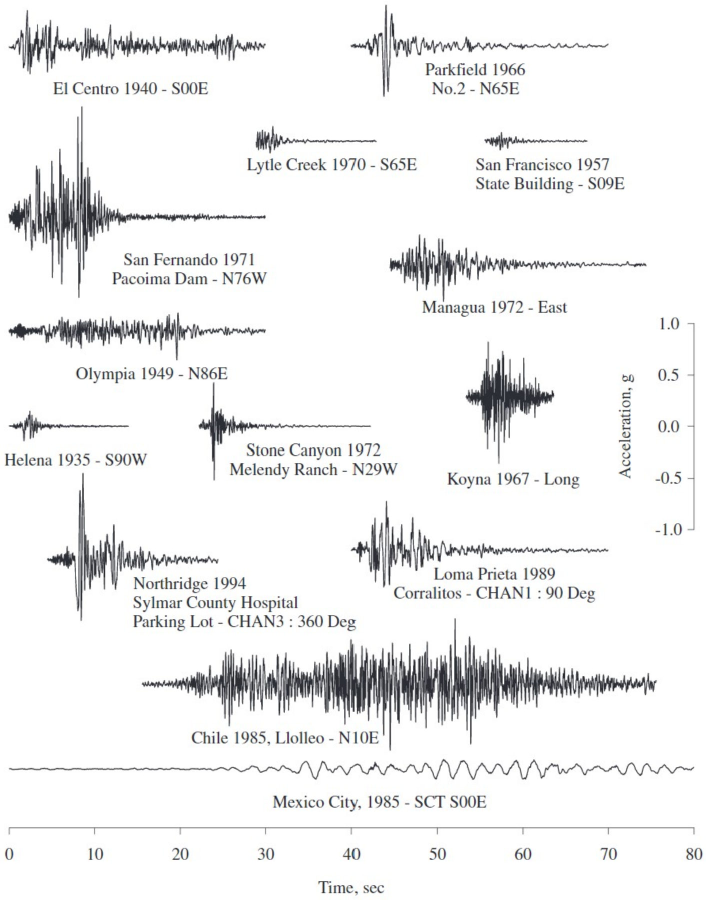

Figure 3.10: Recorded ground motion of several earthquakes (Chopra, 2012).

By applying the solution for the displacement of a structure subjected to an arbitrary loading seen in Eq. (3.23), a displacement response spectrum can be defined by using the maximum values. This spectrum is dependent on the natural frequency and the damping ratio of the structure:

$$u_0(T_n, \zeta) = max|u(t, T_n, \zeta)| \tag{3.39}$$

By differentiating Eq. (3.23) twice, the velocity and acceleration spectrum can be defined. Chopra (2012) highlights that these spectra for a given ground motion are three different ways of representing the structural response, where the deformation spectrum relates to peak deformation, pseudo-velocity spectrum relates to peak strain energy and pseudo-acceleration spectrum relates to static forces. By combining all spectra, the combined D-V-A (Displacement-Velocity-Acceleration) response spectrum can be created, as seen in Figure 3.11.

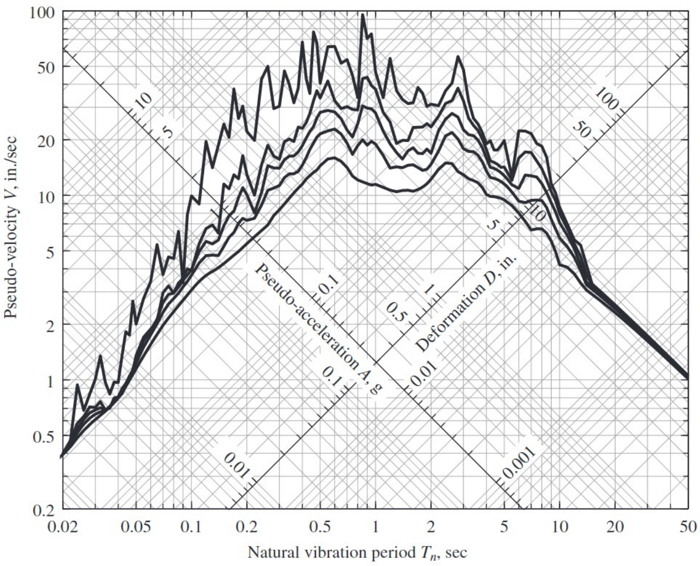

Figure 3.11: Combined D-V-A response spectrum for El-Centro earthquake for different values of damping ζ (Chopra, 2012).

For elastic systems, the response spectrum for a recorded ground motion is inappropriate, as the spectrum for two of the ground motions in Figure 3.10 will be jagged with differing peaks and valleys, and the shape of a future earthquake cannot be predicted. This leads to the introduction of *design spectrum*.

Design spectrum is based on a statistical analysis of the response spectra for a variety of ground motions for the given building location. The 84.1th and 50th percentile design spectra for El Centro earthquake are shown in Figure 3.12, comparing it to the response spectrum.

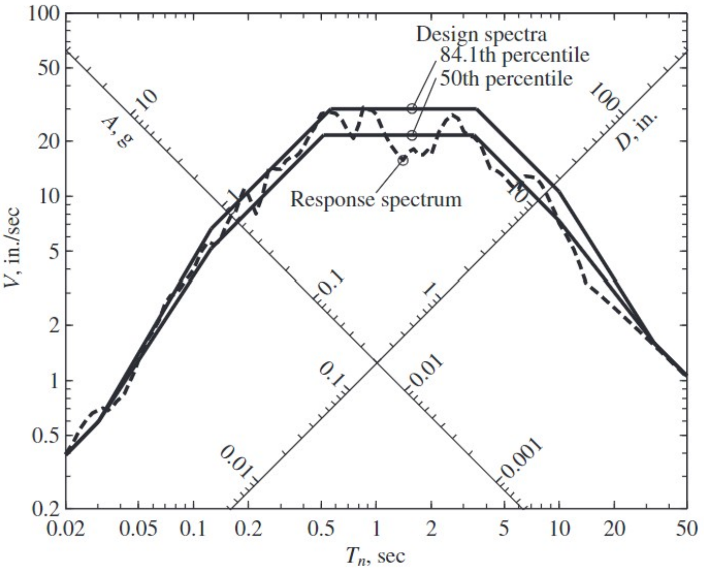

Figure 3.12: Comparison of design spectra with elastic response spectrum for El Centro earthquake (Chopra, 2012).

3.2.2.1 Normalized design spectrum

After the response spectra are combined into an idealized design spectrum, the normalized design spectrum can be defined as seen in Figure 3.13, where the change in gradient represents the change from acceleration to velocity and from velocity to displacement based calculation, respectively.

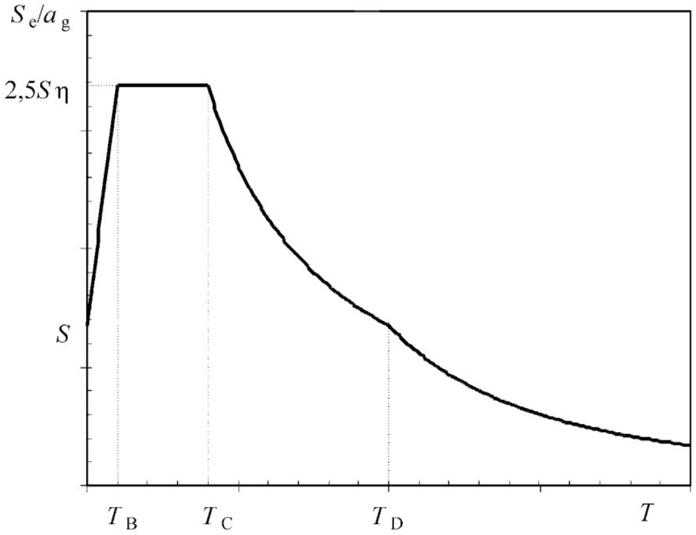

Figure 3.13: Shape of the elastic response spectrum from EC8-1.

3.3 Analytical model

This chapter describes the analytical theory behind methods used in structural engineering, and creates a background to support the methods used when analyzing multi-story hybrid buildings subjected to earthquake loading.

3.3.1 Finite element method

Finite element analysis or Finite element method (FEM) is a method of numerically solving problems from the field. This requires a spatial distribution of one or more dependent variables. This can be described by differential equations or integral expression, and the field of application ranges from temperature distribution in the piston of an engine to the global displacement of a structure (Bathe, 2008).

The solution from FEM is always an approximate solution, where a structure is split into elements connected by nodes. Each element represents a set of algebraic equations, and the particular arrangement of the elements is called a *mesh* connected by *nodes*. Splitting a structure into more elements will give a finer mesh, improving the approximated solution, which is found by applying the boundary conditions and forces (Cook et al., 2002).

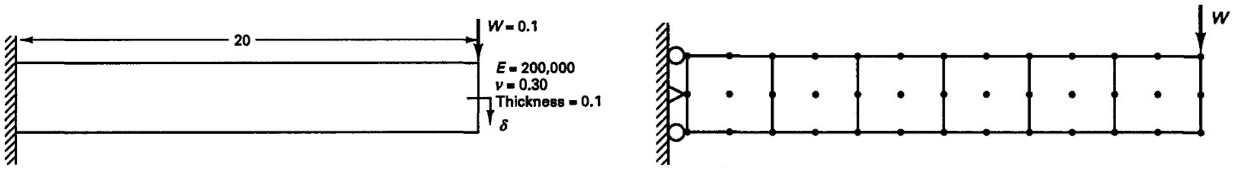

(a) Cantilevered beam with geometry, boundary conditions and material data

(b) Typical FEM discretization using 6x1 mesh of 9-node elements

Figure 3.14: Discretization of cantilevered beam to solve plane stress problem by Bathe (1996).

The displacement-based FEM uses the principle of virtual work, which require that the sum of internal virtual work is equal to the total external work for any compatible small virtual displacement imposed a body in equilibrium. This is expressed by Bathe (1996):

$$\underbrace{\int_V \bar{\boldsymbol{\epsilon}}^T \boldsymbol{\tau} dV}_{\textit{Internal virtual work}} = \underbrace{\int_V \overline{\boldsymbol{U}}^T \boldsymbol{f}^B dV + \int_V \overline{\boldsymbol{U}}^{S_f^T} \boldsymbol{f}^{S_f} dS + \sum_i \overline{\boldsymbol{U}}^{iT} \boldsymbol{R}_C^i}_{\textit{External virtual work}} \tag{3.40}$$

where

$\overline{\boldsymbol{U}}$ are virtual displacements

$\bar{\boldsymbol{\epsilon}}$ are the corresponding virtual strains

$\boldsymbol{\tau}$, $\boldsymbol{f}^B$, $\boldsymbol{f}^{S_f}$ and $\boldsymbol{R}_C^i$ are stresses in equilibrium with applied loads

In Eq. (3.40), the stresses are assumed to be unique stresses that balance the applied loads, and $\overline{\boldsymbol{U}}$ must represent a continuous virtual displacement field for evaluation of $\bar{\boldsymbol{\epsilon}}$. The governing finite element equations can be derived by replacing the virtual displacements with correct reactions.

In linear analysis, the material laws are assumed constant with infinitesimally small displacements and constant volume and surfaces. For an element with j nodal points, Bathe (2008) presents:

$$x = \sum_{i=1}^{k} h_i x_i \qquad y = \sum_{i=1}^{k} h_i y_i \qquad z = \sum_{i=1}^{k} h_i z_i \tag{3.41}$$

and

$$u = \sum_{i=1}^{k} h_i u_i \qquad v = \sum_{i=1}^{k} h_i v_i \qquad w = \sum_{i=1}^{k} h_i w_i \tag{3.42}$$

where

h_i are the given interpolation function of the elements natural coordinates (r, s, t)

x_i, y_i and z_i are the global coordinates of node i

u_i, v_i and w_i are the unknown displacements of node i

By substituting Eq. (3.41) and Eq. (3.42) into Eq. (3.40), Bathe (2008) obtains the following relationship:

$$\boldsymbol{KU} = \boldsymbol{R} \tag{3.43}$$

This is equal to the relationship already described in Eq. (3.16) but with matrix formulation. $\boldsymbol{K}$ is the stiffness matrix, $\boldsymbol{U}$ is the displacement vector describing all unknown node displacement, and $\boldsymbol{R}$ is a vector containing externally applied forces.

For all FEM analyses, Bathe (1996) highlights the importance of choosing an appropriate mathematical model since FEM only solves the exact model. This includes the choice of boundary conditions, element types, and the results judgment by the user. This also includes choosing a sufficient model with reliable accuracy without creating an over-conservative model.

3.3.2 Finite element software

SAP2000 is a general-purpose structural analysis program based on FEM (CSI, 2021). The program can be used for a various structural problems, ranging from simple 2D systems to complex non-linear dynamic analysis. The program has integrated code-based loading assignments and design checks with design optimization. Linear and curved members, cables and post-tensioned tendons, frames, shells and solid elements are some of the available modeling options for structural assembly (Habibullah, 2021).

For earthquake analysis, both static and dynamic methods are available. The static *non-linear pushover analysis* can be used to consider modal load patterns, creating inelastic response of shear walls, floor slabs or plastic hinging behavior of slender elements. The dynamic analysis methods among others are: *response spectrum* for the maximum seismic response, *steady-state* for fatigue behavior with or without damping, or *time history* to implement historical earthquakes (Habibullah, 2021).

Many meshing options are available, including automatic meshing, size-based meshing, and manual meshing. Automatic edge constraints can be applied to elements, connecting edge joints of the element to adjacent corner joints. Joints are considered to be edge joints if being within the auto-merge tolerance and can be user-defined (CSI, 2004).

Some limitation of SAP2000 is that timber as a material is not available as a default material, meaning that analysis with GLT and CLT requires user-defined material properties and sections. This also includes timber connections, leading to a necessary conversion from real, physical connections to a theoretical implementation. HCS sections are not available either, but special sections can be custom made by using *section designer*.

3.3.3 Hollow core slab

When using concrete elements as floors in buildings, Moustafa (1981) proposes that in addition to carrying superimposed gravity loadings, the flooring system should be able to transfer horizontal shear into the lateral load carrying system caused by wind or earthquake. The assumption of infinite rigidity in the floor's plane is an important factor, and the connecting on-site should be done carefully.

Jendzelovsky and Vrablova (2015) calculated the natural frequencies of concrete slabs with FEM using three models: (1) a solid 2D plate, (2) a solid 2D plate with a reduction of stiffness and density, and (3) a 3D model with properties similar to a real HCS. The stiffness correction factor was set to 0.92, and the reduction in dead load set to 2.86 kN/m^2 for model (2). The reduced, simplified model (2) gave similar results to experimental data for static problems, but the for calculation of the plate's natural frequencies, the approximation is concluded to be inappropriate.

Chang et al. (2006) investigated the performance of HCS under fire with simplified modeling of the system. The HCS units are modeled as beam grillages, with transverse and longitudinal elements interconnecting, where only the top and bottom fiber are included in the transverse direction. The reinforced concrete topping is modeled as a shell element, sharing the degrees of freedom and joining the grillage system.

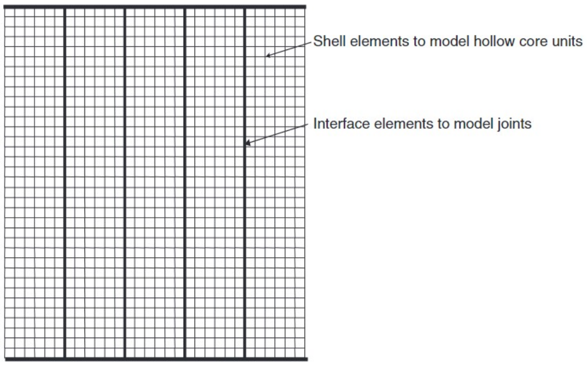

Figure 3.15: Simplified model of slab consisting of HCS using shell elements (Lundgren et al., 2004).

Lundgren et al. (2004) investigated a HCS-system with an element height of 400 mm subjected to shear and torsion by using two different models. The first model consists of a 3D beam with a cross-section divided into zones creating a section similar to a real HCS section (similar to a section seen in Figure 2.2). The second model was modeled as a quadrilateral, isoparametric, curved shell with interconnecting joints. The shell elements were assigned a thickness of 354 mm, giving an effective thickness ratio of 0.885 and corresponding effective bending stiffness to a 400 mm thick HCS. The bending stiffness is assumed to be equal in the transverse direction for each element. The interconnection of the HCS was modeled as hinged slave nodes, meaning high stiffness in compression and low stiffness in tension. It is highlighted by the authors that a traditional hinged connection works as a reference, while the slave node represents the reality better by including the effect of cracking in the longitudinal voids. The schematic drawing can be seen in Figure 3.15.

Bernardi et al. (2016) investigated the SLS load distribution and shear forces transmitted along the connecting joints for HCS. Each HCS is treated as a Saint-Venant element, meaning only the center line of the element is considered, and the transversal deformation is assumed negligible. The stiffness correction for HCS is determined by the flexural stiffness $E \cdot J$ and the torsional stiffness $G \cdot I_0$. The interconnection of elements representing the reinforced concrete joint is treated as rotational hinges. This leads to no bending moment transfer, and applying this analytical method when a concrete topping is used will lead to conservative results. The authors suggest that a concrete topping adds partial moment resistance in the transverse direction. Thicker topping is commonly used in earthquake-prone areas. A brief overview of the different analytical approaches is shown in Table 3.1.

Table 3.1: Brief overview of some approaches for analytical modeling of HCS.

	Analytical model	**Cross-section approach**	**Correction factor**	**Interconnection**	**Transverse bending translation**
Bernardi et al. (2016)	Saint-Venant beam	Stiffness/torsional correction	Flexural/torsional properties	Rotational hinge	Hinged
Chang et al. (2006)	Beam grillage + shell topping	Longitudinal and transverse fibres	-	Grillage system + connecting shell	Yes
Jendzelovsky and Vrablova (2015)	Solid 2D plate	Solid section	-	Continuous 2-way shell	
Jendzelovsky and Vrablova (2015)	Reduced 2D plate	Reduced stiffness and mass	0.92 · stiffness -2.86 kN/m^2 selfweight	Continuous 2-way shell	
Jendzelovsky and Vrablova (2015)	Solid 3D	Hollow core modules	-	Continuous 2-way shell	
Lundgren et al. (2004)	3D Beam system	Zoned HCS	-	Slave nodes	Hinged
Lundgren et al. (2004)	Quadrilateral shell	Reduced cross section	0.885	Continuous 2-way shell	Yes

3.3.4 Glued laminated timber

Glued Laminated Timber (GLT) or *glulam* was introduced in the late 19th century and consists of wood lamellas bonded with adhesives so that the fiber direction of all laminations runs parallel to the longitudinal direction. GLT can be produced in a various dimensions, shapes, and strength classes (Issa and Kmeid, 2005). Manufacturers can place high-grade lumber near the top and bottom fiber, while lower grade can be used in mid layers. This type of GLT is referred to as *GLc* (combined), shown in Figure 3.16a. GLT with the same grade of lumber through the whole section is referred to as *GLh* (homogeneous), as shown in Figure 3.16b.

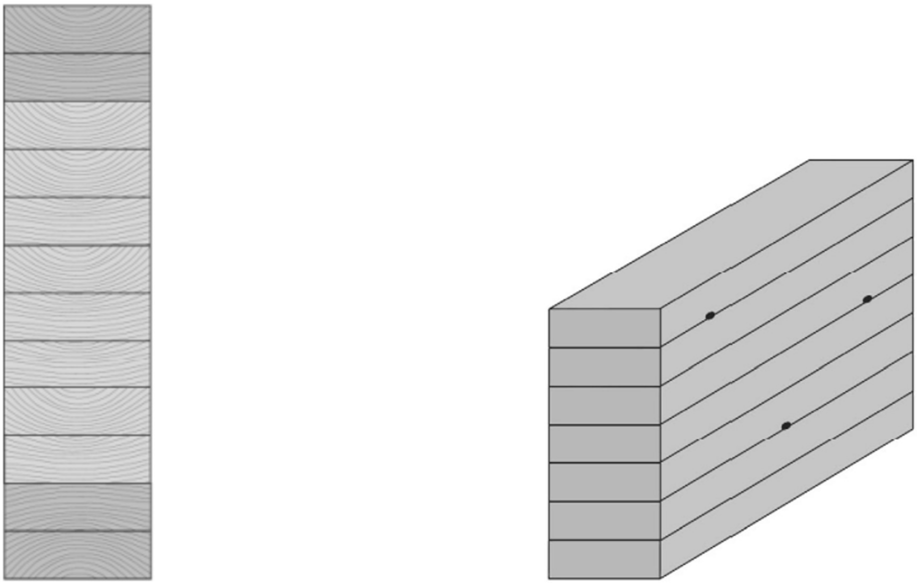

(a) Combined GLT (GLc).

(b) Homogeneous GLT (GLh).

Figure 3.16: Types of GLT from Crocetti et al. (2015).

The homogeneous build-up leads to higher strength capacity but is more expensive to produce (Aicher and Tapia, 2018). Differences in mechanical properties are shown in Table 3.2, showing that the bending strength, shear strength, and tension perpendicular to fiber strength is the same for GLc and GLh. In contrast, the tensile and compressive strength is higher for GLh.

Table 3.2: Mechanical properties of combined and homogeneous GLT (Hasslacher group, 2021). All numbers in N/mm^2.

	bending	**compression**	**tension parallel**	**tension perp.**	**shear**
GL32c	32	32	25.6	0.5	3.5
GL32h	32	24.5	19.5	0.5	3.5

Dugdale (2015) suggests that a GLT beam can be modeled by idealizing it to be an orthotropic material. Orthotropic, in this case, means that the material is idealized with three main directions for the properties, each mutually perpendicular to the other. This represents the longitudinal, tangential, and radial directions for timber, as seen in Figure 3.17. Dugdale (2015) collected material properties for *26-1.9F Southern pine* and the values are converted from *ksi* to N/mm^2 for comparison.

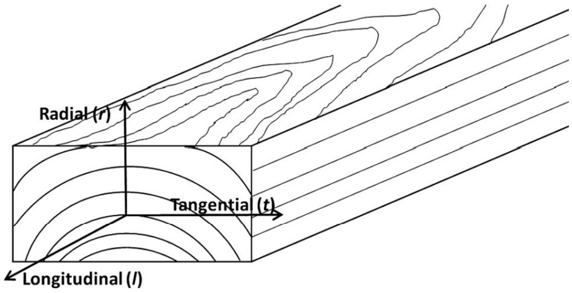

Figure 3.17: Graphical explanation of the main directions for timber (Zhou et al., 2014).

Vratuša et al. (2011) investigated structural particulars of tapered GLT beams of grade GL28h with varying heights. The analytical model consisted of orthotropic 4-node final elements with two main directions, being (1) parallel to grain and (2) perpendicular to grain, where the shear modulus is assumed equal for all directions. Zhao et al. (2021) did a numerical simulation of the global static and dynamic behavior of a 105-meters tall building built in various grades of GLT, where the timber grade for the reference building is GL24c. The GLT beams are assumed here to have orthotropic properties in 2 directions. An overview of the values used in the mentioned researches are shown in Table 3.3.

Table 3.3: Material properties used for modeling GLT. All numbers are converted to N/mm^2.

	Analytical material	GLT type	Longitudinal Young's modulus (E1)	Tangential Young's modulus (E2)	Radial Young's modulus (E3)	Shear modulus parallel to grain (G1)	Shear modulus perp. to grain (G2)
Dugdale (2015)	Orthotropic, 3 directions	26-1.9F Southern pine	13100	1480	1034	1061	170
Vratuša et al. (2011)	Orthotropic, 2 directions	GL28h	12600	420	-	780	780
Zhao et al. (2021)	Orthotropic, 2 directions	GL24c	11000	300	-	650	65

3.3.5 Cross laminated timber

Cross Laminated Timber (CLT) is an engineered wood product (EWP) based on minimum three layers with alternating timber glued together to form a solid panel with high strength to weight ratio. The technology has been applied in Europe for several decades and has been crucial in building high-rise timber buildings (Mahdavifar et al., 2016).

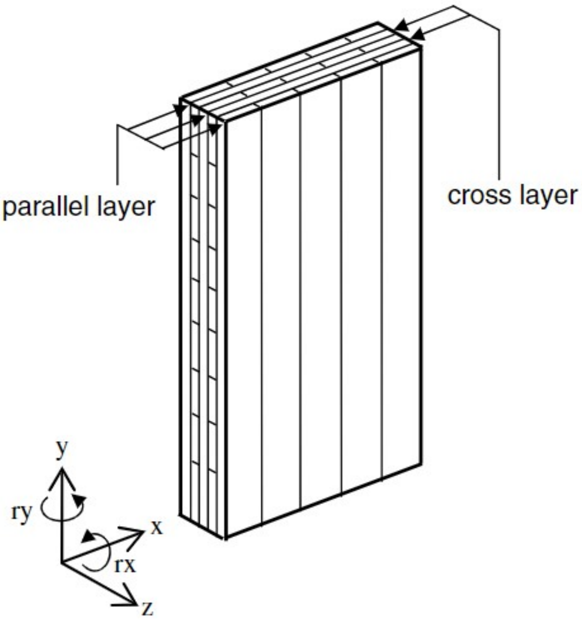

Figure 3.18: Graphical view of CLT panel with axis definition from Yasumura et al. (2016).

The analytical model of CLT is pivotal in taking into account the effect of the anistropic properties of timber. This is because CLT elements can resist both horizontal and vertical loads and both out-of-plane and in-plane loadings. The alternating layers give mechanical properties based on the number of horizontal and vertical layers, the thickness of each layer, and the timber quality. A graphical view of a typical CLT panel is seen in Figure 3.18.

Currently, there are no official standards for CLT design, but EC5 Annex B proposes the *Gamma method* to account for out-of-plane shear stress. This method is based on the effective stiffness and connection effective ratio γ. Mahdavifar et al. (2016) criticizes this method for not including rolling shear effects and, therefore, not being suitable for span-to-depth ratios exceeding 27.

Figure 3.19: Thickness definition by Follesa et al. (2013).

Follesa et al. (2013) present a solution based on the orthotropic properties of wood, the number of layers, and the direction. The material properties can be defined by modeling CLT elements as orthotropic shell elements following the principal axes given in Figure 3.18, the material properties can be defined. By the thickness definitions a_1, a_3, and a_5, as seen in Figure 3.19, the properties can be found:

$$E_y = \left[1 - \left(1 - \frac{E_{90,T}}{E_{0,L}}\right) \cdot \frac{a_3 - a_1}{a_5}\right] \cdot E_{0,L} \tag{3.44}$$

$$E_x = \left[\frac{E_{90,T}}{E_{0,L}} + \left(1 - \frac{E_{90,T}}{E_{0,L}}\right) \cdot \frac{a_3 - a_1}{a_5}\right] \cdot E_{0,L} \tag{3.45}$$

$$E_z = t_{tot} \left(\sum_{i=1,3,..}^{n} t_i / E_{90,L,i} + \sum_{j=2,4,..}^{n-1} t_i / E_{90,T,j} \right)^{-1} \tag{3.46}$$

$$G = t_{tot} \left(\sum_{i=1,3,..}^{n} t_j / G_{L,i} + \sum_{j=2,4,..}^{n-1} t_i / G_{T,j} \right)^{-1} \tag{3.47}$$

3.3.6 Timber connections

In this section, several types of timber connections from previous research are presented. The geometry, properties, and method of calculating the rotational stiffness is presented for each connection, in addition to research results and failure modes.

A dowel-type connection connects the beam with the column by slotted inn plates drilled with holes, as seen in Figure 3.20. Dowels are inserted and glued in place, and both the slotted-in plates and the dowels can be of different materials, e.g., steel or wood (Frenette, 1997).

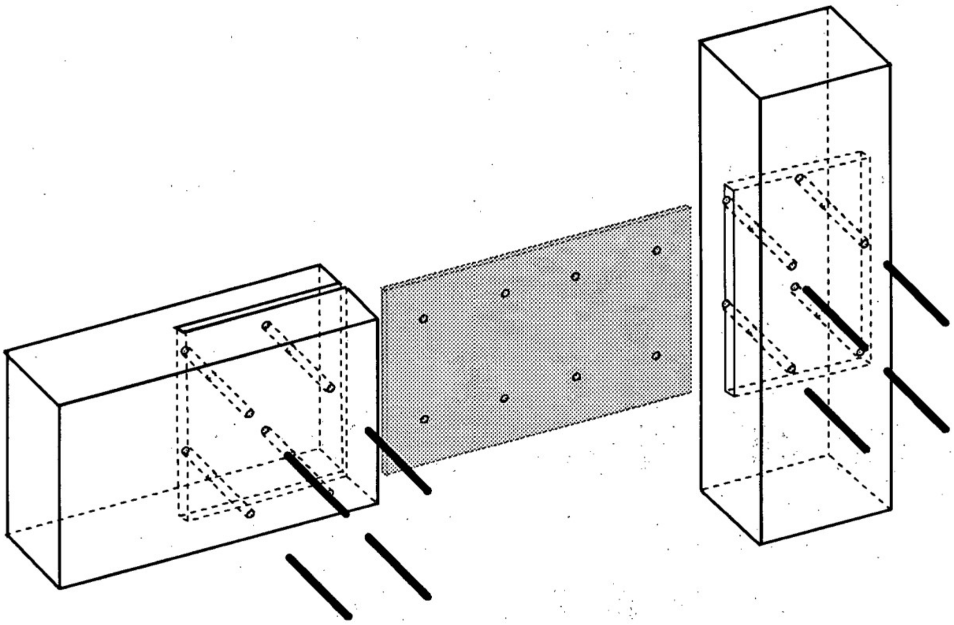

Figure 3.20: Example of dowel type connection, with eight dowels and slotted in plate (Frenette, 1997).

The rotational stiffness K_r per shear plane in SLS is given by EC5:

$$K_{r,ser} = \sum_{i=1}^{n} K_{ser} \cdot r_i^2 \tag{3.48}$$

Where r_i is the distance from the Center of Rotation (COR) to the fastener, and K_{ser} is the slip modulus of one fastener given by EC5-1 Table 7.1.

$$K_{ser} = \frac{\rho_m^{1.5} \cdot d}{23} \tag{3.49}$$

EC5 (2.1) gives the conversion from SLS to ULS by $K_u = 2/3 \cdot K_{ser}$.

Different materials used as plates or dowels offer different dynamic properties. Blaß and Schädle (2011) suggest that a dowel connection with steel dowels offers ductility by nature and can be regarded as moment resisting when an appropriate placement and amount of dowels are used. Frenette (1997) suggests a semi-rigid resistance for dowel connections.

Zhou et al. (2021) compare a traditional bolted connection with slotted-in steel plates (FS) with an innovative solution comprising top-and-seat steel angles (FDF). The two types of connection are shown in Figure 3.21. Both cases connect a GLT beam of dimension 130x300 mm to a GLT column 220x220 mm. The rotational stiffnesses were calculated by assuming 40% of the maximum bending moment to the associated rotation, and the traditional connection with bolts gave a rotational stiffness of $k_\theta = 241$ kNm/rad. In contrast, the connection with top-and-seat steel angles gave a rotational stiffness of $k_\theta = 969$ kNm/rad, approximately three times higher. The authors concluded that the FDF solution could be classified as semi-rigid according to Eurocode 3, while the FS solution is a typical hinged connection. A reduced member version of the FDF solution with beams of 130x250 mm and columns 180x180 produced 73% of the rotational stiffness of FDF, showing that the rotational stiffness is dependent on the member size.

The failure mode of FS was due to torsion in the bolt group, splitting the beam due to tension perpendicular to grain. Bearing failure in the column was also observed in the compressive zone of the beam. The FDF showed failure due to splitting in the beam's end and embedding of bolt holes resulting from significant bending in the bolts in the beam. The bolts in the columns showed no sign of bending (Zhou et al., 2021).

Tsalkatidis et al. (2018) investigated a similar connection with steel angles for a hybrid structures. A parametric study of a glulam beam with dimensions of 405x140 mm connected to a square hollow steel column 150x10 mm with steel angles of 150x200x15 mm, MR12 HR bolts to the glulam beam, and M16 HR bolts to the steel column. Varying the dimensions of angles and bolts lead to an optimal build-up of the connection, with 20 mm thick steel angles and 20 mm thick bolts increasing the rotational stiffness of the connection by 137% while decreasing the von Mises stress by 32.7%. Karagiannis et al. (2017) formulated an expression for the rotational stiffness for this type of connection based on the initial rotational stiffness of the top- (K_{top}) and seat- (K_{bottom}) angle components as seen in Eq. (3.50):

$$K_{\theta,init} = \frac{h_{gl}^2}{1/K_{top} + 1/K_{bottom}} \tag{3.50}$$

Where h_{gl} is the height of the glulam beam and:

$$K_{top} = \frac{1}{1/K_{CF} + 1/K_{HB} + 1/K_t} \tag{3.51}$$

$$K_{bottom} = \frac{1}{1/K_{CF} + 1/K_t} \tag{3.52}$$

where

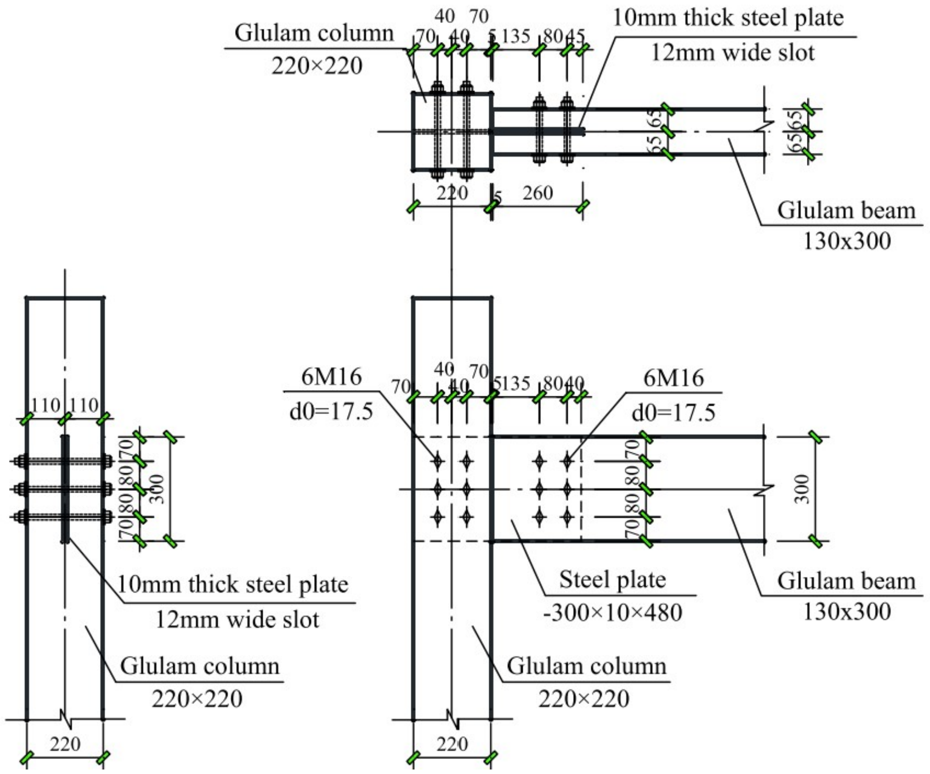

(a) Traditional bolted connection (FS) (Zhou et al., 2021).

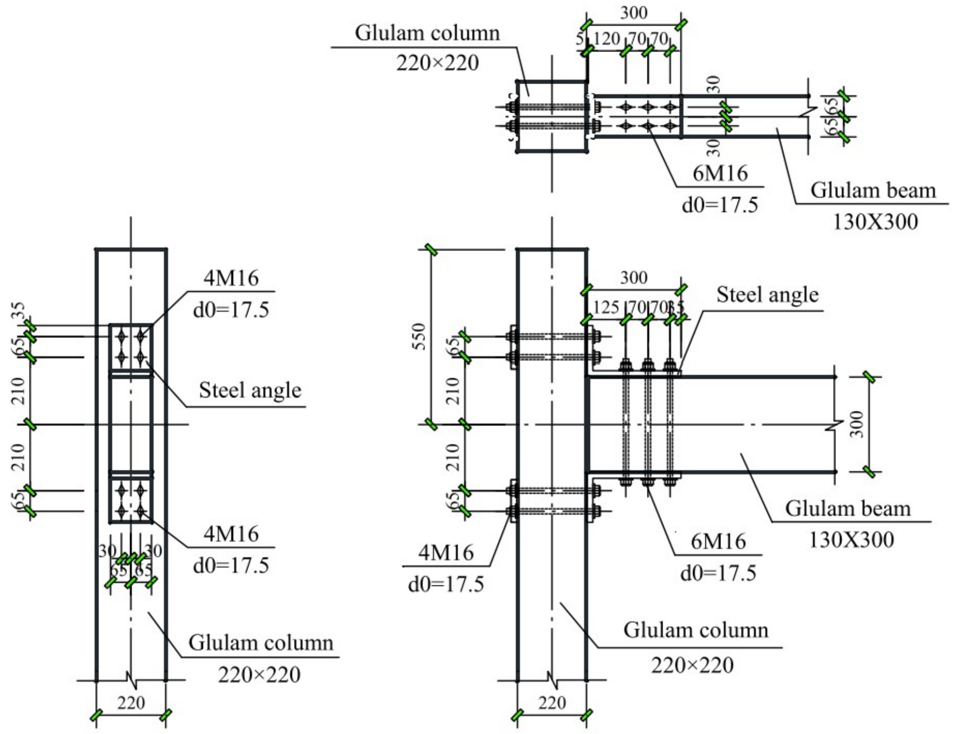

(b) Top-and-seat steel angles connection (FDF) (Zhou et al., 2021).

Figure 3.21: Two types of bolted connections compared by Zhou et al. (2021).

K_{CF} is the bearing stiffness of the column face

K_{HB} is the Hollo-bolt axial stiffness

K_t is the tensile stiffness of the angle horizontal leg

The expression for K_{HB} and K_t is described by Málaga-Chuquitaype and Elghazouli (2010):

$$K_{HB} = \frac{A_b E}{L_b} N \tag{3.53}$$

where

A_b is the cross-sectional area of the bolt

N is the number of bolts considered to contribute to the stiffness

L_b is the effective length of the bolt, typically the shank length

and

$$K_t = \frac{E \cdot p \cdot t_f}{a'} \tag{3.54}$$

where

p is the steel angle width

t_f is the steel angle thickness

a' is the distance from the vertical bolt to one of the critical yielding points in the angles, located $t_f + 0.8r$ from the column face

As K_{CF} from Tsalkatidis et al. (2018) and Karagiannis et al. (2017) is based on the bearing stiffness of a steel column, the formulation for GLT from Yang et al. (2016) gives an expression for the part of the column in compression:

$$K_{CC} = \frac{E_{90} b_c l_{eff,cc}}{h_c} \tag{3.55}$$

where

E_{90} is the modulus of elasticity perpendicular to grain

b_c is the width of the GLT column

$l_{cc,eff}$ is the effective length of the area under compression of the GLT column

h_c is the depth of the GLT column

Buchanan and Fairweather (1993) describes several connections for timber frames, consisting mainly of epoxied steel bars. The authors highlight that constraints in designing multi-story glulam buildings have been the lack of high-strength beam-to-column-connections. Glued connections are not suitable for seismic design unless designed for elastic response, as they offer very low, or no ductility at all, and tend to have brittle failure. Using epoxied steel bars, a connection was designed to encounter yielding of the steel before failure of the wood.

The connection can be seen in Figure 3.22 and was adopted from Fairweather (1992), who calculated the stiffness of this type of connection with varying parameters. This included a varying the number and diameter of rods, and the arrangement. The connection showed a ductile failure mode, with a ductility factor $\mu = 6$. Failure was caused by buckling in the steel bar, leading to splitting of the wood (Buchanan and Fairweather, 1993).

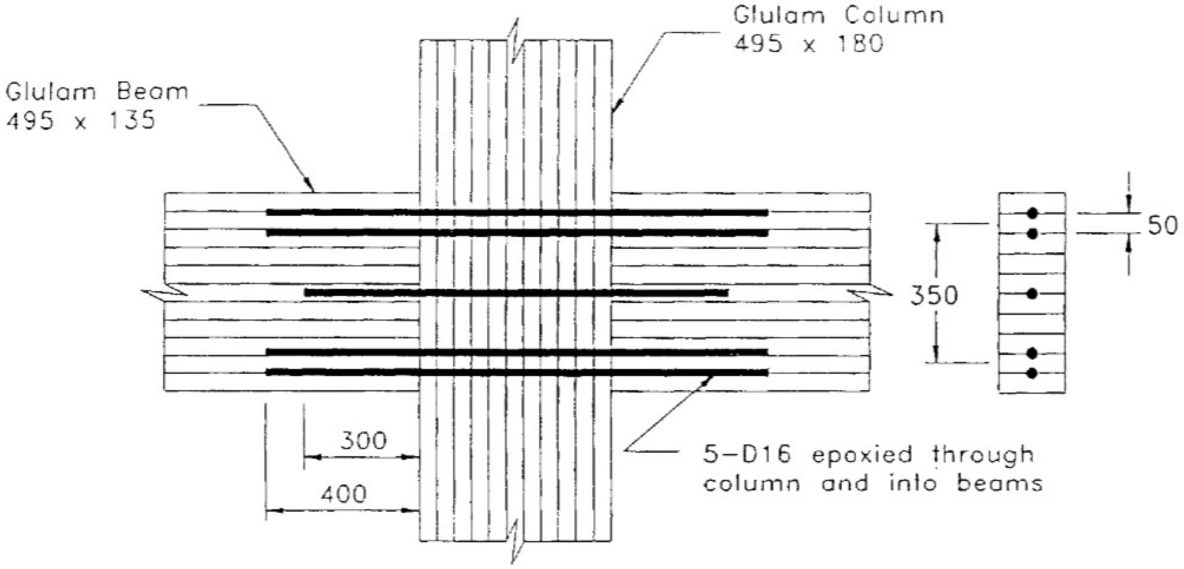

Figure 3.22: Example of intermediate connection using epoxy filled GLT with steel bars adopted by Buchanan and Fairweather (1993) from Fairweather (1992).

Yang et al. (2016) present a method of calculating the rotational stiffness $S_{j.init}$ for an adapted version of this connection with a steel box section by applying the component method. The simplified version can be described with springs, as seen in Figure 3.23. z_{eq} is the equivalent lever arm, k_t represents the initial tensile stiffness and k_c represents the initial compressive stiffness. This leads to Eq. (3.56).

$$S_{j,init} = \frac{z_{eq}^2}{1/K_t + 1/K_c} \tag{3.56}$$

where the compressive stiffness K_c is defined as:

$$K_c = \frac{1}{1/K_{cs} + 1/K_{cc} + 1/K_{srtc} + 1/K_{bc}} \tag{3.57}$$

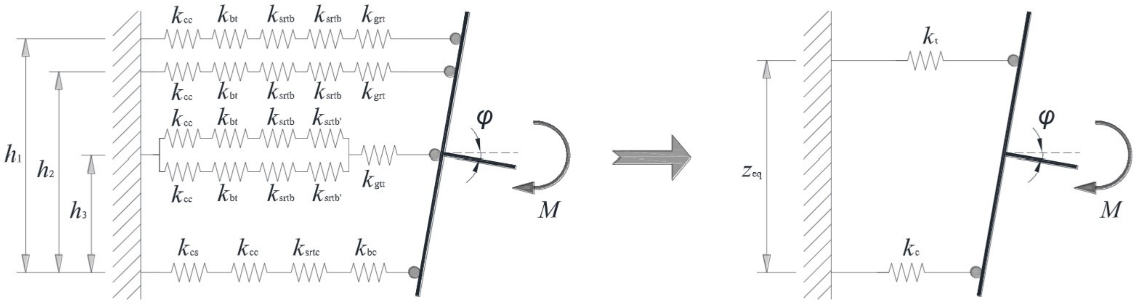

Figure 3.23: Simplification of mechanical of beam-to-column connection by Yang et al. (2016) using component method.

where

K_{cs} is the shear stiffness of the glulam column

K_{cc} is the transverse stiffness of the glulam column

K_{srtc} is the initial stiffness of the steel box

K_{bc} is the stiffness of the glulam beam in compression

K_{bc} is defined by Tomasi et al. (2008) as:

$$K_{bc} = \frac{E_{w.0}\sqrt{b_{eff}l_{eff}}}{\beta} \tag{3.58}$$

where

$E_{w.0}$ is the elastic modulus of timber parallel to grain

b_{eff} and l_{eff} defines the effective area of compression

β is a dimensionless coefficient approximated to the value of 4

The stiffness of the GLT column in shear can by Yang et al. (2016) be determined by classic mechanics theory for a short column:

$$K_{cs} = \frac{G_w \cdot A_c}{z_{eq}} \tag{3.59}$$

where

G_w is the shear modulus of the column

A_c is the cross-sectional area of the column

The tensile stiffness K_t is defined according to Eq. (3.60)

$$K_t = \frac{\sum K_{eff,r} h_r}{z_{eq}} \tag{3.60}$$

where

$K_{eff,r}$ is the effective stiffness of the bolt row r

h_r is the distance from the bolt row r to center of compression

The stiffness of the glued-in rod is defined by EC3-1 as an anchor bolt without prying forces.

$$\frac{2.0 \cdot E_{rod} \cdot A_{rod}}{L_{rod}} \tag{3.61}$$

The elongation length L_{rod} can be found following $L_{rod} = \alpha \Phi_{rod}$, where α can be found by Eq. (3.62) and Φ_{rod} is the diameter of the glued-in rod (Tomasi et al., 2008):

$$\alpha = \left[\left(1 + \frac{E_{rod}}{45.8 E_{w.0}}\right) \cdot \Phi_{rod} \cdot \sqrt{\left(1 + \frac{E_{rod}}{45.8 E_{w.0}}\right) \cdot \frac{G_{epoxy} \pi \Phi_{rod}}{E_{rod} A_{rod.s} t_{epoxy}}} \right]^{-1} \tag{3.62}$$

where

E_{rod} is the elastic modulus of the rod

G_{epoxy} is the shear modulus of the epoxy

t_{epoxy} is the thickness of the epoxy layer

The relevant properties used for the Epoxy resin are the Tensile modulus of elasticity and the shear modulus, listed in Table 3.4.

Table 3.4: Mechanical properties of epoxy resin from Yang et al. (2016).

Property	Unit	Value
Tensile modulus of elasticity	MPa	>2800
Shear modulus	MPa	1500

Vilguts et al. (2021) investigated moment-resisting timber frames by modeling the beam-to-column as semi-rigid. A rotational spring with stiffness k_θ simulated this, while the translational movement was considered rigid due to negligible influence shown in the preliminary design. The connection to the foundation was simulated as both hinged and semi-rigid, considering unfavorable effects from the foundation. The authors suggest a rotational stiffness of minimum 12 500 kNm/rad for buildings up to 8 stories to fulfill acceleration and inter-story drift SLS requirements and that slender frames with a height-to-length ratio > 1.5 is not recommended. The fundamental frequency calculation from EC1-1-4 and EC8-1 using only the building's height does not give accurate results for moment-resisting timber frames.

Stamatopoulos et al. (2022) compare two semi-rigid connections for timber frames with inclined threaded rods. The first connection can be seen in Figure 3.24, where the inclined rods from the beam and the column are fastened with bolts inside steel rings. The analytical rotational stiffness for this connection was found by the component-method approach, where the connection was separated into spring components on the column side, beam side, and steel coupling parts. There is assumed to be no contact between the connected elements for the analytical model. The rotational stiffness provided by both the column-side and the beam-side of the connection is based on the geometric properties and axial stiffness of the threaded rods.

The geometric properties are accounted for by the transformation matrix $\mathbf{Q_c}$. For the column side, one transformation matrix is necessary for the rods in tension (c_1 and c_2), and on for rods in compression (c_3 and c_4):

$$\mathbf{Q}_{\mathbf{c}.12} = \begin{bmatrix} s_{c1} & c_{c1} \\ s_{c2} & -c_{c2} \end{bmatrix} \qquad \mathbf{Q}_{\mathbf{c}.34} = \begin{bmatrix} s_{c3} & c_{c3} \\ s_{c4} & -c_{c4} \end{bmatrix} \tag{3.63}$$

where $s_{ci} = \sin(\alpha_{ci})$, $c_{ci} = \cos(\alpha_{ci})$

For the beam side a transformation matrix is required for (1) top and (2) bottom rod:

$$\mathbf{Q}_{\mathbf{b}.1} = \begin{bmatrix} c_{b1} & s_{b1} \\ -s_{b1} & c_{b1} \end{bmatrix} \qquad \mathbf{Q}_{\mathbf{b}.2} = \begin{bmatrix} c_{b2} & -s_{b2} \\ s_{b2} & c_{b2} \end{bmatrix} \tag{3.64}$$

The stiffness of rods at the column side is assumed by Stamatopoulos et al. (2022) to only be provided by the axial stiffness of the rod $K_{ax.l0}$ and the withdrawal stiffness of a threaded rod $K_{ser.ax}$.

$$K_{ax.l0} = \frac{A_{net} \cdot E_s}{l_0} \tag{3.65}$$

where E_s is the modulus of elasticity of steel, A_{net} is the net area of the rod, based on 90% of the diameter of a metric rod and l_0 is the non-embedded length of the rod:

$$K_{ser.ax} \approx \frac{50000 \cdot (d/20)^2 \cdot (\rho_m/470)^2 \cdot \min\left[(l/300)^{0.75}; 1\right]}{0.4 \cdot \cos^{2.3}\alpha + \sin^{2.3}\alpha} \tag{3.66}$$

where d is the outer diameter of the rod, ρ_m is the mean density of the timber, l is penetration length of the rod and α is the angle between the rod and the grain direction in the element. This leads to the axial stiffness of the rods on the column side:

$$K_{ax.c} = \frac{K_{ser.ax} \cdot K_{ax.l0}}{K_{ser.ax} + K_{ax.l0}} \tag{3.67}$$

By combining $\mathbf{Q_c}$ with the axial stiffness, the compliance terms can be found for conversion to global coordinate stiffness:

$$S_{xx.c}^{ci-c(i+1)} = \frac{\frac{c_{ci}^2}{K_{ax.c(i+1)}} + \frac{c_{c(i+1)}^2}{K_{ax.ci}}}{\left(c_{ci} \cdot s_{c(i+1)} + c_{c(i+1)} \cdot s_{ci}\right)^2} \tag{3.68}$$

$$S_{xy.c}^{ci-c(i+1)} = \frac{\frac{c_{ci} \cdot s_{ci}}{K_{ax.c(i+1)}} + \frac{c_{c(i+1)} \cdot s_{c(i+1)}}{K_{ax.ci}}}{\left(c_{ci} \cdot s_{c(i+1)} + c_{c(i+1)} \cdot s_{ci}\right)^2} \tag{3.69}$$

The rotational stiffness provided by the threaded rods on the column side consists per plane of rods is then expressed as:

$$K_{\theta.C} = \frac{z^2}{\left(S_{xx.c}^{(c1-c2)} + S_{xx.c}^{(c3-c4)}\right) + \left(S_{xy.c}^{(c3-c4)} - S_{xy.c}^{(c1-c2)}\right) \cdot \frac{z}{2 \cdot L_v}} \tag{3.70}$$

including the compliance terms $S_{xx.c}$ and $S_{xy.c}$, the distances z and L_v as seen in Figure 3.24.

At the beam side, the lateral stiffness K_v of the rod is included due to the global direction of the rods.

$$K_v = \frac{3mk_v l_{ch}(\lambda_0 + m)}{\lambda_0^4 + 4m\lambda_0^3 + 6m\lambda_0^2 + 6m\lambda_0 + 3m^2} \tag{3.71}$$

$m = d_{net}^4/d_1^4$, where d_{net} represents the diameter in the free length and d_1 is the core diameter of the embedded rod. $\lambda_0 = l_0/l_{ch}$ and $l_{ch} = \sqrt[4]{4E_s \cdot I_s/k_v}$, where k_v is the foundation modulus a laterally loaded rod.

The compliance terms at beam side is formulated as:

$$S_{xx.bi} = \frac{s_{bi}^2}{K_{v.bi}} + \frac{c_{bi}^2}{K_{ax.bi}} \tag{3.72}$$

$$S_{xy.b1} = s_{b1} \cdot c_{b1} \left(\frac{1}{K_{v.b1}} - \frac{1}{K_{ax.b1}}\right) \qquad S_{xy.b2} = s_{b2} \cdot c_{b2} \left(\frac{1}{K_{ax.b2}} - \frac{1}{K_{v.b2}}\right) \tag{3.73}$$

The rotational stiffness at the beam side per plane of rods can then be expressed as:

$$K_{\theta.B} = \frac{z^2}{\left(S_{xx.b1} + S_{xx.b2}\right) + \left(S_{xy.b2} - S_{xy.b1}\right) \cdot \frac{z}{2 \cdot L_v}} \tag{3.74}$$

The stiffness provided by the steel rings are found through numerical analysis by Stamatopoulos et al. (2022) to be 484 kN/mm and 600 kN/mm for the ring in compression and tension, respectively. This leads to the rotational stiffness of connectors:

$$K_{\theta.con} = z^2 \left(\frac{1}{K_{ax.con.1}} + \frac{1}{K_{ax.con.2}} \right)^{-1} \tag{3.75}$$

By combining each component from Eq. (3.70), Eq. (3.74) and Eq. (3.75) as springs in series, the expression for the rotational stiffness of the connection proposed by Stamatopoulos et al. (2022) is:

$$K_{\theta.tot} = \left(\frac{1}{K_{\theta.C}} + \frac{1}{K_{\theta.B}} + \frac{1}{K_{\theta.con}} \right)^{-1} \tag{3.76}$$

For thread angles in the column of 35º for c_1 and c_4 and 55º for c_2 and c_3 the analytical approach coincided with experimental results, only differing with 2%. or thread angles of 55º for c_1 and c_4 and 70º for c_2 and c_3, the rotational stiffness differed more from analytical to experimental. The analytical formulation gave 22.8% higher rotational stiffness for the entire connection, with two planes of rods. The failure for both case was due to splitting in the panel zone of the column, but due to a low number of experimental test no concluding remarks are made.

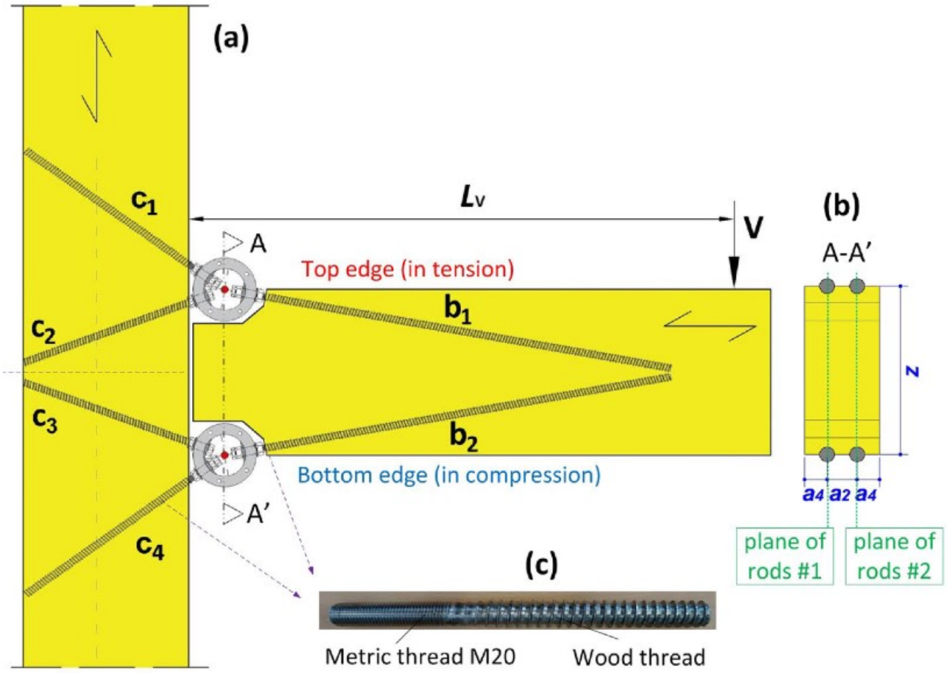

Figure 3.24: Semi-rigid connection from Stamatopoulos et al. (2022).

3.4 Design guidelines for buildings

This section describes the guidelines used for designing buildings published by the European Committee for Standardization (CEN). Every country member of this committee must follow the guidelines and the additional national annexes (CEN, 2002). This thesis is based on the reader having basic knowledge of the Eurocode series, meaning that only a brief description of relevant parts is given.

3.4.1 Eurocode 0 and Eurocode 1

NS-EN 1990 Eurocode 0: Basis of structural design (EC0) and *NS-EN 1991 Eurocode 1: Actions on structures - Part 1-1: General actions - Densities, self-weight, imposed loads for buildings* (EC1-1) describes how actions on structures should be considered and the different safety factors for the different limit state designs (CEN, 2002; CEN, 2009).

The load combination for ULS is set by EC0 (6.10):

$$\sum_{j\geq 1} \gamma_{G,j} G_{k,j}\text{"}+\text{"}\gamma_P P\text{"}+\text{"}\gamma_{Q,1} Q_{k,1}\text{"}+\text{"}\sum_{i>1} \gamma_{Q,i} \psi_{0,i} Q_{k,i} \tag{3.77}$$

where $G_{k,j}$ represents permanent loadings, $Q_{k,1}$ represents the dominating variable load and $Q_{k,i}$ represents other variable loads. γ represents a factor of safety given in EC0 Table NA.A1.2(A) as 1.2 for permanent loadings and 1.5 for variable loadings. ψ reduces other variable loads according to EC0 Table NA.A1.1 and depends on the building category. The imposed load depends on the decided category of use and is given in EC0 Table NA 6.1 and Table NA 6.2.

For accidental limit state (ALS), the load combination is defined by EC0 6.4.3.4(2) for seismic design situations:

$$\sum G_{k,j}\text{"}+\text{"}P\text{"}+\text{"}A_{Ed}\text{"}+\text{"}\sum \psi_{2,i} Q_{k,i} \tag{3.78}$$

where

P is the pre-stressing action

A_{Ed} is the design value of an accidental action, in this case, seismic action

NS-EN 1991-1-3 Eurocode 1: Actions on structures - Part 1-3: General actions - Snow loads (EC1-1-3) describes the procedure to define the snow loads acting on a structure, including drift of snow and other parameters affecting the structure (CEN, 2005a).

NS-EN 1991-1-4 Eurocode 1: Actions on structures - Part 1-4: General actions - Wind actions (EC1-1-4) describes the procedure to calculate the wind loads acting on a structure, including e.g. the geometry and geographical placement (CEN, 2003).

3.4.2 Eurocode 2

NS-EN 1992 Eurocode 2: Design of concrete structures (EC2) applies to designing buildings and in plain, reinforced or pre-stressed concrete and complies with the requirements for the safety and serviceability of structures, the basis of their design and verification given in EC0 and EC1 (CEN, 2014).

3.4.3 Eurocode 3

NS-EN 1993 Eurocode 3: Design of steel structures (EC3) describes the process of evaluating structural elements and buildings in steel. This standardization consists of several parts, whereas Eurocode 3 Part 1-8: Design of joints (EC3-1-8) describes the process of designing steel joints and classifies them in three main categories for unbraced frames (CEN, 2005b):

1. **Pinned**: $S_{j,ini} < EI_b/L_b$
2. **Semi-rigid**: $EI_b/L_b < S_{j,ini} < 25EI_b/L_b$
3. **Rigid**: $S_{j,ini} > 25EI_b/L_b$

where

$S_{j,ini}$ is the initial rotational stiffness of the connection

EI_b is the flexural rigidity of the beam

L_b is the length of the beam

3.4.4 Eurocode 5

NS-EN 1995 Eurocode 5: Design of timber structures (EC5) describes the process of evaluating structural elements in timber. With use in conjunction with EC0 and EC1, EC5 is divided into three parts:

- EC5-1-1: General - Common rules and rules for buildings
- EC5-1-2: General - Structural fire design
- EC5-2: Bridges

In this thesis, EC5 refers to EC5-1-1, and eventual exceptions will be highlighted.

Timber as a material requires additional conditions to the general set of rules, as the material will behave differently under different moisture level, the duration of load, and the direction of the load. These are represented by:

- *Climate class* - Moisture variations
- *Deformation factor* k_{def} - Reduction factor based on the climate class
- *Modification factor* k_{mod} - A correction factor based on load duration and climate class
- *Height factor* k_h - Variation from the reference height of 600 mm
- Different properties perpendicular than parallel to the fiber direction

The general formulation for the stress capacity of timber is found in EC5 (2.4.3)

$$R_d = k_{mod} \frac{R_k}{\gamma_m} \tag{3.79}$$

where

R_k is the characteristic value of resistance

γ_m is the partial factor of safety

For the capacity of timber connections, EC5 8.2.3(3) gives the shear capacity per fastener per shear plan, and the corresponding failure mode according to Johansen's theory. Typical failure modes for connections with steel and timber can be seen in Figure 3.25. For a connection with an arbitrary thick steel plate as the central component of the connection, the failure mode can be calculated using Eq. (3.80)

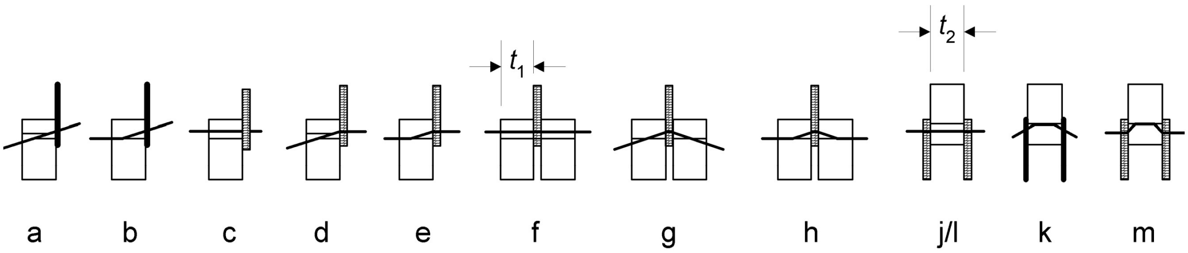

Figure 3.25: Failure modes for connections with steel against timber.

$$F_{v.RK} = \min \begin{cases} f_{h.k}\, t_1\, d & \text{failure mode (f)} \\ f_{h.k}\, t_1\, d \left[\sqrt{2 + \frac{4M_{y.Rk}}{f_{h.k}\, t_1^2\, d}} - 1 \right] + \frac{F_{ax.Rk}}{4} & \text{failure mode (g)} \\ 2.3\sqrt{M_{y.Rk} f_{h.1.k} d} + \frac{F_{ax.Rk}}{4} & \text{failure mode (h)} \end{cases} \tag{3.80}$$

where

$f_{h.k}$ is the characteristic embedment strength of the timber

t_1 is the thickness of the connected timber according to Figure 3.25

d is the diameter of the fastener (bolt, dowel, nail, etc.)

$M_{y.Rk}$ is the characteristic yield moment of the fastener

$F_{ax.Rk}$ is the withdrawal capacity of the fastener. For bolts, this capacity is limited by EC5 8.2.2(2) to be 25% for bolts and 0% for dowels

3.4.5 Eurocode 8

EC8 *NS-EN 1998 Eurocode 8: Design of structures for earthquake resistance* (EC8) describes the process of evaluating structural elements in a building to sustain loads due to earthquake loading. The different methods are described, and the main differences are presented.

EC8 is divided into several parts:

- EC8-1: General rules, seismic actions and rules for buildings
- EC8-2: Bridges
- EC8-3: Assessment and retrofitting of buildings
- EC8-4: Silos, tanks, and pipelines
- EC8-5: Foundations, retaining structures, and geotechnical aspects
- EC8-6: Towers, masts, and chimneys

EC8-1 presents that the building's structure should be designed to retain its integrity and load carrying ability without a local or global collapse in ULS. The national annex NA gives a return period for earthquakes of 475 years in Norway and allows the verification of damage limitation to be neglected. The seismic class for a building is determined by the type of building and the consequences of the building collapsing.

The scale goes from class I (lowest) to class IV (highest), and the recommended class for a certain type of building is presented in EC8-1 Table NA.4(902). An extraction of the complete table is shown in Table 3.5

Table 3.5: Recommended choice of seismic class extracted from EC8-1 Table NA.4 (902).

Type of building	I	II	IIIa	IIIb	IV
Buildings with exceptional consequences of collapse					x
Important infrastructure			(x)	x	
Buildings with persistent crowds			x		
Schools and institutions		(x)	x		
Houses, small warehouses	x				

From EC8-1 NA.3.2.1(5), seismic analysis of buildings in seismic class I-IIIa is not necessary if one of several criteria given by the standard is met, while for seismic class IIIb and IV, seismic analysis is required.

3.4.5.1 Seismic mass

The seismic loading is defined by EC8-1 3.2.4, where the inertia forces should be based on the loadings present in the following load combination

$$\sum G_{k,j} \text{"} + \text{"} \sum \psi_{E,i} \cdot Q_{k,i} \tag{3.81}$$

where

$\psi_{E,i}$ is the combination factor for variable actions

$\psi_{E,i}$ takes into account the probability of the loads acting simultaneously and is defined as:

$$\psi_{E,i} = \varphi \cdot \psi_{2,i} \tag{3.82}$$

where

φ is the modification factor for variable actions defined by EC8-1 Table NA.4.2 as seen in Table 3.6

Table 3.6: Values of φ for calculating ψ_{Ei} EC8 Table NA.4.2 (CEN, 2004).

Type of variable action	**Story**	$\boldsymbol{\varphi}$
Categories A-C	Roof	0.5
	Story with correlated occupancies	0.5
	Independently occupied stories	0.5
Categories D-F		1

3.4.5.2 Methods of seismic analysis

EC8 suggest the categorizing of building structures into *regular* or *non-regular*. This distinction determines the analysis method and allowable simplifications for the method of seismic analysis. For a building to be regular in plan, it must meet all criteria given by EC8-1 4.2.3.2, including symmetry, distribution of stiffness in plan, slenderness of the building in plan, and eccentricity. EC8-1 4.2.3.3 sets criteria for regularity in elevation, including continuous lateral load resisting system, constant lateral stiffness, and limitations regarding setback of stories.

From EC8-1 Table 4.1 seen in Table 3.7, the method of analysis that should be applied is determined based on regularity in plan and elevation.

Table 3.7: Method of analysis based on regularity from EC8-1.

Regularity		Allowed Simplification		Behavior factor
Plan	Elevation	Model	Linear-elastic Analysis	(for linear analysis)
Yes	Yes	Planar	Lateral force	Reference value
Yes	No	Planar	Modal	Decreased value
No	Yes	Spatial	Lateral force	Reference value
No	No	Spatial	Modal	Decreased value

3.4.5.3 Design spectrum

The design spectrum in EC8-1 is a response spectrum similar to Figure 3.13 but can account for seismic actions in the non-linear range by considering the behavior factor q (see Section 3.4.5.7).

The horizontal components of the elastic design spectrum $S_d(T)$ is defined by EC8-1 3.2.2.5(4)P:

$$0 \leq T \leq T_B : S_d(T) = a_g \cdot S \cdot \left[\frac{2}{3} + \frac{T}{T_B} \cdot \left(\frac{2.5}{q} - \frac{2}{3}\right)\right] \tag{3.83}$$

$$T_B \leq T \leq T_C : S_d(T) = a_g \cdot S \cdot \frac{2.5}{q} \tag{3.84}$$

$$T_C \leq T \leq T_D : S_d(T) \begin{cases} = a_g \cdot S \cdot \frac{2.5}{q} \left[\frac{T_C}{T}\right] \\ \geq \beta \cdot a_g \end{cases} \tag{3.85}$$

$$T_D \leq T : S_d(T) \begin{cases} = a_g \cdot S \cdot \frac{2.5}{q} \left[\frac{T_C T_D}{T^2}\right] \\ \geq \beta \cdot a_g \end{cases} \tag{3.86}$$

where

T is the vibration period

a_g is the design ground acceleration on type A ground

T_B is the lower limit of the constant spectral acceleration branch

T_C is the upper limit of the constant spectral acceleration branch

T_D is the value defining the beginning of constant range of the spectrum

S is the soil factor

β is the lower bound factor for horizontal design spectrum

The soil factor S is based on the ground conditions and accounts for transmission of seismic waves from the ground to the building structure.

3.4.5.4 Lateral force method

The lateral force method is a simple linear-elastic method for determining seismic effects. The analysis can be used for buildings whose response is dominated by the fundamental mode T_1 and meet the criteria for regularity. The fundamental mode for a spatial model can be approximated in each main direction by EC8-1 4.3.3.2.2:

$$T_1 = C_t \cdot H^{3/4} \tag{3.87}$$

where

$$T_1 \leq \begin{cases} 4 \cdot T_c \\ 2.0s \end{cases} \tag{3.88}$$

C_t is 0.050 for other structures than steel and concrete space frames

H is the height of the building

The base shear force F_b can then be calculated based on the fundamental period, design spectrum S_d, the total mass of the building m, and correction factor λ.

$$F_b = S_d(T_1) \cdot m \cdot \lambda \tag{3.89}$$

The seismic action effects are then distributed to all stories by mode shapes or assuming linear distribution along the height of the building.

3.4.5.5 Modal response spectrum analysis

Modal response spectrum analysis (MRSA) is a linear elastic method based on the dynamic properties of a structure and shall be applied to buildings as seen in Table 3.7, where each mode contributing significantly to the global response is considered. From EC8-1 4.3.3.3.1(3), the requirements to ensure all significantly contributing modes are considered, either of the following must be considered:

- Cumulative sum of effective modal mass for considered modes should be at least 90% of the total mass of the building
- All modes with effective modal mass greater than 5% of the structure's total mass is considered.

When using a spatial model, this should be considered for each relevant direction. For buildings with significant contributions from torsional modes, these requirements can be hard to satisfy. An alternative way of finding the minimum number k of modes which must be considered is given in EC8-1 4.3.3.3.1(5), where both of the following conditions must be satisfied:

$$k \geq 3 \cdot \sqrt{n} \qquad \text{and} \qquad T_k \leq 0.20\,\text{s} \tag{3.90}$$

where

k is the number of modes considered

n is the number of stories above foundation

T_k is the period of mode k

To find the modal maximum, there are two main method presented. If the response of all modes satisfies $T_j \leq 0.9T_i$, the modes can be regarded as independent, and the maximum seismic response can be found using Square root of sum of squares (SRSS):

$$E_E = \sqrt{\sum E_{Ei}^2} \tag{3.91}$$

where

- E_E is the seismic action effect considered in the analysis
- E_{Ei} is the seismic action effect of the vibration mode i

Otherwise, more accurate procedures of seismic action effect combinations must be adopted, where the Complete Quadratic Combination (CQC) is proposed by EC8-1. Wilson et al. (1981) presented CQC, including all cross-modal terms and considering if the signs of the modal response are opposite or equal. This leads to a more accurate result than SRSS for asymmetric building, as the cross-modal terms, in this case will, be significant. The seismic action effect is found according to:

$$E_E = \sqrt{\sum_i \sum_j E_{Ei} \rho_{ij} E_{Ej}} \tag{3.92}$$

where

ρ_{ij} is the correlation factor, being a function of the loading properties, modal frequencies of the structure and the damping ratio of the structure (Wilson et al., 1981)

MRSA can also account for the structures ability to absorb energy through the behavior factor q, see Section 3.4.5.7.

3.4.5.6 Non-linear analysis

A non-linear analysis (NLA) can be applied where the post-elastic behavior of structural members is utilized. Unlike for linear-elastic analysis, NLA consists of a set of equations with possibly more than one solution and can be complicated and time-consuming. EC8-1 requires the structure to be in ductility class medium or high, see Section 3.4.5.7, for NLA to be performed.

3.4.5.7 Ductility

In earthquake design, the ductile structural elements can absorb the energy released from an earthquake in plasticity areas and is supposed to enhance the human safety of the building. EC8-1 expresses the ductility of the main construction through the behavior factor q.

The level of ductility is separated into three categories based on this in EC8-1. Ductility class low (DCL) refers to structures with low energy absorption, and global elastic analysis and performance of structural elements according to the non-seismic standards, e.g. EC2, EC3 or EC5 for concrete, steel and timber respectively, is sufficient.

Ductility class medium (DCM) and Ductility class high (DCH) refers to structures with the ability to dissipate hysteretic energy from repeated reversed loading without suffering brittle failure. For timber structures, the behavior factor q with examples of typical structures is listed in Table 3.8, adapted from EC8-1 Table 8.1:

Table 3.8: Design concept, behavior factor q and examples of structural types. Adopted from EC8-1.

Design concept and ductility class	q	Examples of structures
DCL	1.5	Cantilevers, beams, arches with two or three pinned joints
DCM	2	Trusses with doweled and bolted joints, mixed structures consisting of timber framing
	2.5	Hyperstatic portal frames with doweled and bolted joints
DCH	3	Nailed wall panels with glued diaphragms, trusses with nailed joints
	4	Hyperstatic portal frames with doweled or bolted joints
	5	Nailed wall panels with nailed diaphragms connected with nails and bolts

An important notice is that EC8-1 NA.5.2.1 removes the possibility of employing behavior factors from DCH, meaning that only values for DCL and DCM can be used in Norway even if the connection fulfills the requirements for DCH.

3.5 Design to disassemble

This chapter describes the theory behind the concept of designing buildings to be dismantled in the future, how different elements and design of connection affect an element's ability to be reused and how the structural parameters are affected.

3.5.1 Introduction to the concept: Why?

The construction industry is responsible for over half of the global resources and more than 30% of the total energy consumption (Iacovidou and Purnell, 2016). This consumption costs a considerable amount of CO_2, and Rose and Stegemann (2018) suggest that sustainable development depends on reducing both the use of resources and the amount of waste produced. This concept is backed by Joensuu et al. (2022), claiming that 15% of global climate emissions originate from the production of new structural elements. If one building is being demolished to make space for a new building, the concept of reusing both structural and non-structural elements will have a positive influence on the carbon-emission (Iacovidou and Purnell, 2016).

An important aspect of reusability is that a reused structural element should have the same quality as new elements to ensure the structural integrity of the building. In addition to cost and risk, this uncertainty is crucial for the implementation beyond niche projects (Rose and Stegemann, 2018). This problem is also highlighted by Niu et al. (2021), who emphasize that the mechanical properties of a reused structural element must be guaranteed for the life span of the new building.

3.5.2 Reused hollow core slabs

The concrete production is responsible for large parts of the carbon emission in the construction industry due to the high consumption (Adesina, 2020). Feidaki and Vasdravellis (2017) suggest that the steel and concrete production is responsible for 15% of the global CO_2 emissions. In Norway, several producers offer steel reinforcement made from reused steel (Autoretur, 2019), and Fugleseth et al. (2020) suggest that reinforcement with 99% recycled steel is available in Norway. However, the average portion of recycled steel is assumed to be 90% when performing Life Cycle Assessment (LCA). The carbon emission from concrete can therefore be said to mainly be caused by the production of Portland cement (Adesina, 2020).

Reppe (2021) suggests that new HCS with an element height emits 141.07 $kgCO_2e/ton$ when deposited at the end of the life cycle and proposes a 68% reduction for Reused HCS (RHCS) with a total emission of 45.55 $kgCO_2e/ton$ when deposited at end of life. Høydahl and Walter (2020) found 89% reduction in phase A1-A4, which excludes the deposition, from 124.9 $kgCO_2e/ton$ for new HCS, to 13.9 $kgCO_2e/ton$ for RHCS. Bleuel (2019) suggests an approximate reduction for HCS 200 from 530 $kgCO_2e$ for new elements to 120 $kgCO_2e$ for reused elements in an office building. For a low-rise residential building, the reduction is 70%, from approximately 500 to 150 $kgCO_2e$. The difference between reused elements from office to residential in Bleuel (2019) is due to extra handling when changing the purpose and demands of the RHCS. The difference between new and reused elements in all cases mentioned is mainly due to removing the production phase for RHCS. An overview of the numbers are shown in Table 3.9.

Table 3.9: Overview of reduction in carbon emission from different resources. All numbers presented are in $kgCO_2e$.

	New HCS	Reused HCS	Reduction in emissions
Reppe (2021)	141.07/ton	45.55/ton	68%
Høydahl and Walter (2020)	124.9/ton	13.9/ton	89%
Bleuel (2019)			
Office	530	120	78%
Low-rise apartment	500	150	70%

Ajdukiewicz et al. (2013) propose that the quality of RHCS when disassembled appropriately, is similarly good to new HCS. Interestingly, Bleuel (2019) highlights that HCS, on average, are used 15 to 30 years before being demolished, while the technical lifespan is at least 200 years, or as suggested by Jensen and Sommer (2018), reusable for three cycles, each cycle of 120 years. Naber (2012) highlights that HCS can be reused when not subjected to loads exceeding normal loading. Eberhardt et al. (2018) propose that 90% of HCS used as floors and 60% of HCS used as roofs are suitable for reuse.

In recent years, there has been researched regarding alternative connections of HCS to obtain stiff diaphragms while the elements remain reusable. Volkov (2019) proposes a solution for interconnecting RHCS seen in Figure 3.26, with steel plates continuously bolted at the top and bottom of the interconnection. As the drawing is not scaled, it should be regarded as a conceptual solution.

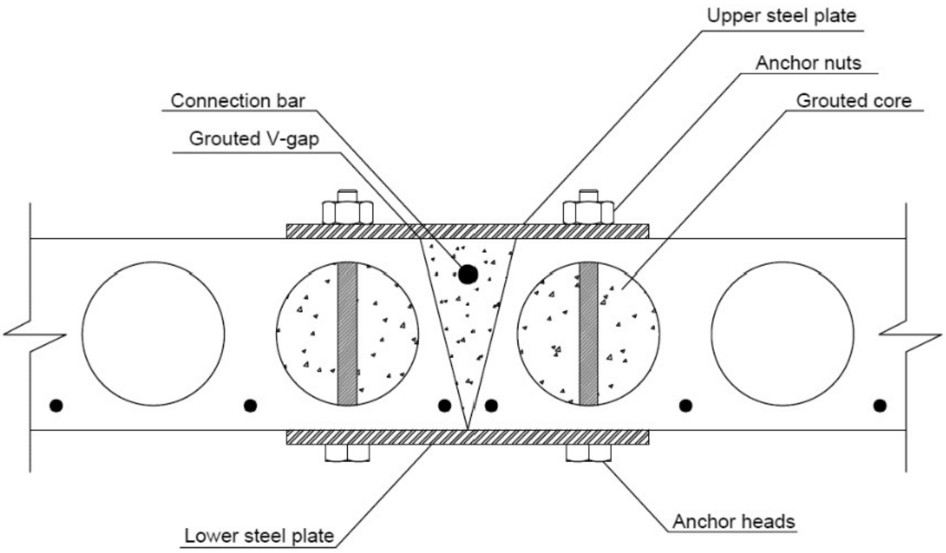

Figure 3.26: Conseptual proposal for interconnection of adjacent HCS (Volkov, 2019).

Volkov (2019) highlights that the advantages of this joint are that the steel plates add ductility to the system, the horizontal shear resistance is good, and the joint is relatively suitable for further reuse. The complex on-site process needed with the drilling of holes for bolts, extra grouting, and unaesthetic look is mentioned, among other things, as drawbacks for this connection.

Al-Ghalib and Ghailan (2020) present a solution adopted from Moynihan and Allwood (2014) to connect concrete planks to steel beams in a demountable manner. The concept is seen in Figure 3.27 and permits reuse of both the concrete planks and the steel beam. The head of a bolt is inserted in the continuous steel channel in the concrete plank, and fastened to a steel beam with a beam clamp.

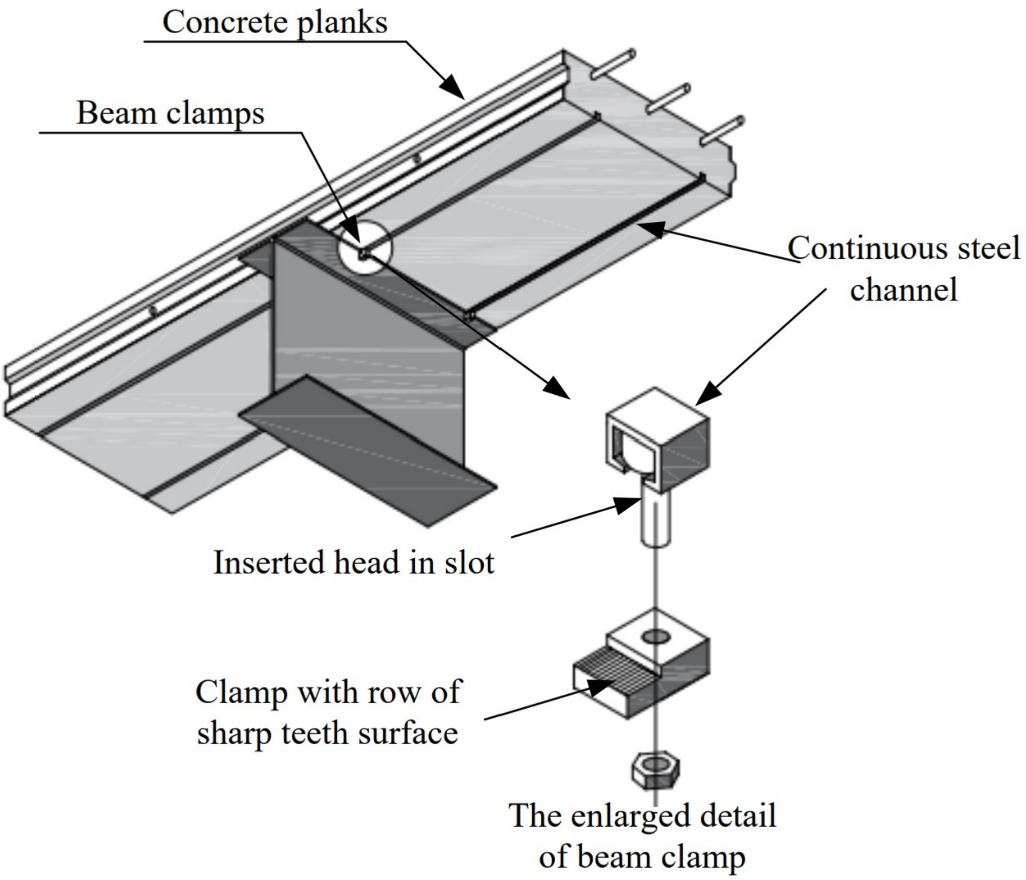

Figure 3.27: Demountable connection, connecting concrete plank and steel beam (Al-Ghalib and Ghailan, 2020).

3.5.3 Reuse of timber

Reusing structural timber as load-bearing elements can be problematic due to the characteristic static fatigue. This phenomenon is caused by the aging of timber, duration, and intensity of load. Niu et al. (2021) suggest that the general view is that bending strength and stiffness is not, or only marginally, affected by this However, the investigation is complex due to the large natural variability of timber. Unlike steel, the demolition of buildings is rough for the structural timber elements and reduces the potential for reuse. This often leads to a down-cycle of high-value products by chipping for fiber- or particleboard (Hradil, 2014).

Whittaker et al. (2019) present that timber elements have great recycling potential, as they can be reprocessed into lamellas for GLT if the element cannot be reused as is. The available research regarding the reuse of GLT elements is limited, while several authors present ways of reinforcing GLT.

Through cyclic accelerated aging treatments, Okada et al. (2020) evaluated the durability of Aqueous polymer-isocyanate adhesive (API) bonded glulam. The durability was estimated from the change in shear strength, showing no decrease in wood failure but a declining shear strength. This was assumed to be caused by the wood cracking and not the deterioration of adhesives. The API bonded glulam also showed greater durability than resorcinol formaldehyde resin (RF) bonded glulam and solid wood when subjected to accelerated aging treatment.

Vahedian et al. (2019) suggest using Fibre Reinforced Polymers (FRP) to improve the mechanical properties of GLT. Sheets of FRP can be externally applied to the bottom part of the beam, as seen in Figure 3.28. The sheets can be made out of different materials, such as Aramid or Carbon (Romani and Blaß, 2001). This is found by Vahedian et al. (2019) to enhance the stiffness of the GLT element up to 64%, as well as the ductility. The possibility of mounting the sheets on already existing elements is the main advantage. The drawback is the unaesthetic look of the processed element.

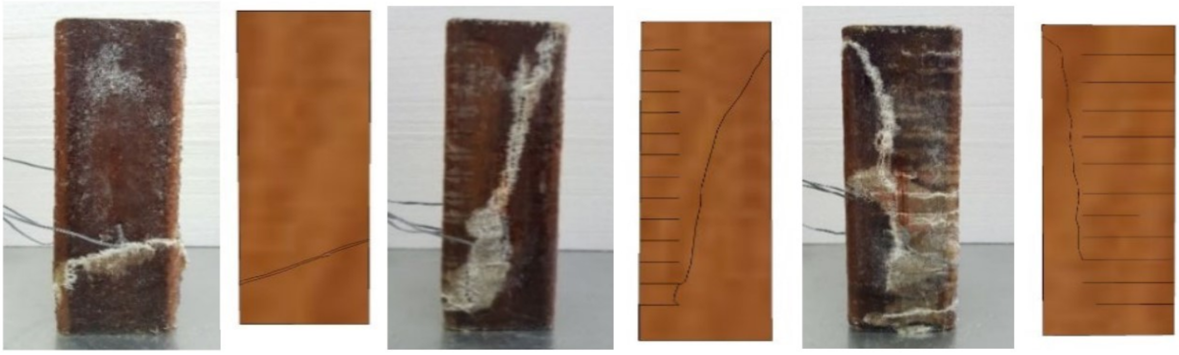

Figure 3.28: Example of FRP applied to GLT element from Raongjant and Jing (2020).

3.5.4 Reuse of timber connections

As presented in Section 3.3.6, there are multiple ways to connect elements when erecting a timber frame building. Every type of connection offers different dynamic properties that will influence a building subjected to both static and dynamic loading. When designing a building for the purpose of reusing, it is important to know the limitations of the different types of connections, and the concept of reusing structural components in timber connections needs further research.

Hradil (2014) investigated the reuse potential of timber elements and connections, comparing them to steel connections by damage modes of timber. An overview of typical timber connections and the damage modes can be seen in Table 3.10.

Reynolds et al. (2013) highlight that a non-linear behaviour under initial load in dowel-type connections leads residual displacements in connections upon removal of the load. This occurs even when dowels are tightly fitted during mounting and is caused by imperfections in the timber surface facing the steel dowel.

Table 3.10: Reusability of timber connections and the connecting elements by Hradil (2014).

Connection	Suitable for reuse	Comment
Glued	No	Hard to separate without damaging elements
Carpentry joints	Sometimes	Notches can cause unfavourable stress concentrations when used differently
Nails, stables	Sometimes	Hard to remove due to bending failure in connecting elements
Screws	Yes	Holes can reduce the effectiveness of the connector
Bolts, dowels	Yes	Checking of holes and cracks are necessary

4. Method

This chapter describes the method used in this thesis. The reference building with preliminary design choices and geometrical adjustments for the analysis is presented along with the structural build-up and applied loads. The input for the numerical model to perform both dynamic analysis and modal response spectrum analysis in SAP2000 is described for each connection-case. Calculation of rotational stiffness and assumptions for the behavior factor of the connection is outlined, and an overview with a comparison of the connections is presented.

4.1 Structural design of the building

This section presents the reference building analyzed in this thesis, the structural considerations, and the dimensions used. The grid system is elaborated, and the modifications on the building's geometry are described and graphically shown. The preliminary dimensions for structural elements are based on loads and actions applied to the structure, leading to the critical load combinations.

4.1.1 Reference building

The reference building to be considered is based on proposed drawings from Multiconsult and a preliminary model seen in Figure 4.1, presenting the northern and southern views of the building. The reference building is an office building of eight levels with a story height of 3.8 m, in addition to three levels under ground. All levels under ground are cast on site, and elements above ground, from levels 1-8, are precast concrete elements. The two upper floors are partly retracted, and there is an overhanging/cantilevered part from axis E6/A1 to E7.

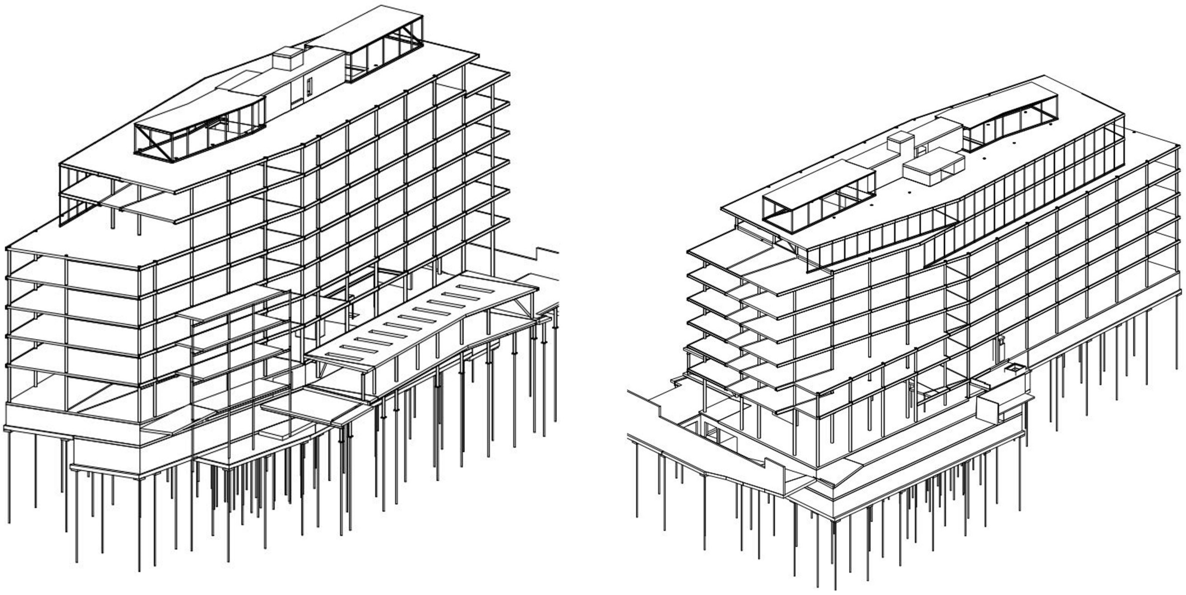

(a) Northern view. **(b)** Southern view.

Figure 4.1: Detailed model of the reference building.

The axis system for the building consists of four main systems. The systems can be seen in Figure 4.2. The global origin (0,0) is set to A1/F4.

1. **Grid A-F**: Grid lines A1-A8 and F1, F4 and F5 in addition to the small system in the middle of the building (1-3, 11-12). The distance between each grid line A1-A7 is 7200 mm and from A7-A8 3900 mm. The distance between F4 and F5 is 8400 mm and F1 is located -17 400 mm vertically from global zero.

   Grid line 1 is located 2050 mm from F4 and grid line 2. Grid line 3 is located 2400 mm from grid line 2. 11 and 12 is placed with equal distance of 3600 mm to A5-A6 and A6-A7, respectively.

2. **Grid B-C**: Grid lines B1-B4 with grid line distance of 7200 mm and C1-C2 with a distance of 8400 mm. Rotated 8^o clockwise relative to A-F. The origin of the system B1/C1 is set to global (54.1,7.415)

3. **Grid C-D**: Grin lines D1-D7 with grid distance of 7200 mm and C3-C4 with a distance of 7950 mm. Rotated 4^o counter-clockwise relative to A-F and origin D7/C3 in global (36,-9)

4. **Grid E-F**: Grin lines E1-E7 with grid distance of 7200 mm for grid line E2-E6, 4450 mm between E1-E2 and 3550 mm between E6-E7. F2-F3 has a distance of 8200 mm and the grid system is rotated 9.5^o clockwise relative to A-F. The origin of the system E1/F2 is set to global (29.4,-17.4).

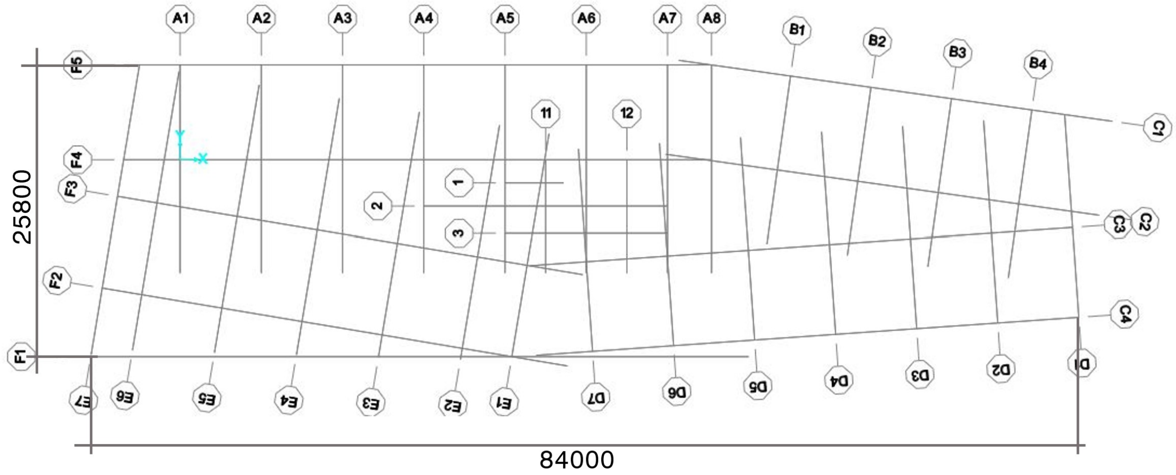

Figure 4.2: Grid system of the reference building.

The triangular extension of the floor level 1 and level 2 seen in Figure 4.1b is included in further calculations, while the external parts seen in Figure 4.1a are ignored, considering only the main building system. The small retractions in levels 6 and 7 are ignored, and the facade line is assumed to follow the same axis as lower stories, meaning axes F2 and C4.

Based on the drawings provided, the height of each story is set to 3.8 for levels 1-8. The top of under ground concrete in level U1 is set to level 0 in the model (K+42.7 m = +0.0 in SAP2000). Southern part of levels 7 and 8 is assumed to end in axis E5. The cantilevered part in Axis E6-E7 is ignored as preliminary tests showed that the natural frequencies of the building were practically unaffected by the removal of this.

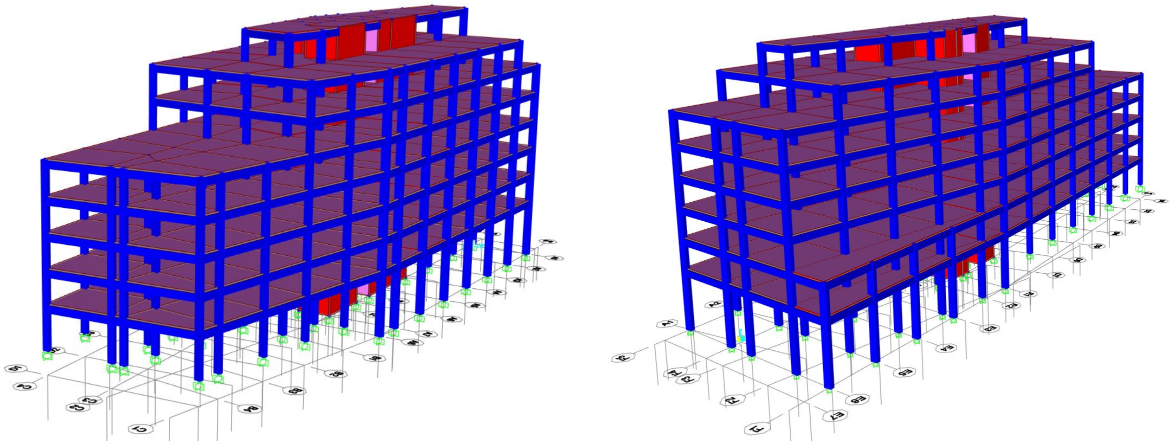

(a) Northern view of SAP2000 model.

(b) Southern view of SAP2000 model.

Figure 4.3: Simplified SAP2000 model of the reference building.

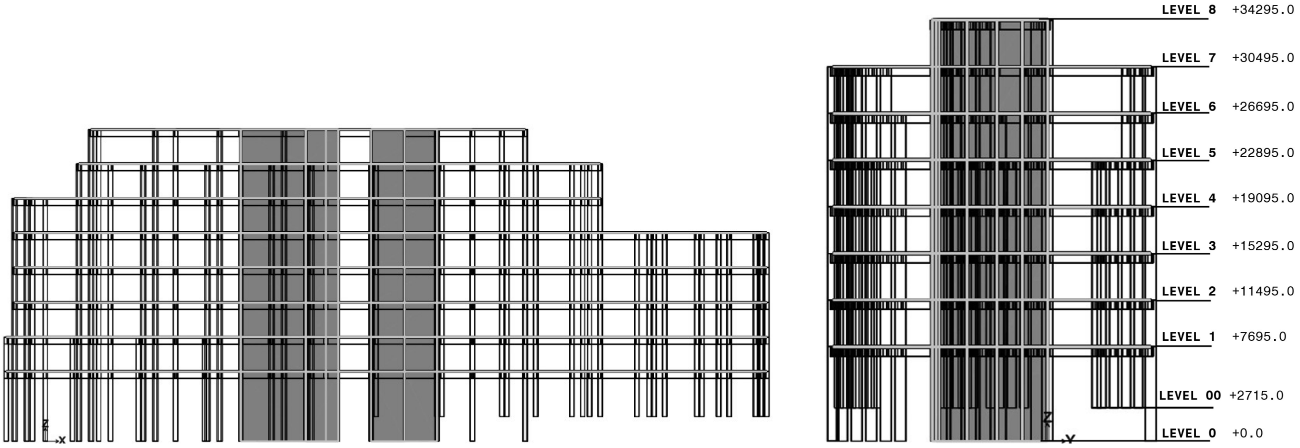

(a) XZ-plane section view.

(b) YZ-plane section view.

Figure 4.4: Section views of simplified model.

4.1.2 Load description

In the following sections, the loads and load categories considered in the modeling of the building are described. The combination of the actions is done as described in Section 3.4.1 for the ULS and according to EC8 for the seismic mass.

4.1.2.1 Dead load

The dead load in the model is the self-weight of the structural elements, meaning the beams, columns, walls, and floors, as seen in Table 4.1. These loads depend on the material's density and dimensions for all elements except the flooring, where the dead load of the elements is applied as a load. Table 4.2 lists additional dead load to be considered in the model, and a line load of 1 kN/m is added to represent the loading from the facade.

Table 4.1: Self-weight of the structural elements

Element	Quality	Self-weight
HCS 200 (NOBI Voss, 2016)	B45	255 + 16 kN/m^2
HCS 320 (NOBI Voss, 2016)	B45	400 + 25 kN/m^2
GLT beams (Crocetti et al., 2015)	GL28h	460 kg/m^3
GLT columns (Crocetti et al., 2015)	GL28h	460 kg/m^3
CLT walls (Awad et al., 2017)	CLT	439 kg/m^3

Table 4.2: Additional dead load to be considered in the modeling.

Placement	**Additional self-weight** $\left[\mathbf{kN/m^2}\right]$	**Comment**
Floor between stair core	4.5	Polished concrete
Floor level 1-7	1.5	Flooring
Roof level 6 and 8	1.7	50 mm sedum green roof
Roof level 7	5.0	250 mm soil for planting

4.1.2.2 Live load

The building is an office building and from EC0 Table NA 6.1 considered building category B, leading to a live load of 3.0 $\mathrm{kN/m^2}$ from Table NA 6.2 on levels 1-7. The roofs on level 2, 5, 6 and level 7 are considered a terrace, leading to building category I from EC0 Table 6.9. This implies a live load of 3.0 $\mathrm{kN/m^2}$; as for building category B. Live load is applied to every indoor floor, while the roof live load is applied to the external part in level 2, 5, 6 and 7.

4.1.2.3 Snow load

The snow loads are calculated following EC1-3. Drift of snow is not considered for simplification, and the characteristic snow load value is assumed to 3.5 $\mathrm{kN/m^2}$ according to EC1-1-3 Table NA.4.1 (901). The form factor of 0.8 is applied, the thermal coefficient $\mu_t = 1$, and the exposure coefficient $\mu_e = 1$. This leads to the snow load:

$$s = 3.5 \cdot 0.8 = 2.8 \quad \mathrm{kN/m^2} \tag{4.1}$$

4.1.2.4 Seismic mass

For all cases presented in this thesis, the modal mass is based on the formulation from EC8-1 (3.17) seen in Eq. (3.81), assuming the seismic mass from the dead load, a portion of the live and snow load. An overview of the factor for each type of load can be seen in Table 4.3.

Table 4.3: Overview of $\psi_{E,i}$ for the type of loadings used to find the seismic mass.

Load	*Structural elements*	*Flooring*	*Sedum*	*Planting soil*	*Live*	*Roof Live*	*Snow*
Type	G	G	G	G	Q_L	Q_L	Q_S
$\boldsymbol{\psi_{E,i}}$	-	-	-	-	0.48	0.48	0.2

4.1.3 Preliminary design of structural timber elements

The preliminary design of the structural elements for the reference building uses various ULS combination to find sufficient dimensions for the beams, columns, and CLT wall panels. A ULS capacity utilization of 70% is assumed appropriate for further calculations, using EC5 and the modification factors based on short-term loading and climate class 1. For GL28h, the characteristic capacities are listed in Table 4.4.

Table 4.4: Characteristic values for GL28h from Crocetti et al. (2015).

Type	Symbol	Value [N/mm^2]
Bending	$f_{m.k}$	28
Tension	$f_{t.0.k}$	22.3
Tension perp.	$f_{t.90.k}$	0.5
Compression	$f_{c.0.k}$	28
Compression perp.	$f_{c.90.k}$	2.5
Shear	$f_{v.k}$	3.5
E-modulus parallel to grain	E_0	12600
E-modulus perp. to grain	E_{90}	300

The highest point reaction force was approximately 5400 kN in joint 566, located in axis A3/F4. Based on this, a GLT column of quality GL28h with dimensions of 900x480 mm is used for columns located from axis A1-A8. For columns from axis B1-B4 located where a lower story height in the bottom floor is present, the maximum point load is approximately 5000 kN in joint 933, located in axis C3/D5. This gives a column dimension of 480x720 mm. For the beams, the highest load considered is found for the pinned case in beam 576, located at C3/D4-D5, with a bending moment 79 kN/m. This gives a beam dimension of 765x480 mm.

4.2 Input for numerical model

This section presents the inputs in SAP2000, highlighting the material properties defined and input that is relevant for the seismic analysis.

4.2.1 Beams and columns

The glulam beams and columns are assumed of quality GL28h. The modeling of this material is done as an orthotropic material with the properties listed in Table 4.5. The modal damping of the GLT elements is set to 1%. The positioning of the beams and columns with the dimensions described in Section 4.1.3 is shown in Figure 4.5.

Table 4.5: Material properties of GL28h, based on properties from Crocetti et al. (2015).

Property	Notation and unit	Value
Longitudinal E-modulus	E_1 $[N/mm^2]$	12600
Transversal E-modulus	$E_2 = E_3$ $[N/mm^2]$	300
G-modulus	$G_{12} = G_{23}$ $[N/mm^2]$	650
Rolling G-modulus	G_{13} $[N/mm^2]$	65
Density	ρ $[kg/m^3]$	460
Poisson's coefficient	v	0.3
Thermal expansion coefficient	a_T	0

4.2.2 Walls

The modeling of 200 mm thick CLT wall panel is done using an orthotropic thin shell element and the material property calculations from Follesa et al. (2013) in Equations (3.44)–(3.47). It is assumed that the layers are of equal thickness of 40 mm, and the same wall panel thickness are used for all panels. The material properties are based on standard timber quality C24, and leads to the shell properties seen in Table 4.6.

Table 4.6: Material properties of thin shell representing CLT with axis as seen in Figure 3.18.

Direction	Thin shell property	Value [N/mm^2]
Vertical	E_y	6 748
Horizontal	E_x	4 622
Out-of-plane	E_z	390
Shear	$G_{xz} = G_{xy} = G_{yz}$	690

4.2.3 Flooring

The floor is modeled as concrete slab with the default material quality C45/55 from SAP2000 listed in Table 4.7. The representation of HCS are modeled as thin shell with a membrane thickness of 200 mm and bending thickness of $0.92 \cdot 200 = 184$ mm. A stiffness modifier *m22* is set to 0.01 to represent the low bending stiffness contribution in transverse direction, creating a one-way slab. The same factors are applied to the roof, with element thickness of 320 mm.

The joint labels in each floor are determined by the *Autolabel* function. The global Z-direction is set to primary direction with the global Y-direction as secondary. This leads to the joint numbers in each story seen in Table 4.8.

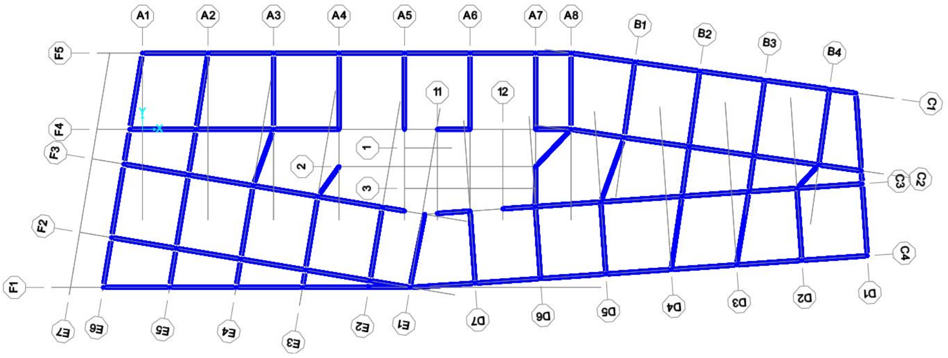

(a) Beams (GL-B-480x765) placement.

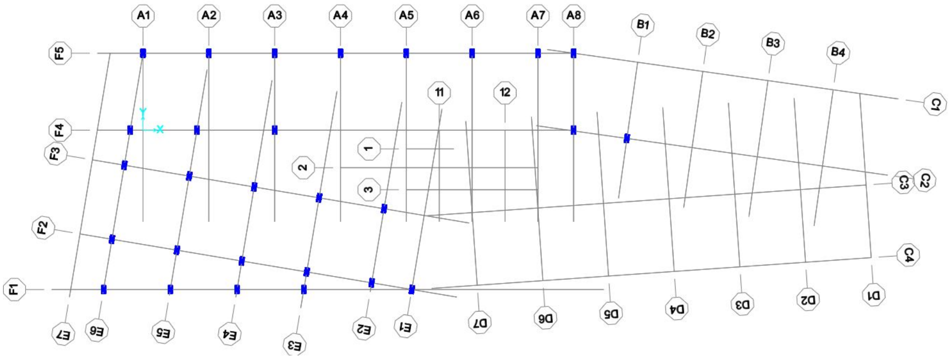

(b) Long columns (GL-C-900x480) placement.

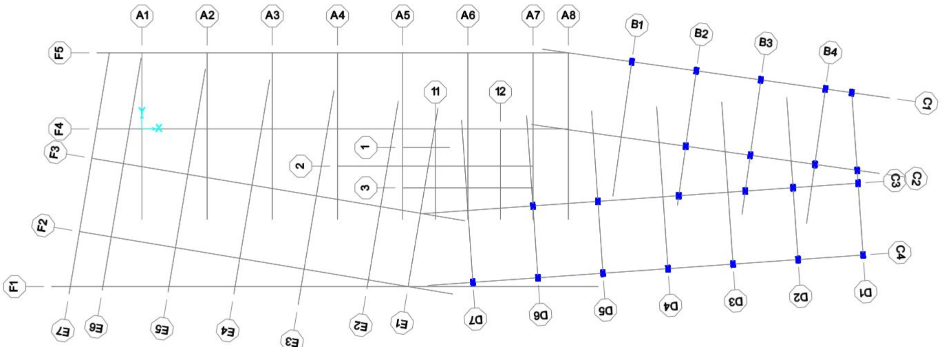

(c) Short columns (GL-CS-720x480) placement.

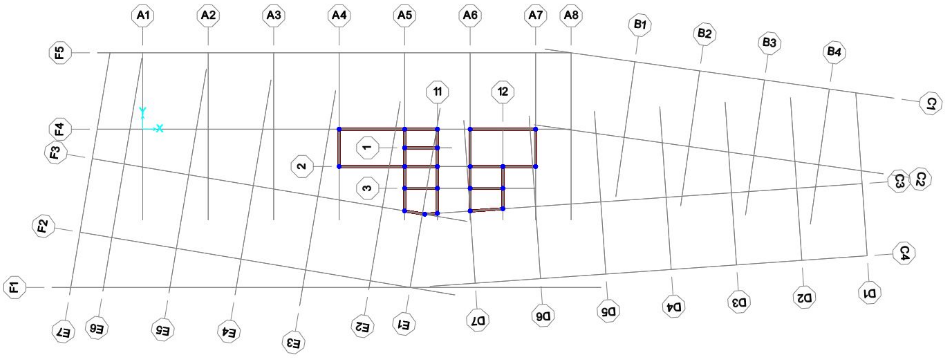

(d) CLT walls (5 Layered 200, 40-40-40-40-40) placement.

Figure 4.5: Placement of structural elements.

Table 4.7: C45 material properties from CSI (2021).

Property	Notation and unit	Value
E-modulus	$E\ [N/mm^2]$	36000
Shear modulus	$G\ [N/mm^2]$	15000
Poisson's coefficient	v	0.2

Table 4.8: Joint numbers per story.

Story	Joint number	Number of joints	Relative story height [mm]
0 / 00	1-72	72	+0.0 / +2 715.0
1	73-149	76	+7 695.0
2	150-226	76	+11 495.0
3	227-298	71	+15 295.0
4	299-370	71	+19 095.0
5	371-442	71	+22 895.0
6	443-502	59	+26 695.0
7	502-554	51	+30 495.0
8	555-586	31	+34 295.0

4.2.4 Meshing

The meshing of HCS are done using a maximum element size of $1.2 \cdot 1.2$ meters for each bay, based on the width of a standard element. The release of moment and twisting between each floor segment, *Area edge release* is used to ensure that the slabs are simply supported and not transferring moments in-between bays. The mesh of a typical floor is shown in Figure 4.6a. The irregularities in the mesh are caused by SAP2000 not meshing with maximum size limitations if the shell segment is anything other than a 4-joint element, but automatically generates the best fitting mesh (Ondrej and Guzman, 2017).

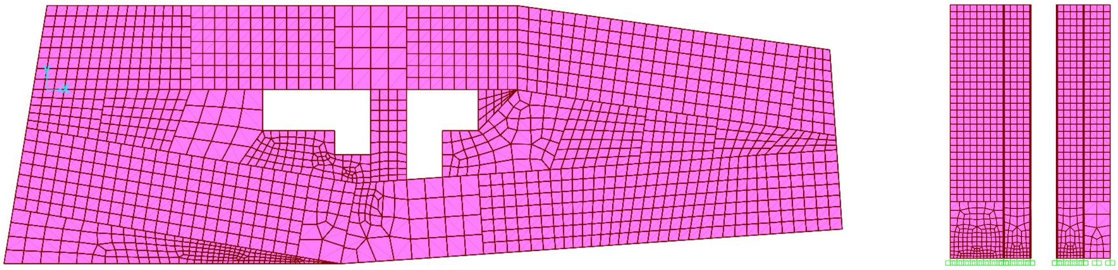

(a) Mesh of typical floor. **(b)** Mesh of CLT core.

Figure 4.6: Mesh of HCS floor and CLT core.

The CLT wall panels are meshed with a maximum element size of $1 \cdot 1$ meters. The SAP2000 function *auto-edge constrain* is used to create connections between wall elements. At the bottom floor a more detailed mesh is required to ensure node connectivity between rigid supports and the wall elements, as can be seen in Figure 4.6b.

Beams and columns are meshed with a maximum element length of 0.2 meters with node creation at interconnections and at intersecting elements.

4.3 Analytical method

The primary goal in this thesis is to investigate how different types of connections affect the seismic response of the reference building. Table 4.14 shows an overview of the different connections used for connecting beams to a column, the rotational stiffness for each connection, and the ductility ratio. All connections considered are based on continuous columns with intermediate beams.

Two reference cases are constructed to decide on a model that reveals differences when the rotational stiffness of the connection is changed. The first case contains pinned-connected intermediate beams. These connections are modeled with beam offset based on the column thickness using automatic connectivity in SAP2000, and the rigid zone factor is set to 0. The second case contains rigid connected intermediate beams. This connection is modeled with a beam offset in the same manner as the pinned case, while the rigid zone factor is set to 1. For the remaining connection-cases, the change in the rigid zone factor did not affect the structure's natural frequencies.

All other connections are modeled as a rotational spring in the beam end using a *Zero-length element*, with significantly higher translational stiffness in all directions to represent rigid constraints for translation. The beam length is decided by the column thickness through automatic connectivity. The rigid zone factor of the connection is set to 0, representing that the fraction of beam offset is considered to have zero rigidity.

Classification of each connection according to EC3-1-8 is done using a reference comparison value $S_{\theta,ref} = EI_b/L_b$, where the flexural rigidity EI_b is found by multiplying the modulus of elasticity about the main axis (E1) retrieved from the GLT beam GL28h properties, with the moment of inertia (I) based on the dimensions of the beam. The length of the reference beams used for classification is dependent on the global direction of the beam, X or Y:

$$S_{\theta,ref,X} = EI_b/L_b = 31\,338.8 \quad \text{kNm/rad} \tag{4.2}$$

$$S_{\theta,ref,Y} = EI_b/L_b = 26\,861.8 \quad \text{kNm/rad} \tag{4.3}$$

4.3.1 Bolted connection

The bolted connection is adopted from Zhou et al. (2021) and transformed to the appropriate size of the beams used for the general case, as seen in Figure 4.7. The build-up is made of continuous columns with intermediate beams, using slotted-in steel plates. The bolts are assumed to be of size M16 and placed at an internal distance of 85 mm. The rotational stiffness is based on EC5 formulation in Eq. (3.49), and the center of rotation (COR) is assumed to be in the center of the bolts connecting the beam to the steel plate. The distance r_i from COR to each bolt is calculated, and the slip modulus K_u for an M16 bolt is calculated:

$$K_{u,i} = \frac{2}{3} \cdot 2 \cdot \frac{\rho_m^{1.5} \cdot d}{23} = 8\,854 \quad \text{N/mm} \tag{4.4}$$

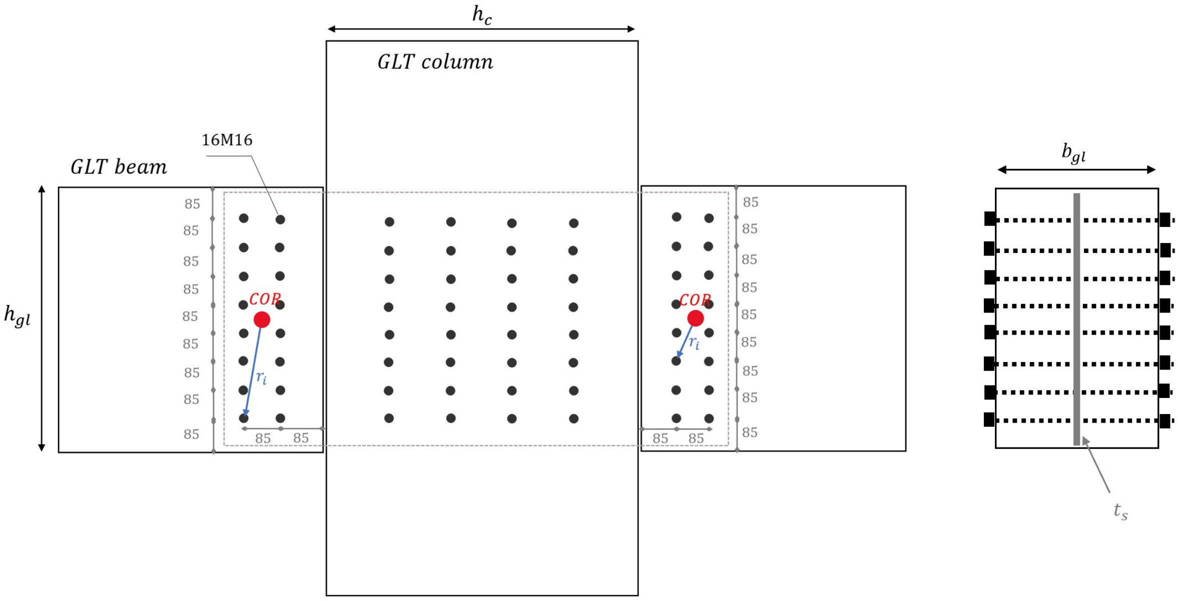

Figure 4.7: Section view of bolted connection adapted in model.

The rotational stiffness of the entire connection can now be found using the distances r_i from COR to the respective fastener

$$K_\theta = \sum K_u \cdot r_i^2 = 5\,629 \quad \text{kNm/rad} \tag{4.5}$$

The classification of the connection according to EC3-1-8 leads to a *pinned* connection. The ductility of the connection is assumed to be low as the diameter of the bolts are $>$ 12 mm, and by EC8-1 8.3(4)a), the connection should not be assumed as energy dissipating. The behavior factor is from this set to $q = 1.5$.

4.3.2 Top-and-seat steel angles connection

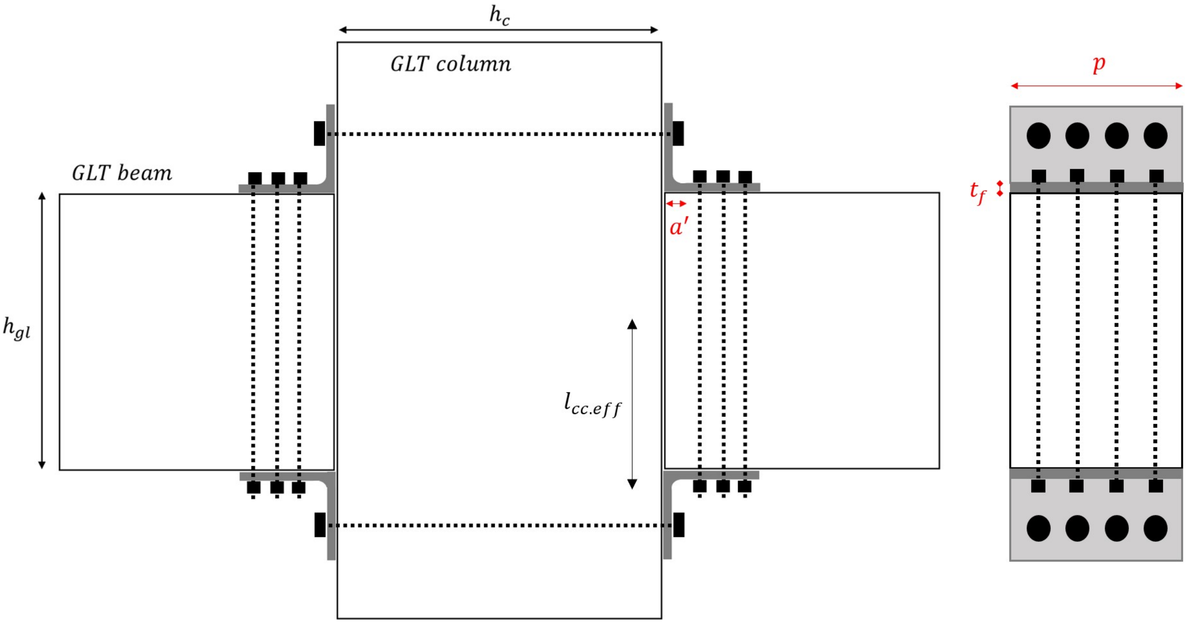

Figure 4.8: Section view of Top-and-seat steel angles connection.

The Top-and-seat steel angles connection is adopted from Zhou et al. (2021), and the rotational stiffness is calculated based on the beam and column dimensions for the reference case. As all columns have their largest depth in the Y-direction, two different rotational stiffnesses must be found: $K_{\theta,C,X}$ for the beams having their main direction in global X-direction (BX) and $K_{\theta,C,Y}$ for beams having their main direction in global Y-direction (BY). For both cases, $h_{gl} = 765$ mm, while the column and bolt properties depend on the beam's direction. A bolt dimension d_{bolt} and angle thickness t_f of 20 mm is assumed, and the effective length of the compressive zone $L_{cc,eff}$ in the GLT column is based on EC5 Figure 6.2, adding 30 mm to half of the GLT beam height. From Eq. (3.55), the column face stiffnesses are found:

$$K_{CC,BX} = \frac{E_{90} \cdot b_c \cdot l_{eff.cc}}{h_{c,BX}} = 204\,750 \quad \text{kN/m} \tag{4.6}$$

$$K_{CC,BY,C} = \frac{E_{90} \cdot b_c \cdot l_{eff.cc}}{h_{c,BY}} = 109\,200 \quad \text{kN/m} \tag{4.7}$$

$$K_{CC,BY,CS} = \frac{E_{90} \cdot b_c \cdot l_{eff.cc}}{h_{cs,BY}} = 13\,650 \quad \text{kN/m} \tag{4.8}$$

The parameter a' in the stiffness of the angle horizontal leg K_t is found based on the minimum distances provided by EC5. For a 20 mm bolt, the minimum distance to a loaded end is $7 \cdot d_{bolt}$. The radius of an angle with thickness $t_f = 20$ mm is $r = 18$

mm. This leads to:

$$a\prime = 20 + 0.8 \cdot 18 = 34.4 \quad \text{mm} \tag{4.9}$$

Meaning that for a steel angle of width $p = 480$ mm:

$$K_t = \frac{E_s \cdot p \cdot t_f}{a\prime} = 55\,813\,953.5 \quad \text{kN/m} \tag{4.10}$$

The Hollo-bolt stiffness K_{HB} formulation in Eq. (3.53) depends on the number of bolts provided to the connection. For a timber structure, traditional bolts are used. Following the assumed bolt diameter, a maximum number of bolts N_b = 4 is decided from the width of the GLT beam. The length of the bolt L_b is dependent on the column thickness. For BX a bolt length of 480 mm provides enough length, while for BY, a bolt length of 900 mm is necessary for the part left of gridline B1 seen in Figure 4.2 and a length of 720 mm for the right part. This leads to three different K_{HB}, and as a consequence of this, three different rotational stiffnesses K_θ. An overview of the stiffness for each component in the three different scenarios can be seen in Table 4.9 and the placement in the plan can be seen in Figure 4.9.

The ductility of this connection is set to not fulfill the requirements for medium ductility and the behaviour factor is set therefore set $q = 1.5$.

Table 4.9: Overview of stiffness components in the Top-and-seat steel angles connection. All numbers in kN/m, except K_θ in kNm/rad.

Connection	K_{cc}	K_{HB}	K_t	K_{top}	K_{bottom}	$\mathbf{K_\theta}$
BX	204 750.0	523 598.8	55 813 953.5	146 804.5	204 001.6	**49 960.7**
$\mathbf{BY_c}$	109 200.0	279 252.7		78 391.9	108 986.7	**26 683.8**
$\mathbf{BY_{cs}}$	136 500.0	349 065.9		83 055.0	136 167.0	**30 190.9**

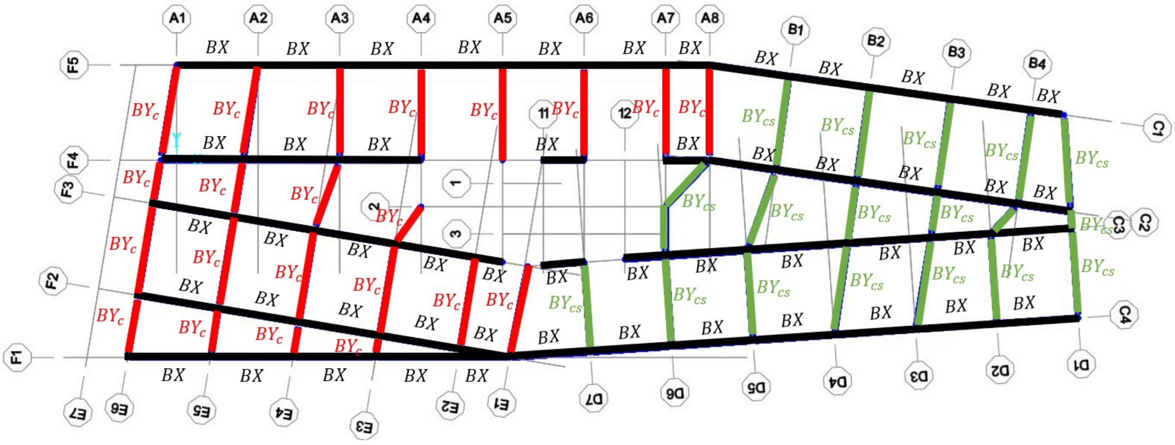

Figure 4.9: Placement of Top-and-seat rotational stiffnesses according to Table 4.9.

4.3.3 Epoxied-in steel rods connection

The Epoxied-in (or glued-in) steel bars-connection is adopted from Fairweather (1992), where the placement of the bars can be seen in Figure 4.10, with two layers of rods in the two outermost glued layer and an additional plane in the middle of the cross section. The rotational stiffness is based on the equations from Yang et al. (2016), where, at the top part, only the glued-in rods are assumed to provide stiffness. The elongation length L_b, is found using Eq. (3.62). The glued-in rods are assumed to have $E_{rod} = 200$ GPa, $\Phi_{rod} = 16$ mm, while the epoxy quality is listed in Table 3.4, assuming a thickness of epoxy layer $t_{epoxy} = 2$ mm. The outer penetration lengths are set to $l_{pen.o} = 400$ mm and inner penetration length $l_{pen.i} = 300$ mm.

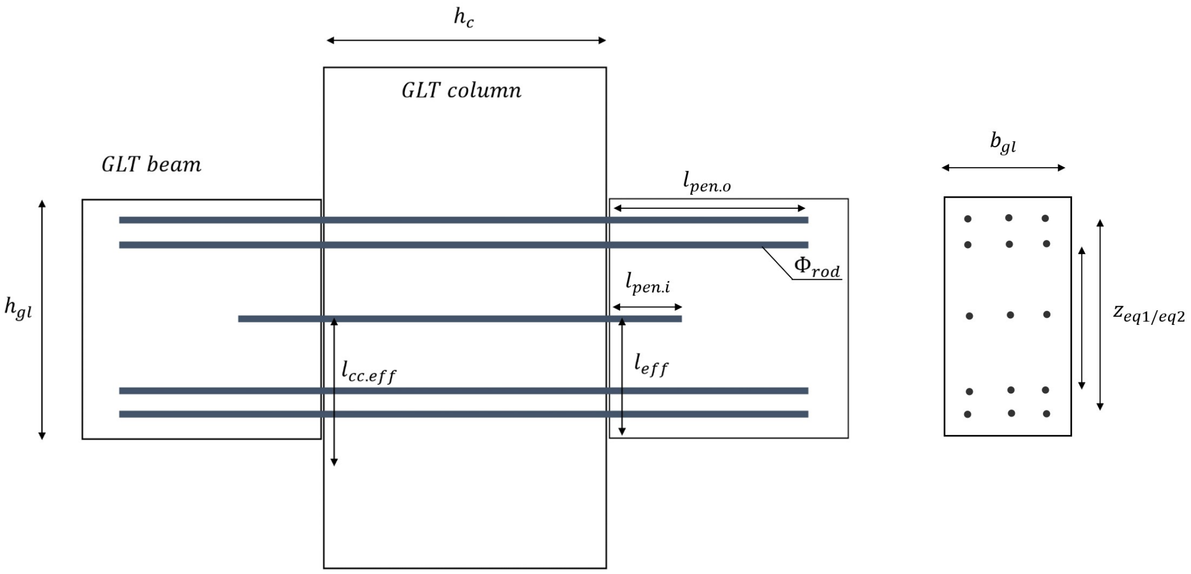

Figure 4.10: Section view of Epoxied-in (glued-in) steel rods connection.

This leads to the following top initial stiffness:

$$K_{t,i} = K_{rod,i} = \frac{2.0 \cdot E_{rod} \cdot A_{rod}}{L_{rod}} = 6\,016\,888.2 \quad \text{kN/m} \tag{4.11}$$

For the compressive zone in the bottom part, the glued-in rod, column and beam face, and the column in shear are assumed to provide stiffness. The column face stiffness is already found in Equations (4.6)–(4.8). The beam face stiffness is found according to Eq. (3.58), assuming properties of the timber from Table 4.4 and the effective area of half the beam cross-sectional area.

$$K_{bc} = \frac{E_{w.0}\sqrt{b_{eff} l_{eff}}}{\beta} = 1\,349\,730.0 \quad \text{kN/m} \tag{4.12}$$

The shear stiffness K_{cs} of the columns are defined using Eq. (3.59), assuming shear modulus from Table 4.4 distance $z_{eq} = 630$ mm. In the same manner as for K_{cc}, two different values are required, both having a width $b_c = 480$ mm:

$$K_{cs,BY,long} = \frac{G_w \cdot h_{c,BY} \cdot b_c}{z_{eq}} = 624\,000 \quad \mathrm{kN/m} \tag{4.13}$$

$$K_{cs,BY,short} = \frac{G_w \cdot h_{cs,BY} \cdot b_c}{z_{eq}} = 499\,200 \quad \mathrm{kN/m} \tag{4.14}$$

This leads to the following compressive stiffnesses:

$$K_{c,1} = \frac{1}{{}^{1}\!/K_{rod} + {}^{1}\!/K_{cs,BY,long} + {}^{1}\!/K_{cc,1} + {}^{1}\!/K_{bc}} \tag{4.15}$$

$$K_{c,2} = \frac{1}{{}^{1}\!/K_{rod} + {}^{1}\!/K_{cs,BY,long} + {}^{1}\!/K_{cc,2} + {}^{1}\!/K_{bc}} \tag{4.16}$$

$$K_{c,3} = \frac{1}{{}^{1}\!/K_{rod} + {}^{1}\!/K_{cs,BY,short} + {}^{1}\!/K_{cc,1} + {}^{1}\!/K_{bc}} \tag{4.17}$$

$$K_{c,4} = \frac{1}{{}^{1}\!/K_{rod} + {}^{1}\!/K_{cs,BY,short} + {}^{1}\!/K_{cc,3} + {}^{1}\!/K_{bc}} \tag{4.18}$$

Using Eq. (3.56), the rotational stiffnesses for each connection can be found, and an overview of the connection properties can be seen in Table 4.10, and the color-coded placement in the typical plan can be seen in Figure 4.11.

Table 4.10: Overview of stiffness components in the Epoxied steel rods connection with 4 rods in each horizontal plan. All numbers in kN/m, except $K_{\theta.con}$ in kNm/rad.

Connection	$K_{grt.i}$	K_{bc}	K_{cs}	K_{cc}	K_{top}	K_{bot}	$\mathbf{K}_{\boldsymbol{\theta}}$
E1	6 016 888.2	1 349 729	624 000.0	204 750.0	36 101 329.2	135 251.1	**53 480.8**
E2				109 200.0		85 710.7	**33 938.0**
E3			499 200.0	204 750.0		128 298.9	**50 741.5**
E4				135 500.0		97 691.5	**38 669.1**

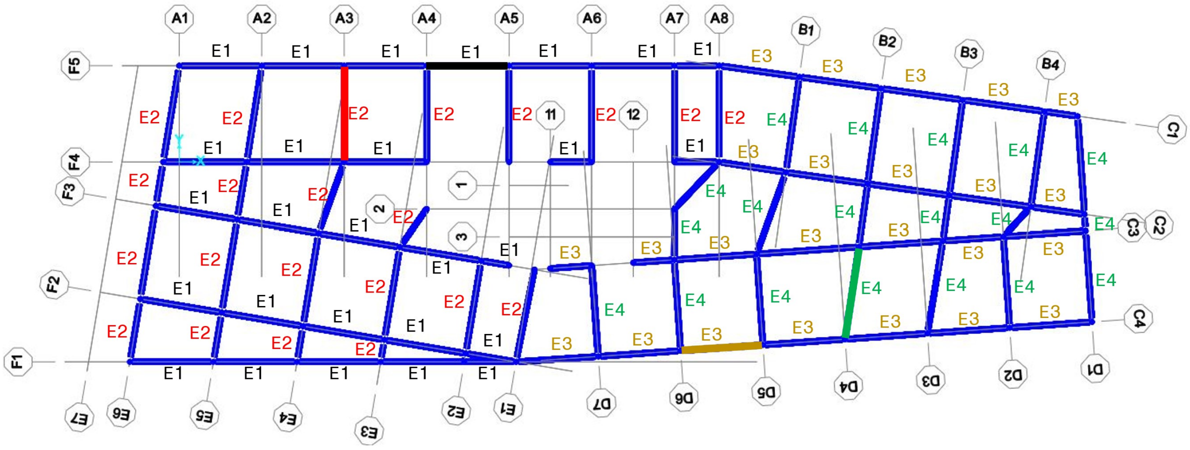

Figure 4.11: Placement of rotational stiffnesses according to Table 4.10.

This connection is design for ductile failure in the steel rods and from this the behavior factor for DCM can be used from EC8-1 Table 8.1, leading to $q = 2.5$

4.3.4 Inclined threaded rods and steel rings connection

The Inclined threaded rods with steel rings connection is adopted from Stamatopoulos et al. (2022) to fit the dimensions of structural elements in the reference building. In the same manner as for Top-and-seat steel angles connection, three different rotational stiffnesses are found to account for the directional dimensions of the columns, $\mathbf{SR_X}$, $\mathbf{SR_{Y.C}}$ and $\mathbf{SR_{Y.CS}}$. The material properties of rods and timber are set similar to rods used for Epoxied-in steel bars, while the dimensions of the rods are listed in Table 4.11.

Table 4.11: Dimensions of rods adopted from Stamatopoulos et al. (2022).

Dimensional property	Value
d_{rod}	22 mm
d_1	16.1 mm
d_{net}	18 mm

The rods is placed with an angle $\alpha_{c1} = \alpha_{c4} = 35^{\text{o}}$ and $\alpha_{c2} = \alpha_{c3} = 55^{\text{o}}$ in the column, and with the angles $\alpha_{b1} = \alpha_{c2} = 10^{\text{o}}$ in the beam. Outer rods are assumed to go through half the column thickness h_{col}, while inner rods have a penetration depth of $1/4 \cdot h_{col}$, as seen in Figure 4.12.

As the beams in the reference building are subjected to uniformly distributed load and not a point load, a reconfiguration of the stiffness components in Eq. (3.70) and

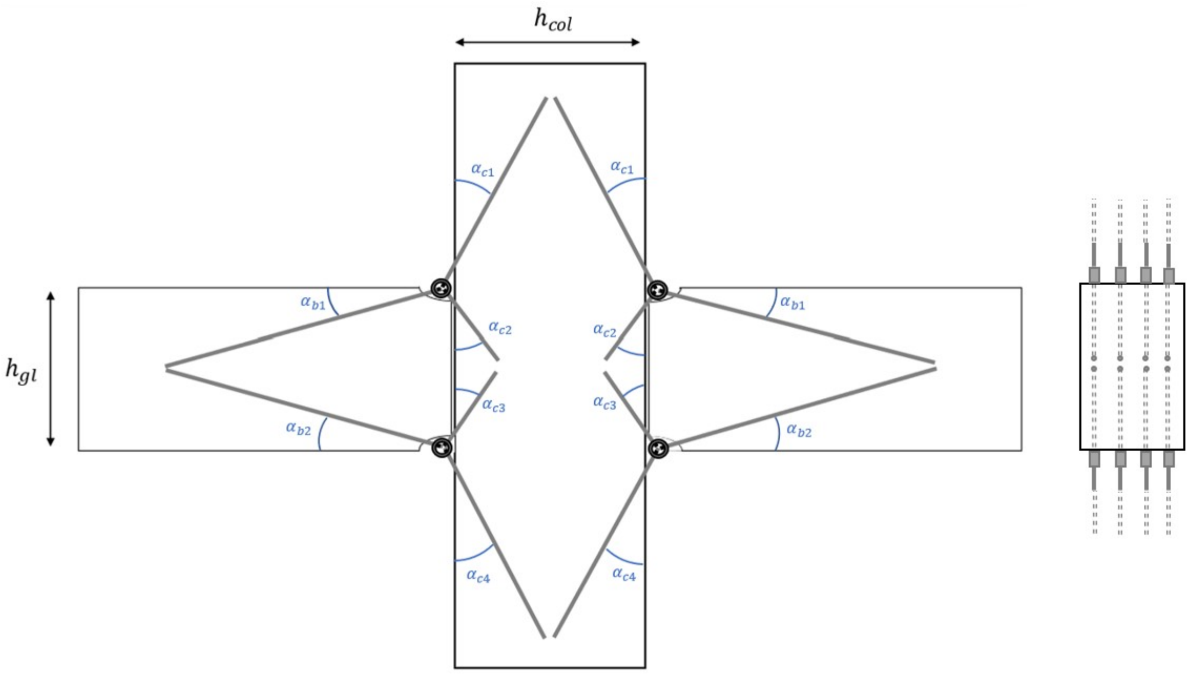

Figure 4.12: Section view of connection with Inclined threaded rods and steel rings.

Eq. (3.74) is necessary. By assuming the following forces in the connection:

$$\begin{Bmatrix} F_x \\ F_y \end{Bmatrix} = \frac{1}{n} \begin{Bmatrix} M/z \\ V/2 \end{Bmatrix} \tag{4.19}$$

Formulas for reaction forces in a clamped beam with uniformly distributed load are known from statics:

$$M = \frac{q \cdot L^2}{12} \qquad V = \frac{q \cdot L}{2} \tag{4.20}$$

This leads to the stiffness components:

$$K_{\theta.C} = \frac{z^2}{\left(S_{xx.c}^{(c1-c2)} + S_{xx.c}^{(c3-c4)}\right) + \left(S_{xy.c}^{(c3-c4)} - S_{xy.c}^{(c1-c2)}\right) \cdot \frac{3z}{L_b}} \tag{4.21}$$

$$K_{\theta.B} = \frac{z^2}{\left(S_{xx.b1} + S_{xx.b2}\right) + \left(S_{xy.b2} - S_{xy.b1}\right) \cdot \frac{3z}{L_b}} \tag{4.22}$$

where L_b is the length of the beam.

Three values of stiffness for the column and beam side is necessary to account for the directions. The height of the columns h_{col} and length of the connected beams L_b are listed in Table 4.12 for each case.

Table 4.12: Beam length, column height and z for each case with Inclined threaded rods.

Connection	Beam length L_b [mm]	Column height h_{col} [mm]	z [mm]
SRX	7200	480	765
SRY_C	8400	900	
SRY_CS	8400	720	

The stiffness of the connectors is assumed equal to connectors from Stamatopoulos et al. (2022); $K_{ax.con.tension} = 484$ kN/mm and $K_{ax.con.compression} = 600$ kN/mm. This leads to the stiffness component from the steel rings:

$$K_{\theta.con} = z^2 \cdot \left(\frac{1}{K_{ax.con.tension}} + \frac{1}{K_{ax.con.comp}} \right) = 156\,779.8 \quad \text{kN/m} \tag{4.23}$$

By combining the stiffness components using Eq. (3.76), the rotational stiffness for each connection K_θ is found. The values are listed in Table 4.13.

Table 4.13: Overview of stiffness components for Inclined threaded rods connection.

Connection	$K_{\theta.C}$	$K_{\theta.B}$	$K_{\theta.con}$	$\mathbf{K}_\theta$
SRX	16 873.5	84 264.3	156 779.8	**51 606.0**
SRY_C	22 304.5	59 085.8		**58 705.4**
SRY_CS	20 216.7	59 085.8		**54 970.0**

As the failure modes in the experimental testing by Stamatopoulos et al. (2022) show compressive failure in the column, the ductility of the connection is assumed to be relatively low. This leads to a behavior factor $q = 1.5$.

4.3.5 Overview of connections

Table 4.14 presents an overview of the rotational stiffnesses calculated along with the considered ductility ratio for each case and the classification of rigidity according to EC3.

Table 4.14: Overview of connections applied in the numerical model.

Connection	Rotational stiffness [kNm/rad]	Behaviour factor q	EC3 classification
Pinned	0	1.5	Pinned
Rigid	∞	1.5	Rigid
Bolted w/ slotted steel plate	5 629.0	1.5	Pinned
Top-and-seat steel angles	49 960.7 26 683.8 30 190.9	1.5	Semi-rigid
Epoxied-in steel rods	53 480.8 33 938.0 50 741.5 38 669.1	2.5	Semi-rigid
Inclined threaded rods w/ steel rings	51 606.0 58 705.4 54 970.0	1.5	Semi-rigid

4.4 Modal Response Spectrum Analysis

The Modal Response Spectrum Analysis (MRSA) is performed using the integrated response spectrum function in SAP2000. One case for each connection is created, implementing the respective behavior factors of the connections previously described. This gives to two different design acceleration response spectra, shown in Figure 4.13.

The soil is assumed as loose-to-medium cohesionless soil giving the ground type D, with parameters describing the elastic response spectrum seen in Table 4.15. As the building is located in Oslo, EC8-1 Table NA.3.2 (902) gives the reference peak ground acceleration (PGA) for the seismic zone as $a_{gR} = 0.3\,\text{m/s}^2$. For seismic class IIIa, the importance factor $\gamma_I = 1.25$. This leads to the ground acceleration a_g:

$$a_g = 1.25 \cdot 0.3 = 0.375 \quad [\text{m/s}^2] \tag{4.24}$$

Table 4.15: Parameters for Type 2 elastic response spectrum and ground type D.

Ground Type	S	T_B (s)	T_C (s)	T_D (s)
D	1.8	0.10	0.3	1.2

Two load cases are created by use of *Response spectrum function*, one for global X (E_{Edx}) and one for global Y (E_{Edy}). The modal combination is set to CQC method to account for coupled modes. The horizontal effect of the seismic loading is done according to EC8-1 4.3.3.5.1 with the two load combinations:

$$E_{Edx}\,''+''\,0.3E_{Edy} \quad \text{and} \quad 0.3E_{Edx}\,''+''\,E_{Edy} \tag{4.25}$$

The absolute drift resultant is found for both combinations with the directional components U1- (Global X) and U2- (Global Y) direction. The ID is found for each story, evaluating it against the limits from EC8-1. As damage limitation calculation is not necessary in Norway, the recommended value for the reduction factor is used: $v = 0.4$. The story heights used are according to Figure 4.4a, and the ductility factors are set equal to the behavior factors used in the respective Response Spectra. The limits are displayed in Table 4.16.

Table 4.16: Interstory drift limits based on EC8-1 formulation.

		Interstory drift limits [mm]	
Story	h [mm]	q = 1.5	q = 2.5
1	7695	128.25	76.95
2-8	3800	63.33	38.00

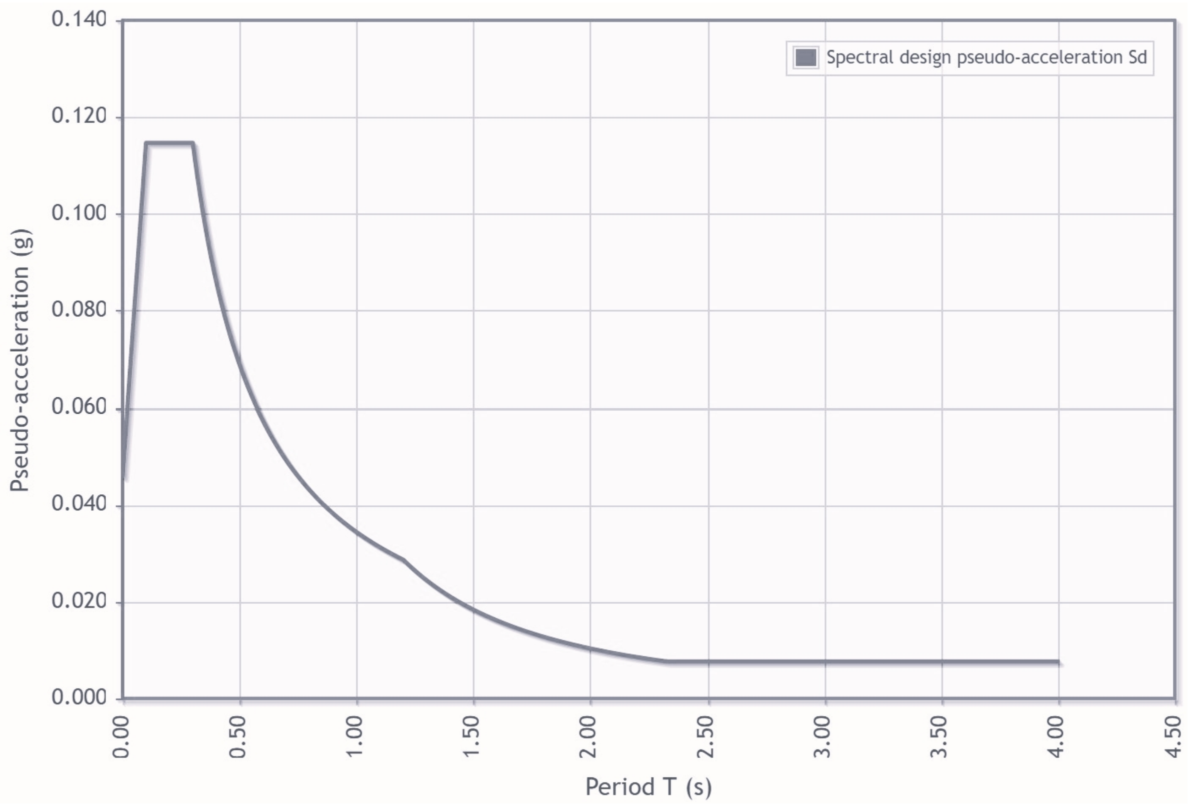

(a) Design response spectrum with behavior factor $q = 1.5$.

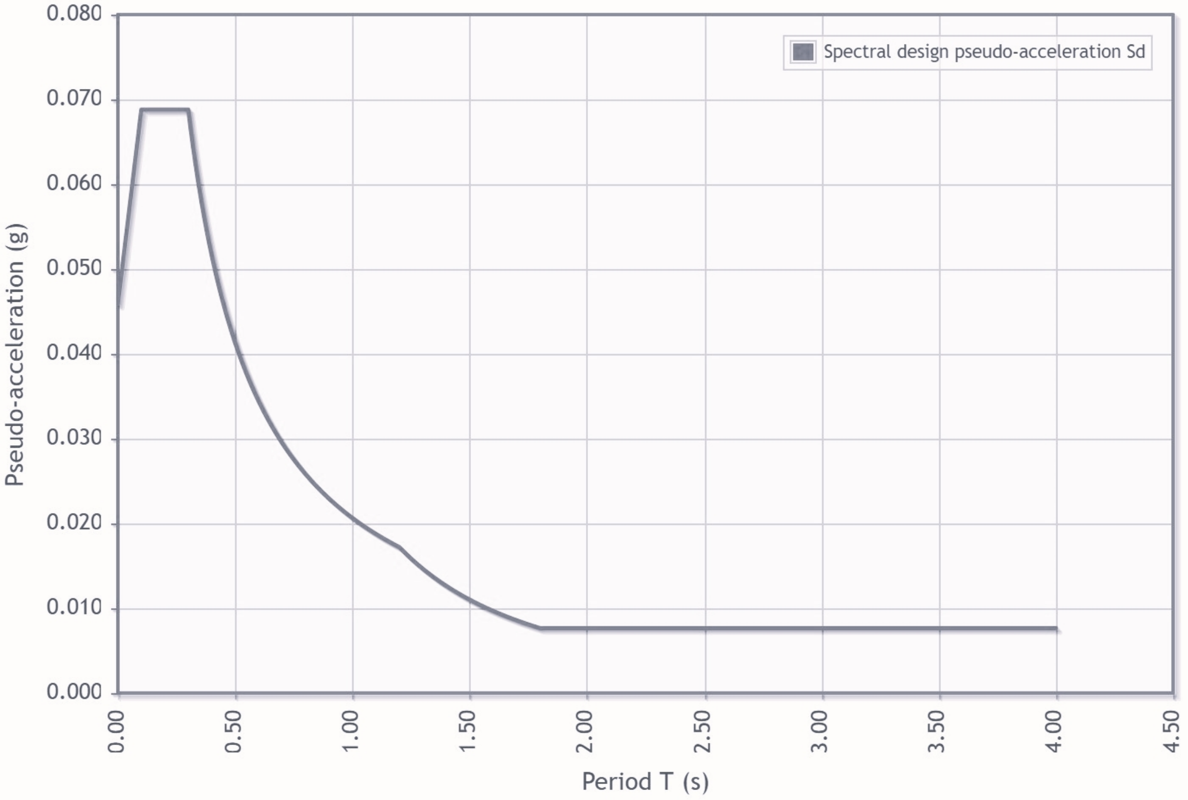

(b) Design response spectrum with behavior factor $q = 2.5$.

Figure 4.13: Design response spectra for the applied behavior factors.

5. Results

This chapter present and describes the results from each model in Chapter 4. The modal analysis is presented, with the period and corresponding mass participation ratio listed in a table, along with a graphical view of the first four modes for each case. The modal shapes are scaled to increase the visibility of the different mode shapes, and the descriptive notation X and Y refer to the global X and global Y direction, respectively.

The modal response spectrum analysis results are further presented with a contour plot of the resultant displacements. The average floor absolute drift (AD) and interstory drift (ID) are presented in the two global main directions for each case.

5.1 Modal analysis

In this section, the results from the modal analysis are presented. For each connection-case, a table presents the periods, the main direction of the mode, the mass participation ratios for each mode in the three main directions $M_{Eff.Ux}$, $M_{Eff.Uy}$ and $M_{Eff.Rz}$. The cumulative sum of the participation ratios in each direction are presented, and the mode number where the directional participation ratio exceeds 90% is highlighted in red. The scaled graphical view of the first four modes is presented for each connection-case, with the corresponding period.

5.1.1 Pinned connection

For the pinned connection-case, the mode shapes can be seen in Figure 5.1. The participation factors for each mode are presented in Table 5.1. Mode 1 is classified as torsional and the second mode is translational in Y. Mode 3 is translational in X-direction, and mode 4 is the second torsional mode. At mode 6, the participation ratio in each main direction exceeds 90%.

Table 5.1: Overview of the modes giving mass participation ratio $\geq$ 90% for pinned case.

			Participation ratio					
Mode	**Type**	$\mathbf{T_n}$	$\mathbf{M_{Eff.Ux}}$	$\sum\mathbf{M_{Eff.Ux}}$	$\mathbf{M_{Eff.Uy}}$	$\sum\mathbf{M_{Eff.Ux}}$	$\mathbf{M_{Eff.Rz}}$	$\sum\mathbf{M_{Eff.Uz}}$
1	Torsional	2.810	0.1%	*0.1%*	0.0%	*0.0%*	70.4%	*70.4%*
2	Trans Y	1.442	1.1%	*1.2%*	76.4%	*76.4%*	0.0%	*70.5%*
3	Trans X	1.286	78.2%	*79.4%*	1.1%	*77.5%*	0.1%	*70.6%*
4	Torsional	0.794	0.1%	*79.5%*	0.0%	*77.5%*	17.5%	*88.1%*
5	Trans X	0.415	12.1%	91.5%	1.4%	78.9%	0.0%	88.2%
6	Trans Y	0.403	1.5%	93.0%	12.5%	91.4%	0.1%	88.3%

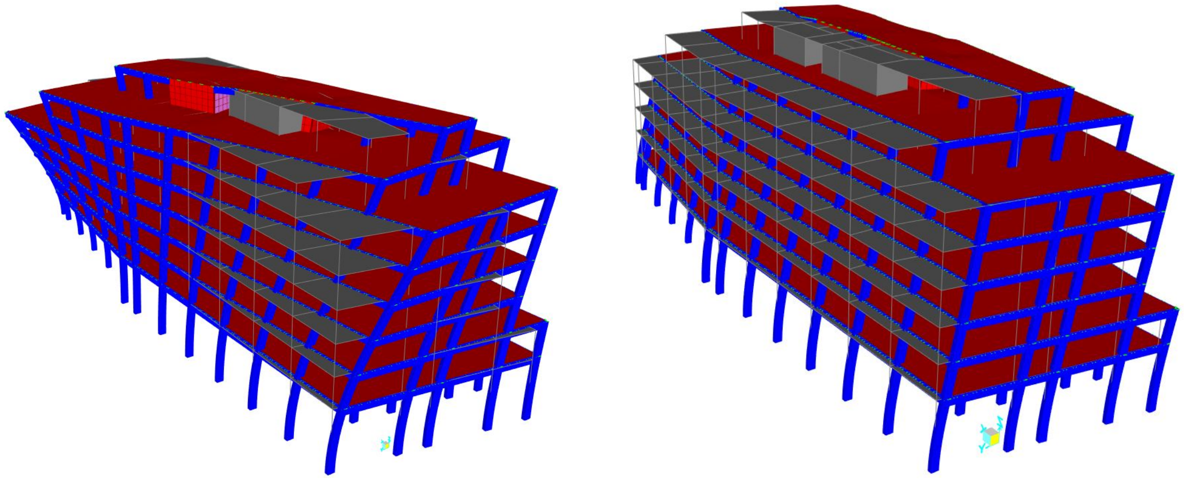

(a) Mode 1, scaled 400. $T_{n.1} = 2.810$ s. Torsional mode.

(b) Mode 2, scaled 400. $T_{n.2} = 1.442$ s. Translation in Y.

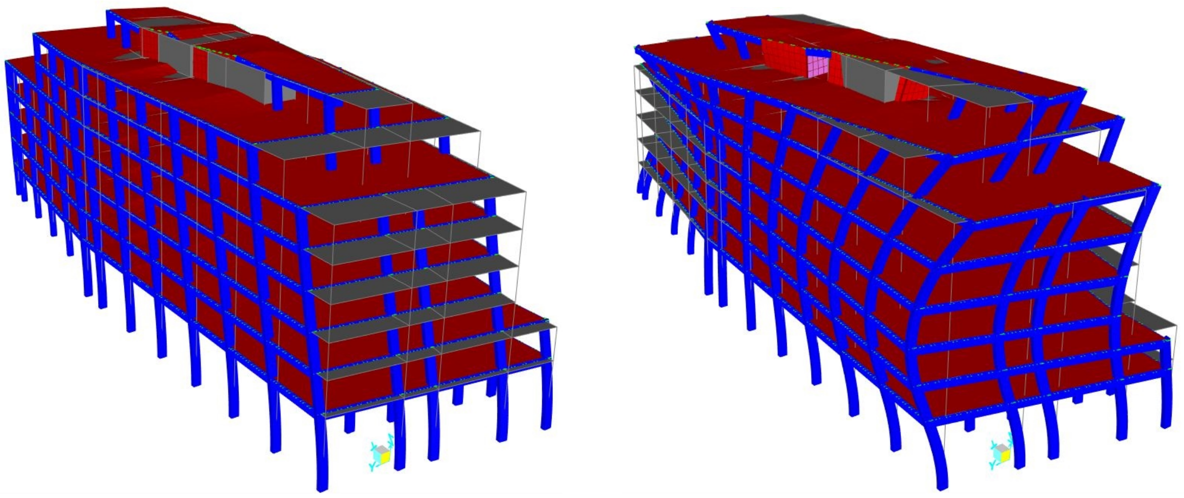

(c) Mode 3, scaled 400. $T_{n.3} = 1.286$ s. Translation in X.

(d) Mode 4, scaled 200. $T_{n.4} = 0.794$ s. Torsional mode.

Figure 5.1: The four first modes for the pinned reference case with the respective natural periods.

5.1.2 Rigid connection

For the rigid connection-case, the mode shapes can be seen graphically in Figure 5.2. The participation factors for each mode are presented in Table 5.2. Mode 1 is classified as translational in Y-direction and the second mode translational in X. The third mode is classified as torsional, while mode 4 is the second translational mode in Y. For this case, the cumulative participation ratio in each main direction exceeds 90% in mode 5, being a translational mode in X.

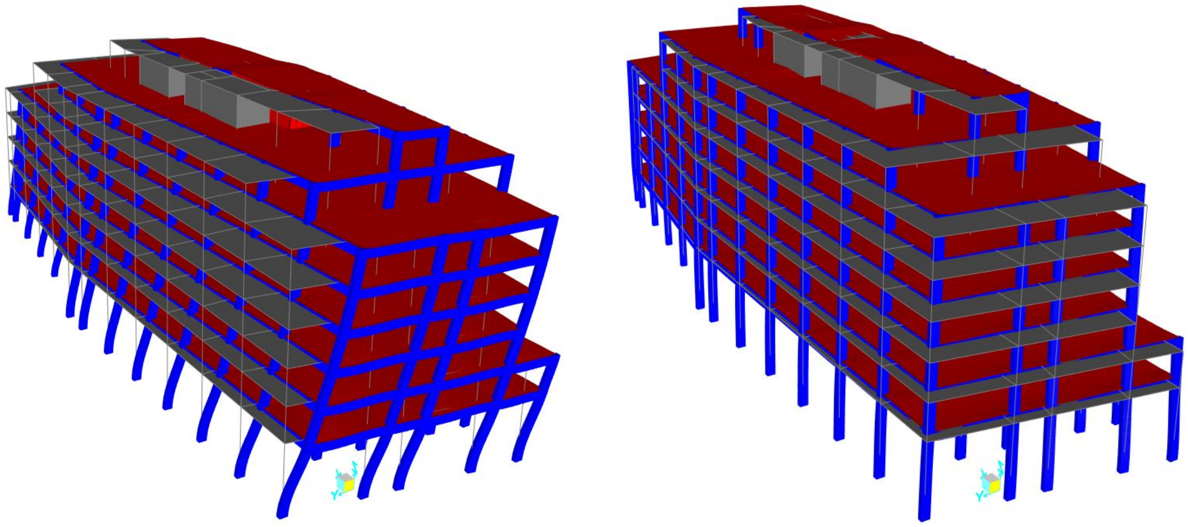

(a) Mode 1, scaled 400. $T_{n.1} = 1.184$ s. Translation in Y.

(b) Mode 2, scaled 400. $T_{n.2} = 1.065$ s. Translation in X.

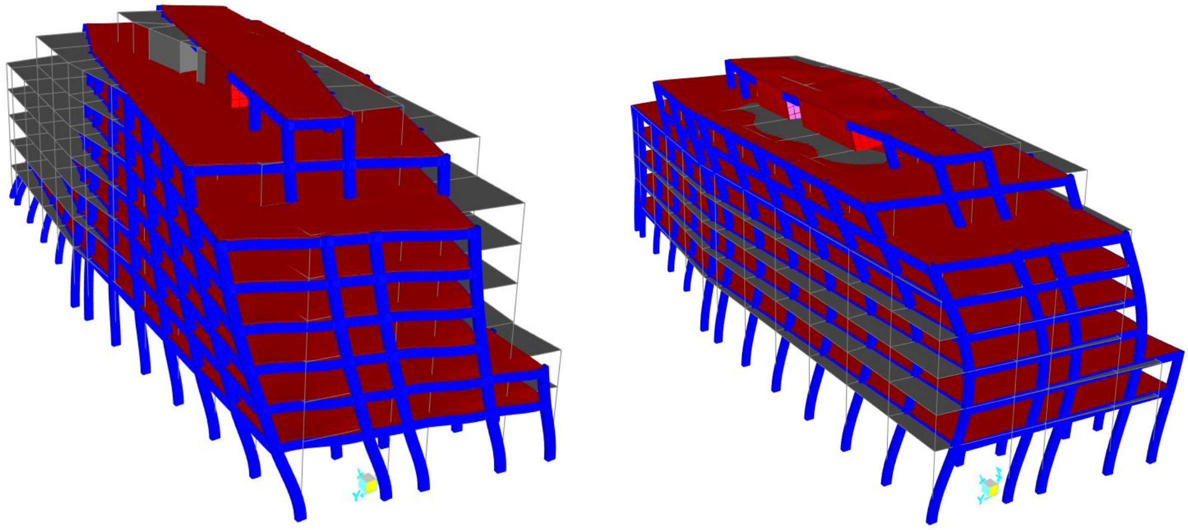

(c) Mode 3, scaled 400. $T_{n.3} = 1.003$ s. Torsional mode.

(d) Mode 4, scaled 200. $T_{n.4} = 0.349$ s. Translation in Y.

Figure 5.2: The four first modes for the rigid reference case with the respective natural periods.

Table 5.2: Overview of the modes giving mass participation ratio $\geq$ 90% for rigid case.

			Participation ratio					
Mode	**Type**	$\mathbf{T_n}$	$\mathbf{M_{Eff.Ux}}$	$\sum \mathbf{M_{Eff.Ux}}$	$\mathbf{M_{Eff.Uy}}$	$\sum \mathbf{M_{Eff.Ux}}$	$\mathbf{M_{Eff.Rz}}$	$\sum \mathbf{M_{Eff.Uz}}$
1	Trans Y	1.184	21.2%	*21.2%*	64.4%	*64.4%*	1.3%	*1.3%*
2	Trans X	1.065	59.1%	*80.3%*	23.1%	*87.5%*	4.3%	*5.6%*
3	Torsional	1.003	4.7%	*85.0%*	0.0%	*87.5%*	81.7%	*87.3%*
4	Trans Y	0.349	2.3%	*87.3%*	6.2%	*93.7%*	0.0%	*87.3%*
5	Trans X	0.318	7.0%	94.3%	2.0%	95.7%	0.0%	87.3%

5.1.3 Bolted connection

For the bolted connection-case, the mode shapes can be seen graphically in Figure 5.3. The participation factors for each mode are presented in Table 5.3. Mode 1 is classified as torsional, and the second mode as translational in Y. The third mode is translational in X, while mode 4 is the second torsional mode. For this case, the cumulative participation ratio in each main direction exceeds 90% in mode 6.

Table 5.3: Overview of the modes giving mass participation ratio $\geq$ 90% for bolted connection.

			Participation ratio					
Mode	**Type**	$\mathbf{T_n}$	$\mathbf{M_{Eff.Ux}}$	$\sum \mathbf{M_{Eff.Ux}}$	$\mathbf{M_{Eff.Uy}}$	$\sum \mathbf{M_{Eff.Ux}}$	$\mathbf{M_{Eff.Rz}}$	$\sum \mathbf{M_{Eff.Uz}}$
1	Torsional	2.407	0.1%	*0.1%*	3.0%	*3.0%*	72.1%	*72.1%*
2	Trans Y	1.401	0.0%	*0.1%*	75.5%	*78.5%*	2.3%	*74.4%*
3	Trans X	1.245	80.6%	*80.8%*	0.0%	*78.5%*	0.1%	*74.6%*
4	Torsional	0.734	0.1%	*80.9%*	0.0%	*78.5%*	14.6%	*89.1%*
5	Trans Y	0.409	2.9%	83.8%	10.1%	88.6%	0.0%	89.1%
6	Trans X	0.387	9.6%	93.4%	3.1%	91.7%	0.1%	89.3%

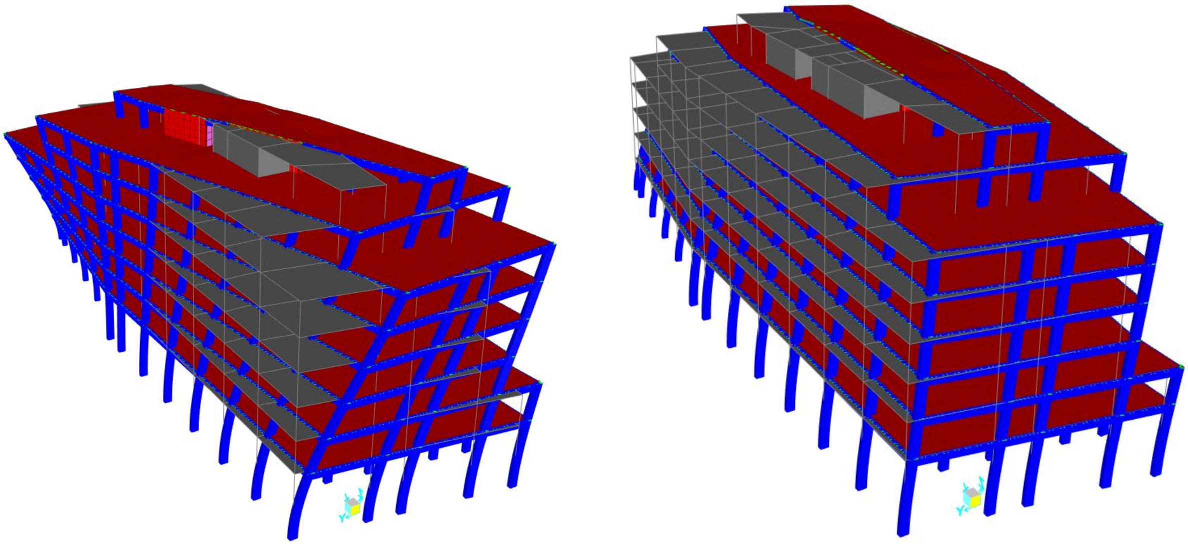

(a) Mode 1, scaled 400. $T_{n.1} = 2.407$ s. Torsional mode.

(b) Mode 2, scaled 400. $T_{n.2} = 1.401$ s. Translation in Y.

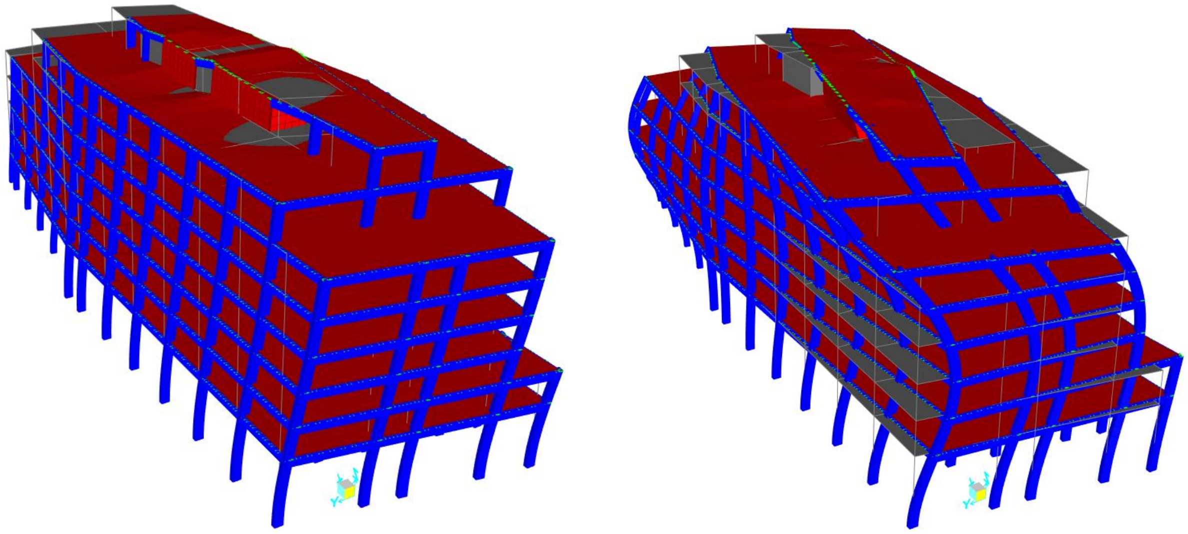

(c) Mode 3, scaled 400. $T_{n.3} = 1.245$ s. Translation in X.

(d) Mode 4, scaled 200. $T_{n.4} = 0.734$ s. Torsional mode.

Figure 5.3: The four first modes for the bolted case with the respective natural periods.

5.1.4 Top-and-seat steel angles connection

For the Top-and-seat steel angles connection-case, the mode shapes can be seen graphically in Figure 5.4. The participation factors for each mode are presented in Table 5.4. Mode 1 is classified as translational in Y-direction and the second mode translational in X. The third mode is classified as torsional, while mode 4 is the second translational mode in Y. For this case, the cumulative participation ratio in each main direction exceeds 90% in mode 6.

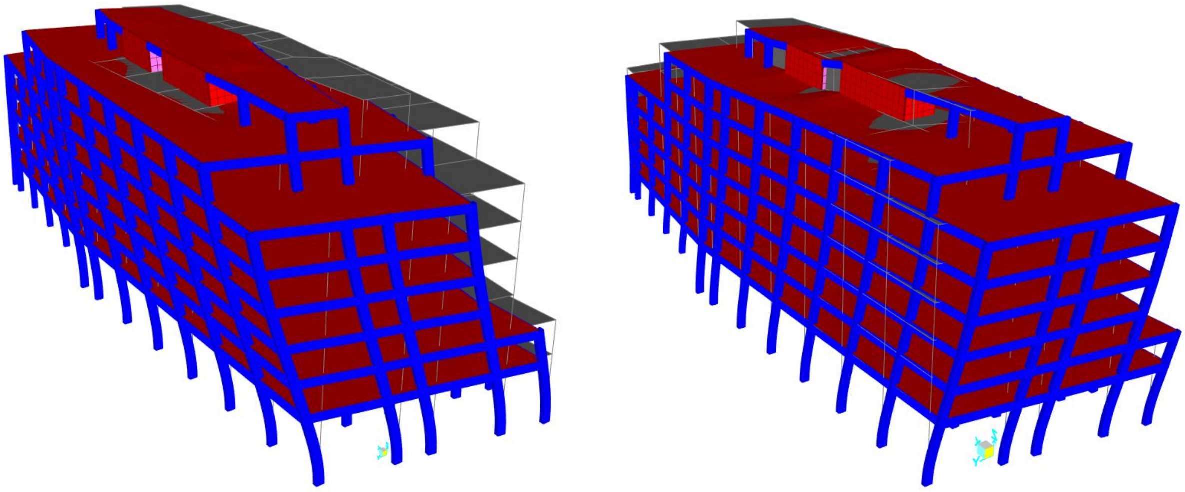

(a) Mode 1, scaled 400. $T_{n.1} = 1.303$ s. Translation in Y.

(b) Mode 2, scaled 400. $T_{n.2} = 1.126$ s. Translation in X.

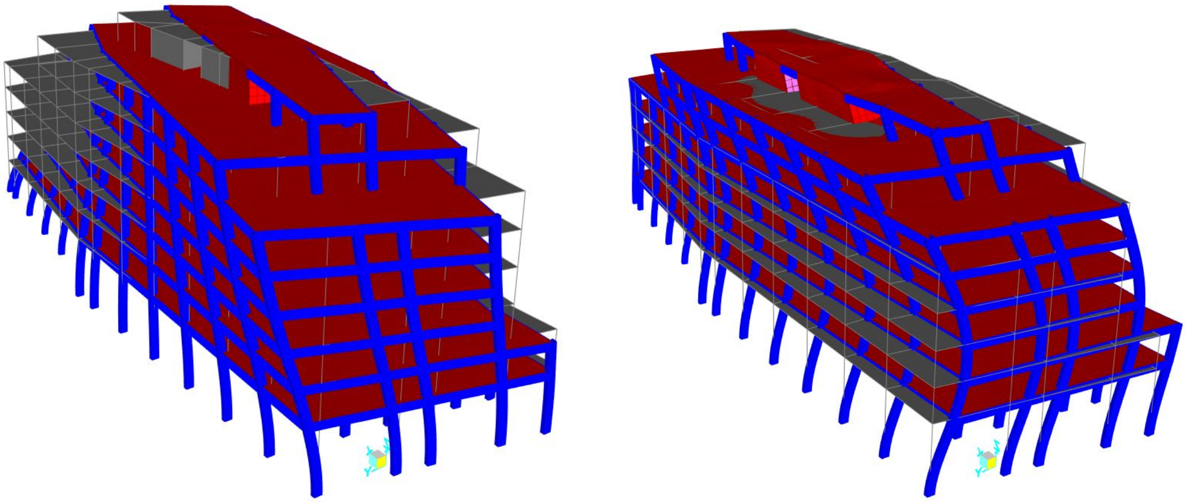

(c) Mode 3, scaled 400. $T_{n.3} = 1.121$ s. Torsional mode.

(d) Mode 4, scaled 200. $T_{n.4} = 0.394$ s. Translation in Y.

Figure 5.4: The four first modes for Top-and-seat steel angles with the respective natural periods.

Table 5.4: Overview of the modes giving mass participation ratio $\geq 90\%$ for Top-and-seat steel angles.

			Participation ratio					
Mode	**Type**	$\mathbf{T_n}$	$\mathbf{M_{Eff.Ux}}$	$\sum \mathbf{M_{Eff.Ux}}$	$\mathbf{M_{Eff.Uy}}$	$\sum \mathbf{M_{Eff.Ux}}$	$\mathbf{M_{Eff.Rz}}$	$\sum \mathbf{M_{Eff.Uz}}$
1	Trans Y	1.303	0.0%	*0.0%*	68.2%	*68.2%*	13.2%	*13.2%*
2	Trans X	1.126	81.8%	*81.9%*	0.2%	*68.4%*	2.2%	*15.4%*
3	Torsional	1.121	2.3%	*84.2%*	12.2%	*80.6%*	65.2%	*80.6%*
4	Trans Y	0.394	0.1%	*84.3%*	10.5%	*91.1%*	1.4%	*82.0%*
5	Torsional	0.344	0.1%	84.4%	1.2%	92.4%	9.4%	91.3%
6	Trans X	0.340	10.2%	94.6%	0.1%	92.5%	0.1%	91.4%

5.1.5 Epoxied-in steel rods connection

For the Epoxied-in steel rods connection-case, the mode shapes can be seen graphically in Figure 5.5. The participation factors for each mode are presented in Table 5.5. Mode 1 is classified as translational in Y-direction and the second mode translational in X. The third mode is classified as torsional, while mode 4 is the second translational mode in Y. For this case, the cumulative participation ratio in each main direction exceeds 90% in mode 6.

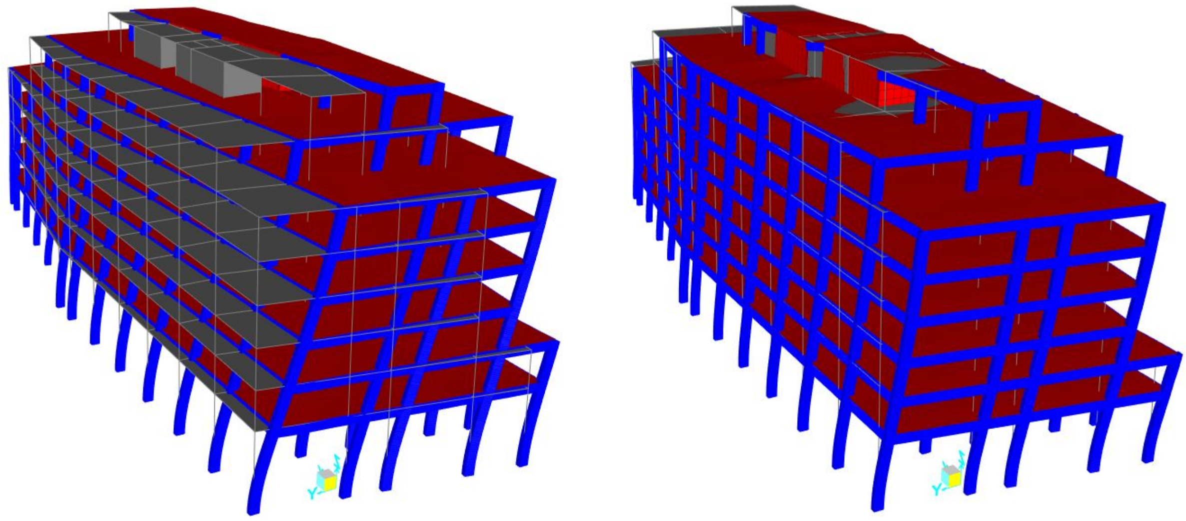

(a) Mode 1, scaled 400. $T_{n.1} = 1.283$ s. Translation in Y (Torsional).

(b) Mode 2, scaled 400. $T_{n.2} = 1.122$ s. Translation in X.

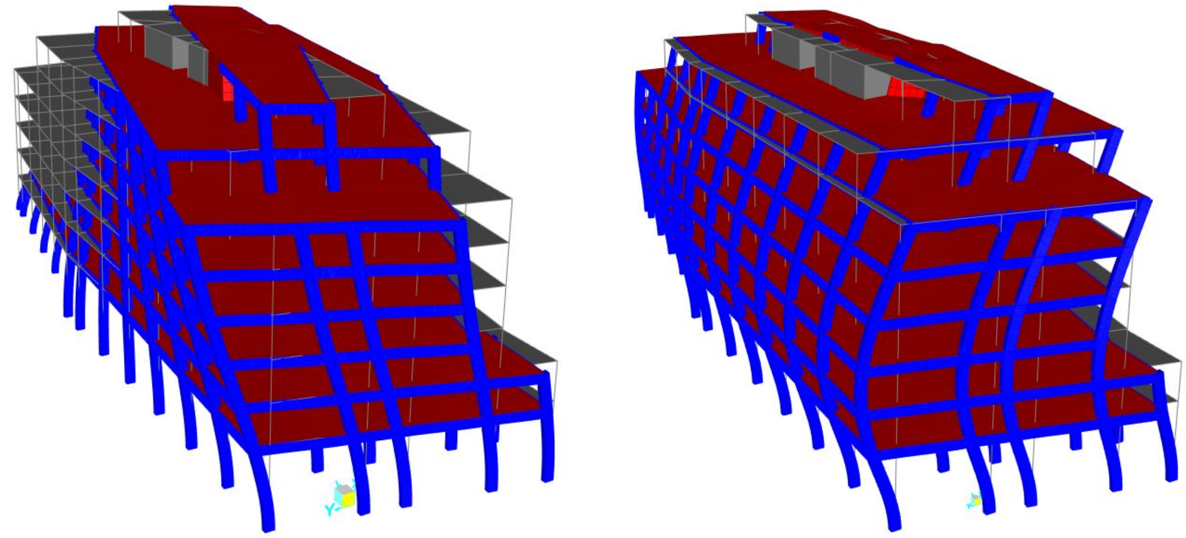

(c) Mode 3, scaled 400. $T_{n.3} = 1.110$ s. Torsional mode.

(d) Mode 4, scaled 200. $T_{n.4} = 0.391$ s. Translation in Y.

Figure 5.5: The four first modes for the Epoxied-in steel rods with the respective natural periods.

Table 5.5: Overview of the modes giving mass participation ratio $\geq$ 90% for Epoxied-in steel rods.

			Participation ratio					
Mode	**Type**	$\mathbf{T_n}$	$\mathbf{M_{Eff.Ux}}$	$\sum \mathbf{M_{Eff.Ux}}$	$\mathbf{M_{Eff.Uy}}$	$\sum \mathbf{M_{Eff.Ux}}$	$\mathbf{M_{Eff.Rz}}$	$\sum \mathbf{M_{Eff.Uz}}$
1	Trans Y	1.283	0.2%	*0.2%*	69.8%	*69.8%*	11.9%	*11.9%*
2	Trans X	1.122	83.8%	*83.9%*	0.0%	*69.8%*	0.6%	*12.5%*
3	Torsional	1.110	0.4%	*84.3%*	11.2%	*81.0%*	68.8%	*81.2%*
4	Trans Y	0.391	0.2%	*84.5%*	10.8%	*91.8%*	0.8%	*82.0%*
5	Torsional	0.340	0.4%	84.9%	0.7%	92.5%	9.3%	91.3%
6	Trans X	0.332	9.7%	94.6%	0.1%	92.6%	0.5%	91.7%

5.1.6 Inclined threaded rods and steel rings connection

For the Inclined threaded rods connection-case, the mode shapes can be seen graphically in Figure 5.6. The participation factors for each mode are presented in Table 5.6. Mode 1 is classified as translational in Y-direction and the second mode translational in X-direction. The third mode is classified as torsional, while mode 4 is the second translational mode in Y. For this case, the cumulative participation ratio in each main direction exceeds 90% in mode 5.

Table 5.6: Overview of the modes giving mass participation ratio $\geq$ 90% for Inclined threaded rods connection.

			Participation ratio					
Mode	**Type**	$\mathbf{T_n}$	$\mathbf{M_{Eff.Ux}}$	$\sum \mathbf{M_{Eff.Ux}}$	$\mathbf{M_{Eff.Uy}}$	$\sum \mathbf{M_{Eff.Ux}}$	$\mathbf{M_{Eff.Rz}}$	$\sum \mathbf{M_{Eff.Uz}}$
1	Trans Y	1.246	3.6%	*3.6%*	71.4%	*71.4%*	7.6%	*7.6%*
2	Trans X	1.120	80.7%	*84.3%*	3.0%	*74.4%*	0.7%	*8.3%*
3	Torsional	1.092	0.0%	*84.3%*	7.4%	*81.8%*	74.1%	*82.4%*
4	Trans Y	0.384	2.3%	*86.6%*	8.6%	*90.4%*	0.1%	*82.5%*
5	Trans X	0.339	7.6%	94.2%	2.5%	92.9%	0.4%	82.9%

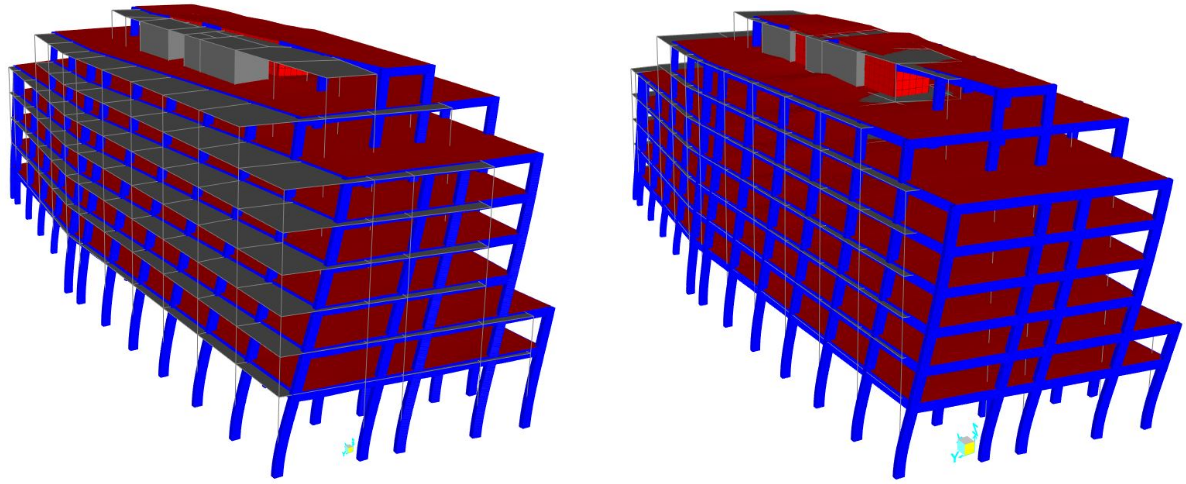

(a) Mode 1, scaled 400. $T_{n.1} = 1.246$ s. Translation in Y.

(b) Mode 2, scaled 400. $T_{n.2} = 1.120$ s. Translation in X.

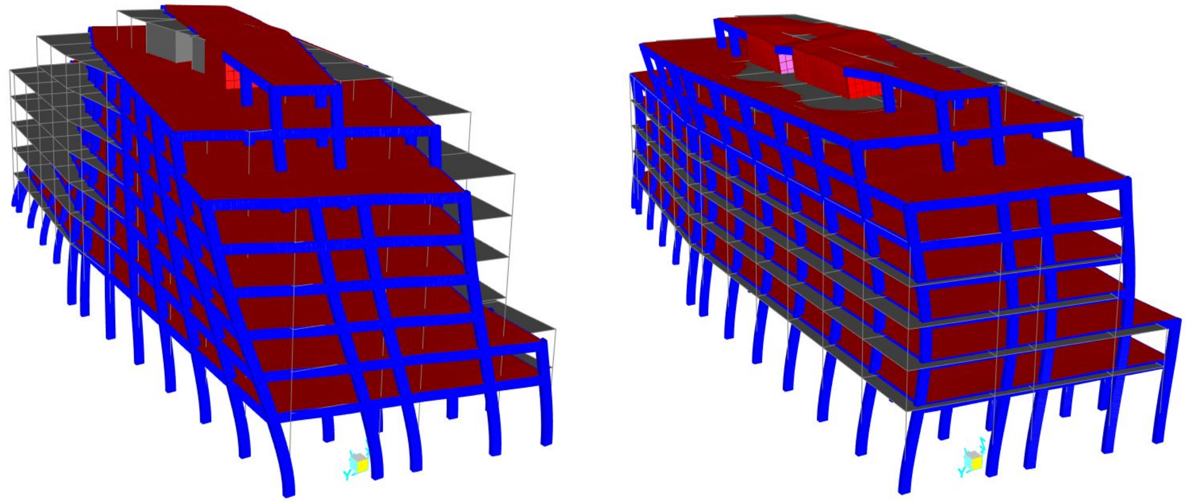

(c) Mode 3, scaled 400. $T_{n.3} = 1.092$ s. Torsional mode.

(d) Mode 4, scaled 200. $T_{n.4} = 0.384$ s. Translation in Y.

Figure 5.6: The four first modes for the Inclined threaded rods case with the respective natural periods.

5.2 Modal response spectrum analysis

In this section the results from the Modal Response Spectrum Analysis are presented. For each case, the story average absolute- (AD) and interstory drift (ID) in the two main global directions U1 (Global X) and U2 (Global Y) of is shown, along with a graphical view of the resultant absolute displacement. The scales used in the contour plot are adapted to each case, resulting in dark blue where the displacements are higher and magenta where the displacements are lower.

5.2.1 Pinned connecion

The results MRSA analysis for the pinned connection leads to the contour plots of the resultant displacements shown in Figure 5.7. The maximum AD is located in the top floor for both cases, with an average top floor displacement of 26.53 mm in global X for load case 1, and average top floor displacement of 29.19 mm in global Y for load case 2. Maximum ID is for both cases found in level 1.

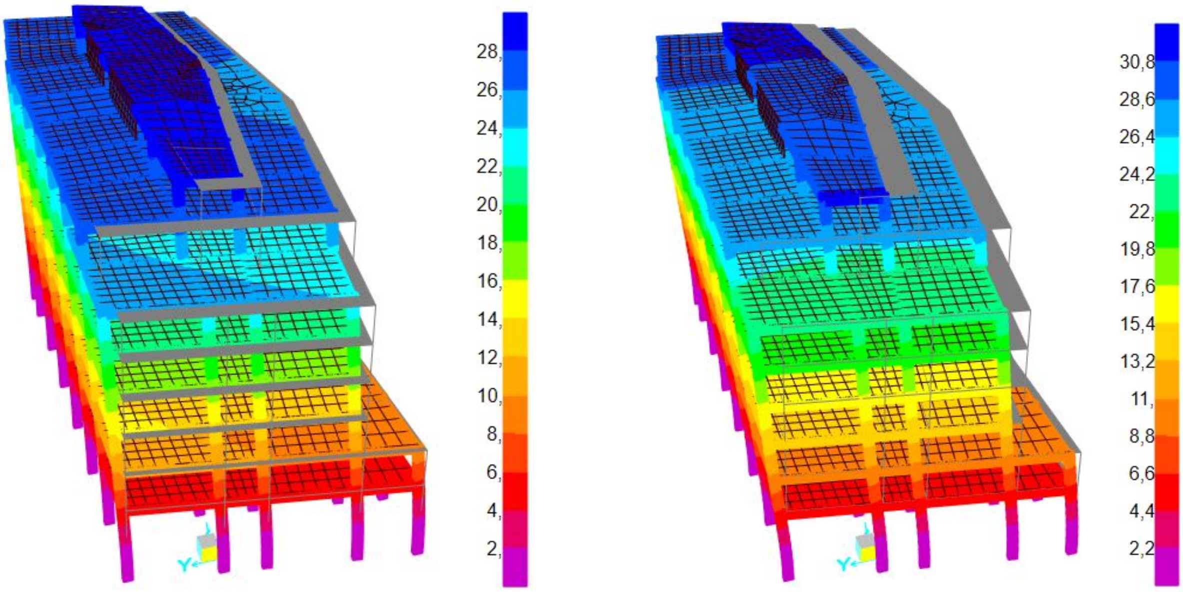

(a) Displacement resultant $E_{Edx} + 0.3E_{Edy}$.

(b) Displacement resultant $E_{Edy} + 0.3E_{Edx}$.

Figure 5.7: Displacement resultants pinned connections.

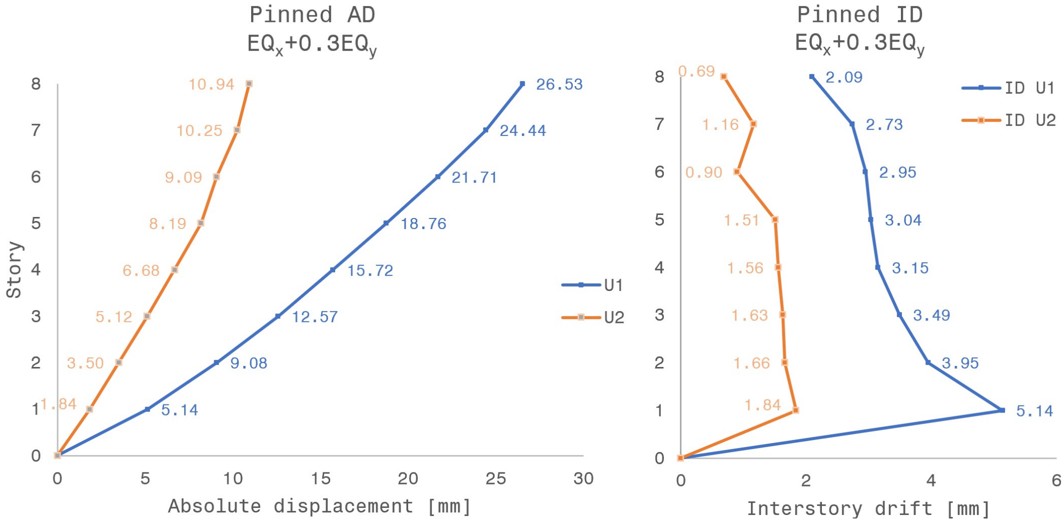

Figure 5.8: Pinned connections, average story AD and ID for $E_{Edx} + 0.3E_{Edy}$.

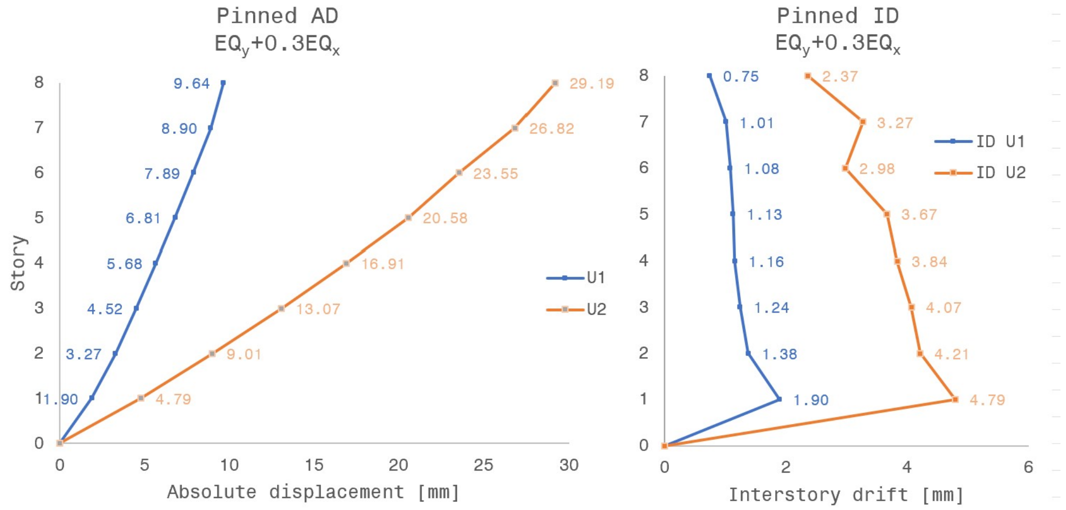

Figure 5.9: Pinned connections, average story AD and ID for $E_{Edy} + 0.3E_{Edx}$.

5.2.2 Rigid connection

The results MRSA analysis for the rigid connection leads to the contour plots of the resultant displacements shown in Figure 5.10. The maximum average AD is located in the top floor for both cases, with an average top floor displacement of 42.16 mm in global X for load case 1, and average top floor displacement of 42.43 mm in global Y for load case 2. Maximum ID is for both cases found in level 1. Figure 5.10b shows that AD varies from approximately 56 mm in the southern part to 40 mm in the northern part.

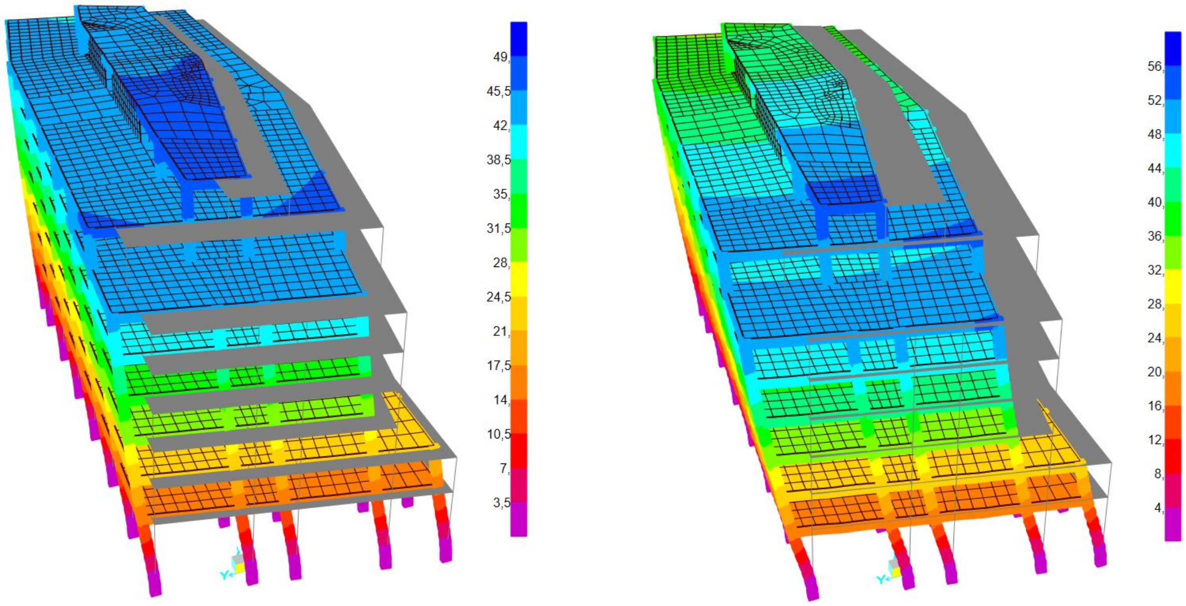

(a) Displacement resultant $E_{Edx} + 0.3E_{Edy}$.

(b) Displacement resultant $E_{Edy} + 0.3E_{Edx}$.

Figure 5.10: Displacement resultants rigid connections.

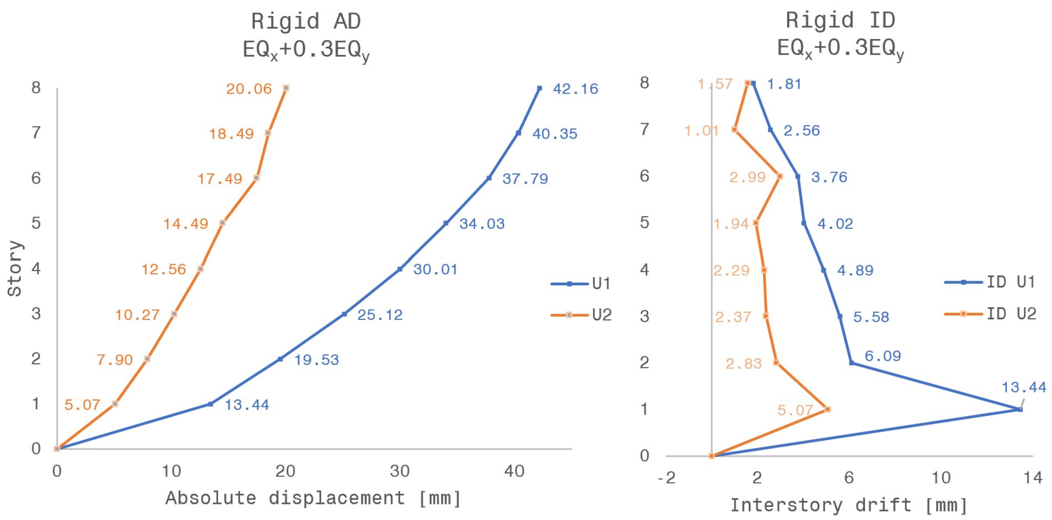

Figure 5.11: Rigid connections, average story AD and ID for $E_{Edx} + 0.3E_{Edy}$.

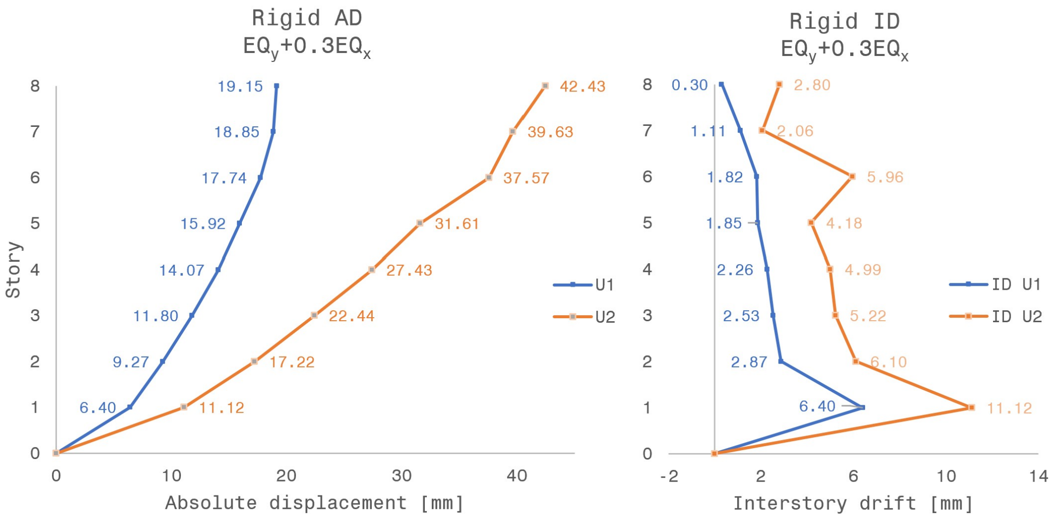

Figure 5.12: Rigid connections, average story AD and ID for $E_{Edy} + 0.3E_{Edx}$.

5.2.3 Bolted connection

The results MRSA analysis for the bolted connection leads to the contour plots of the resultant displacements shown in Figure 5.13. The maximum average AD is located in the top floor for both cases, with an average top floor displacement of 24.26 mm in global X for load case 1, and average top floor displacement of 24.49 mm in global Y for load case 2. Figure 5.13b shows that AD varies in the top floor story from approximately 30 mm in the part northern part to 22 mm in the southern part.

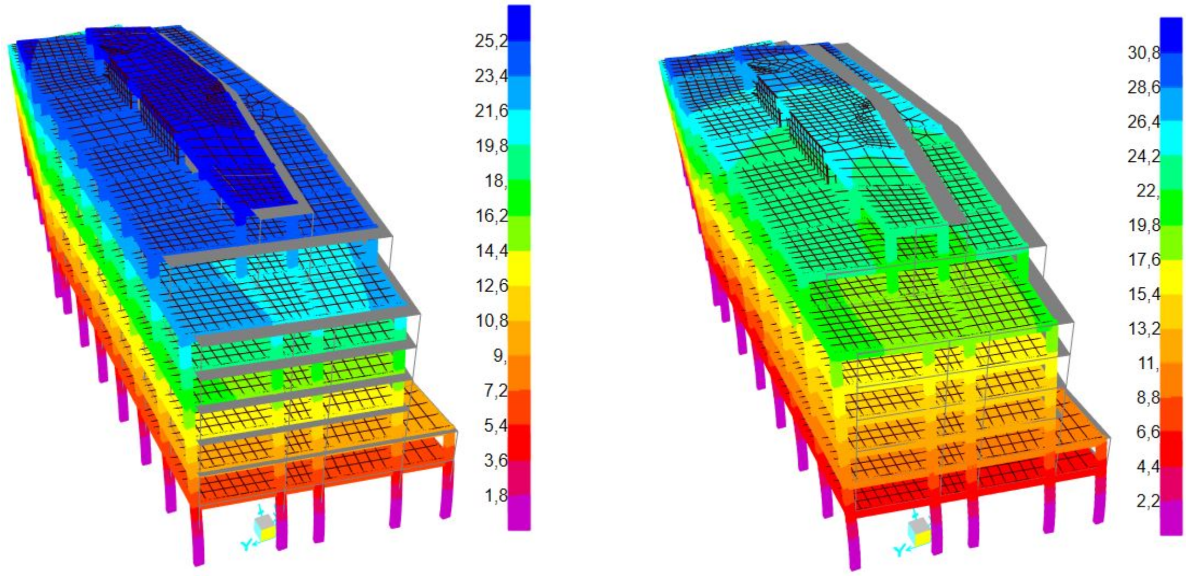

(a) Displacement resultant $E_{Edx} + 0.3E_{Edy}$.

(b) Displacement resultant $E_{Edy} + 0.3E_{Edx}$.

Figure 5.13: Displacement resultant bolted connections.

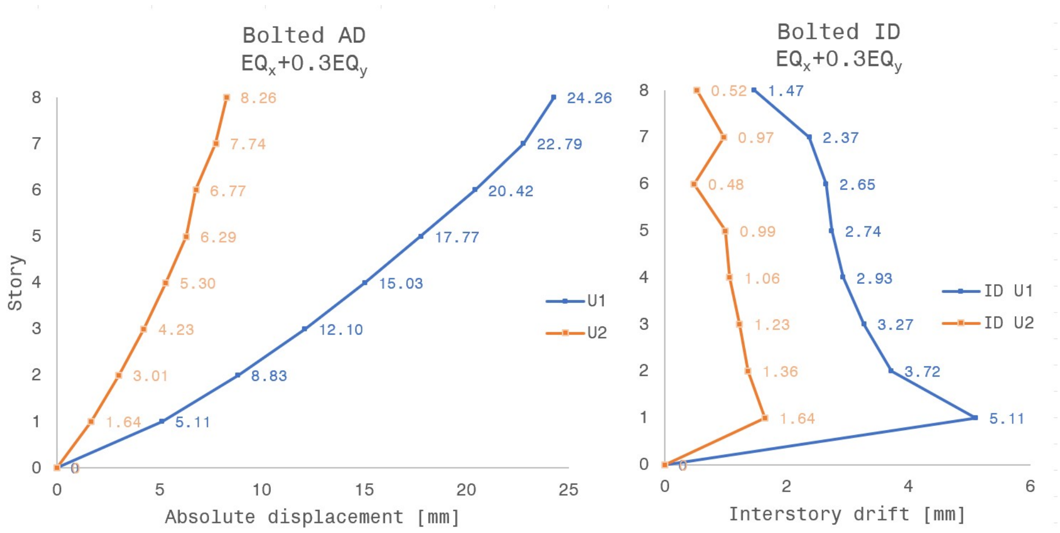

Figure 5.14: Bolted connections, average story AD and ID for $E_{Edx} + 0.3E_{Edy}$.

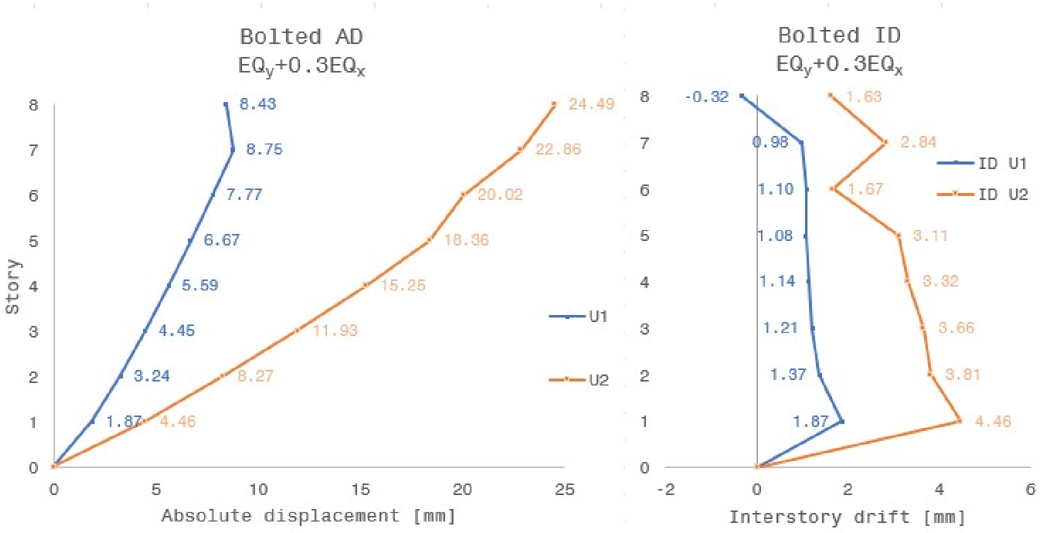

Figure 5.15: Bolted connections, average story AD and ID for $E_{Edy} + 0.3E_{Edx}$.

5.2.4 Top-and-seat steel angles connection

The results MRSA analysis for the Top-and-seat steel angles connection leads to the contour plots of the resultant displacements shown in Figure 5.16. The maximum average AD is located in the top floor for both cases, with an average top floor displacement of 22.42 mm in global X for load case 1, and average top floor displacement of 21.59 mm in global Y for load case 2. Figure 5.16b shows that AD varies in the top floor story from approximately 30 mm in the southern part to 22 mm in the northern part.

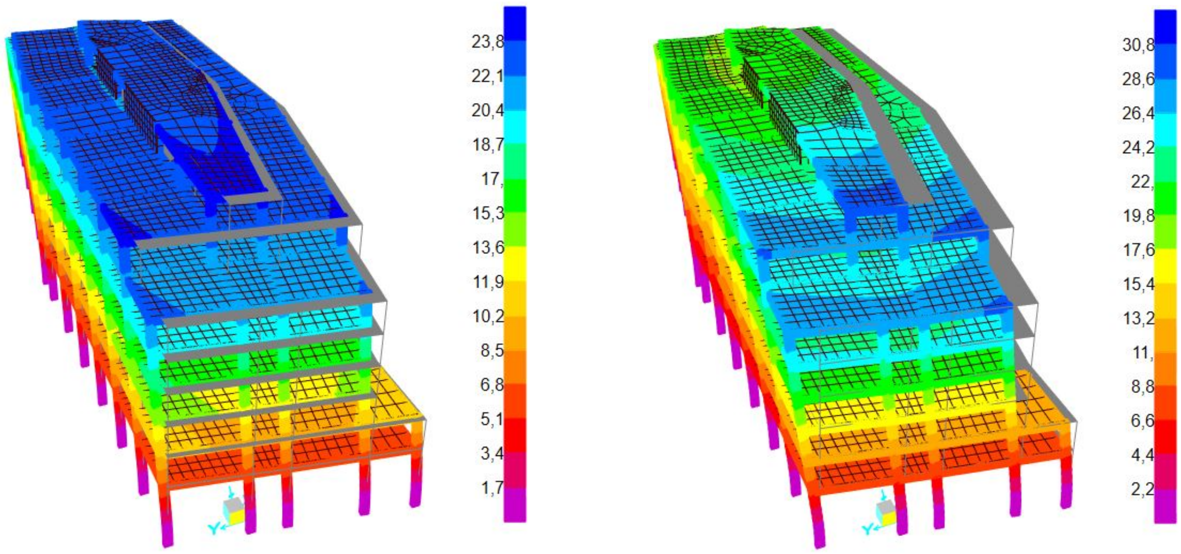

(a) Displacement resultant $E_{Edx} + 0.3E_{Edy}$. **(b)** Displacement resultant $E_{Edy} + 0.3E_{Edx}$.

Figure 5.16: Displacement resultants for Top-and-seat steel angles connections.

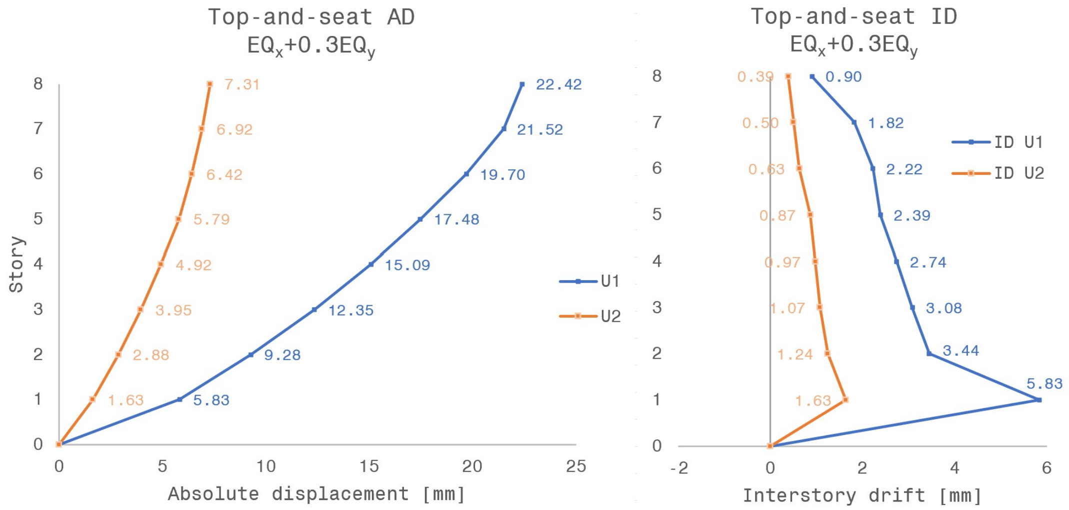

Figure 5.17: Top-and-seat steel angles connections, average story AD and ID for $E_{Edx} + 0.3E_{Edy}$.

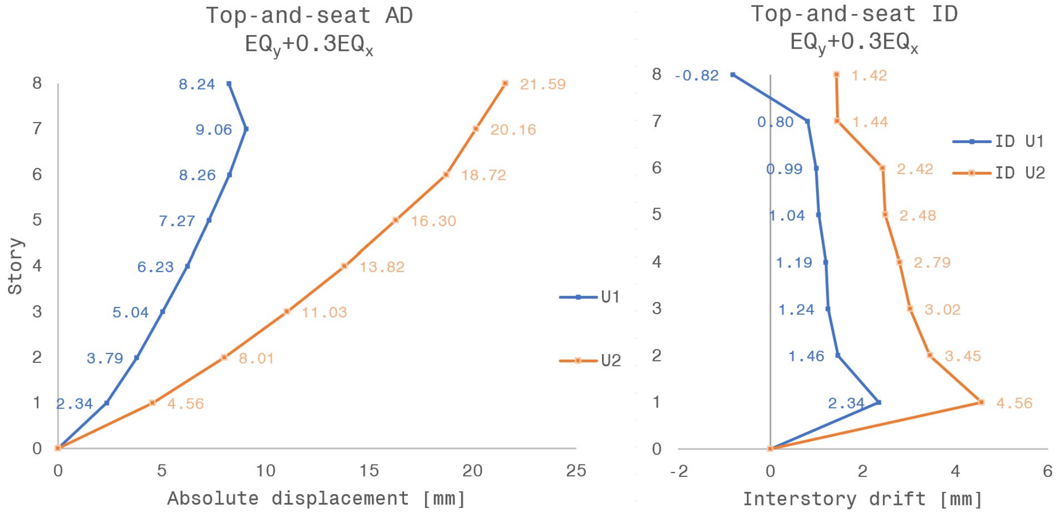

Figure 5.18: Top-and-seat steel angles connections, average story AD and ID for $E_{Edy} + 0.3E_{Edx}$.

5.2.5 Epoxied-in steel rods connection

The results MRSA analysis for the Epoxied-in connection leads to the contour plots of the resultant displacements shown in Figure 5.19. The maximum average AD is located in the top floor for both cases, with an average top floor displacement of 14.10 mm in global X for load case 1, and average top floor displacement of 15.82 mm in global Y for load case 2. Figure 5.19b shows that AD varies in the top floor from approximately 22 mm in the southern part to 14 mm in the northern part.

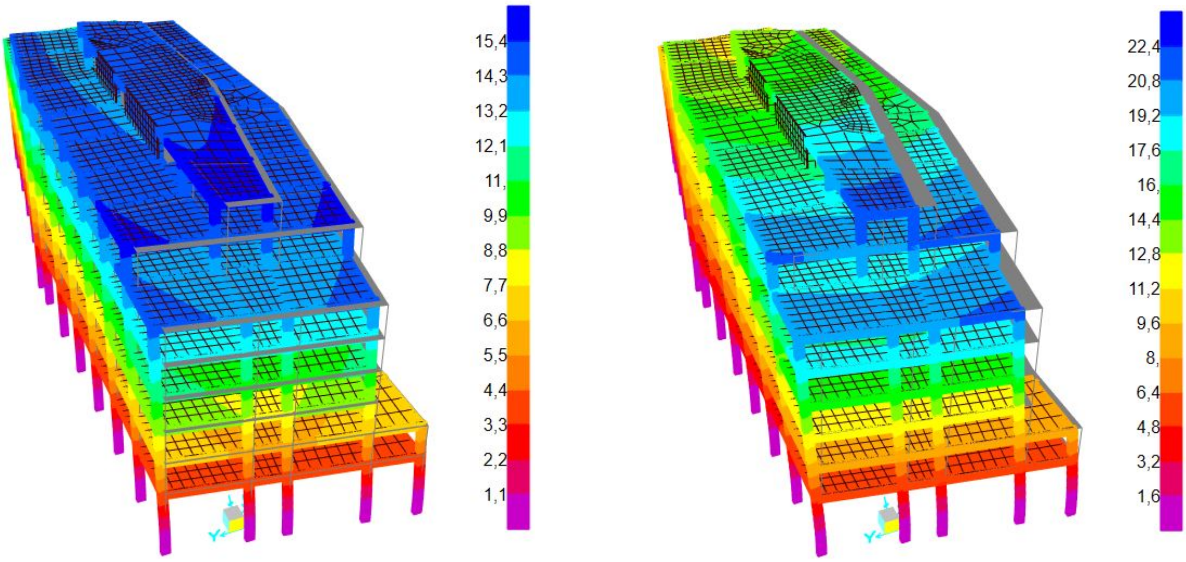

(a) Displacement resultant $E_{Edx} + 0.3E_{Edy}$.

(b) Displacement resultant $E_{Edy} + 0.3E_{Edx}$.

Figure 5.19: Displacement resultants for Epoxied-in connections.

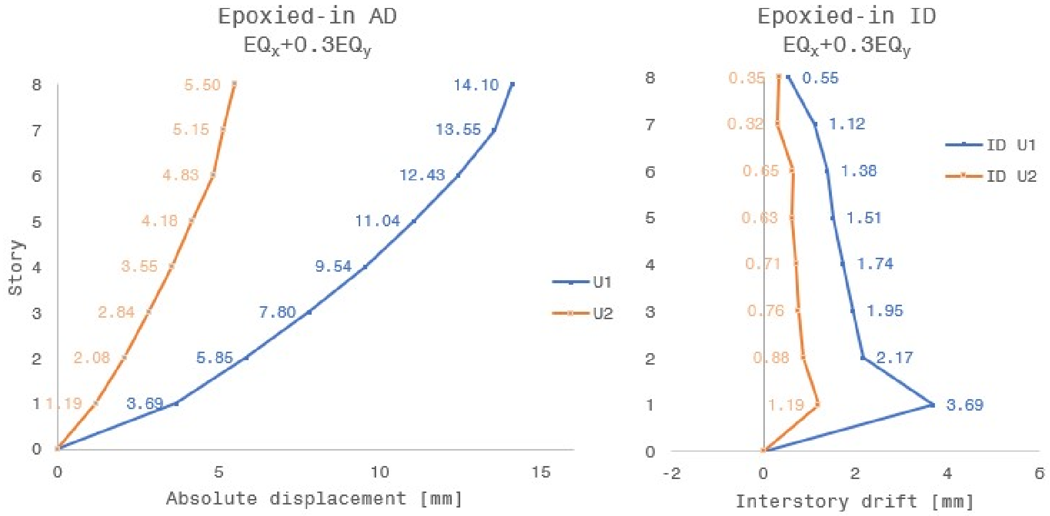

Figure 5.20: Epoxied-in connections, average story AD and ID for $E_{Edx} + 0.3E_{Edy}$.

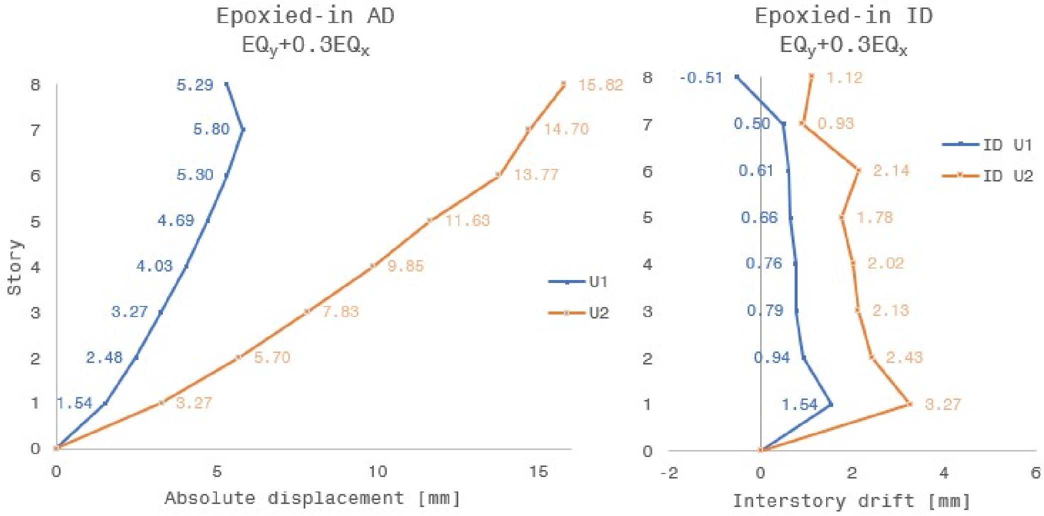

Figure 5.21: Epoxied-in connections, average story AD and ID for $E_{Edy} + 0.3E_{Edx}$.

5.2.6 Inclined threaded rods and steel rings connection

The results MRSA analysis for the Inclined threaded rods connection leads to the contour plots of the resultant displacements shown in Figure 5.22. The maximum average AD is located in the top floor for both cases, with an average top floor displacement of 22.57 mm in global X for load case 1, and average top floor displacement of 22.68 mm in global Y for load case 2. Figure 5.22b shows that AD varies in the top floor story from approximately 30 mm in the southern part to 20 mm in the northern part.

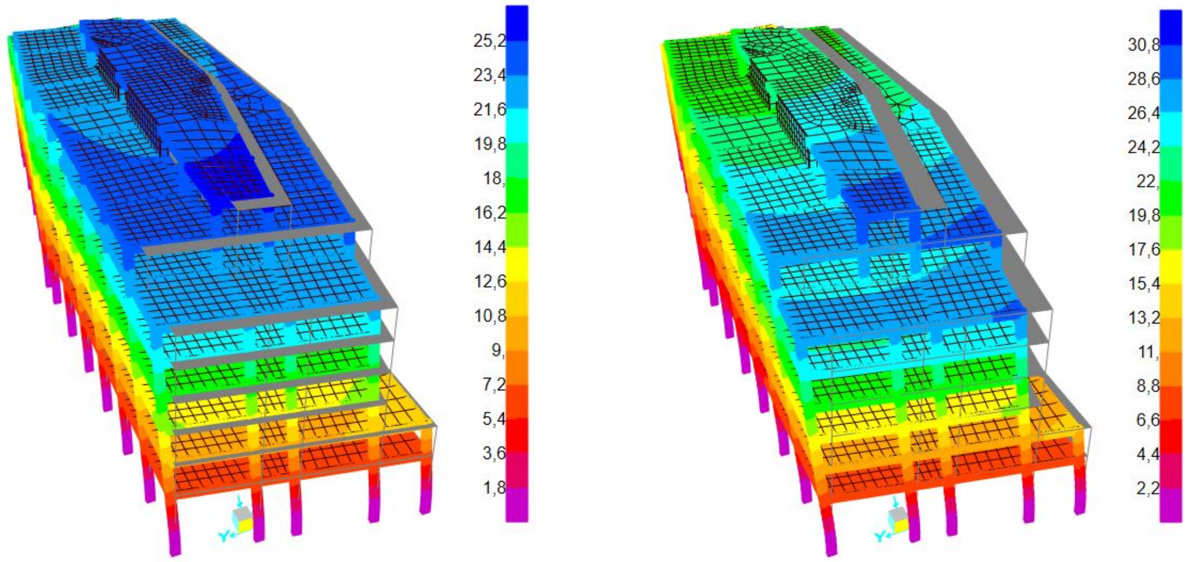

(a) Displacement resultant $E_{Edx} + 0.3E_{Edy}$.

(b) Displacement resultant $E_{Edy} + 0.3E_{Edx}$.

Figure 5.22: Displacement resultants for Inclined threaded rods connections.

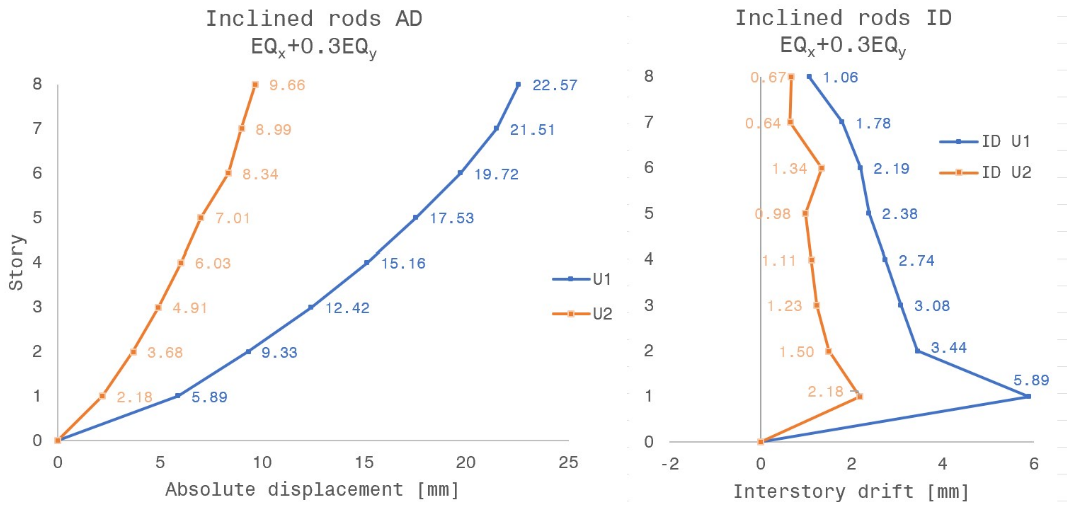

Figure 5.23: Inclined threaded rods connections, average story AD and ID for $E_{Edx} + 0.3E_{Edy}$.

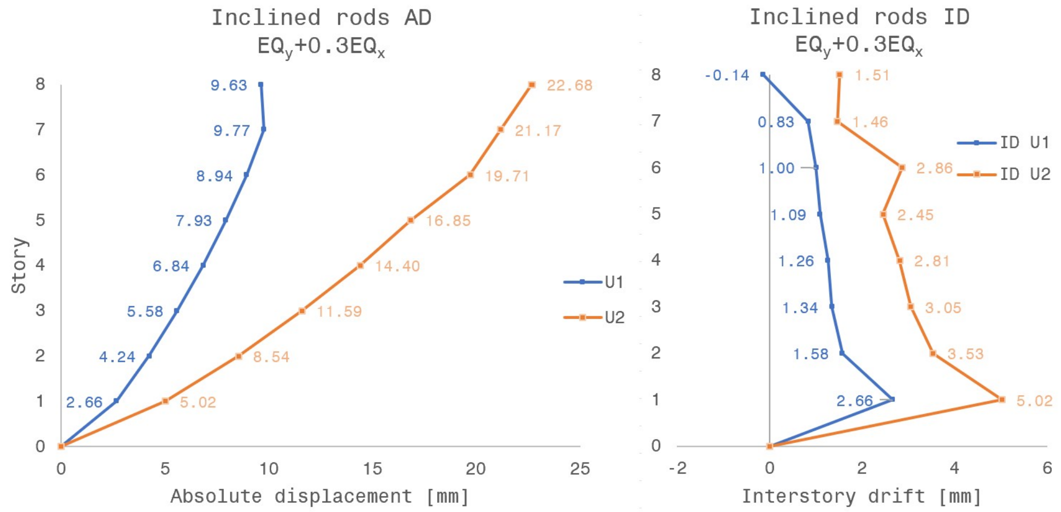

Figure 5.24: Inclined threaded rods connections, average story AD and ID for $E_{Edy} + 0.3E_{Edx}$.

5.2.7 Interstory drift

The interstory drift for each case is compared to the limits presented in Table 4.16. For all presented cases, the critical ID is found in story 1, but for no cases the limits are exceeded. The most critical displacements are for the Rigid connection with a utilization ratio:

$$\frac{ID_{max}}{Limit_{q=1.5,\,story\,1}} = \frac{13.44}{128.25} = 10.5\% \tag{5.1}$$

6. Discussion

This chapter is dedicated to discussing the results presented in chapter 5, where the results from the modal analysis and the seismic performance are evaluated for each connection. The next part contains an evaluation of each connection regarding seismic performance, ease of construction, ease of disassembly, reuse potential of the beam, column, and connecting elements, and the aesthetics of the joint. An overview of the discussed parameters is given, leading to a comparison of all connections. The comparison is the base for discussing the optimization process for seismic design of moment-resisting timber joints when designing for reuse.

6.1 Modal Analysis

This section discusses the results obtained in the modal analysis, highlights the differences, and discusses the main reasons behind the differences. First, a general discussion about the dynamic consequences of the building's structural build-up is necessary by using the results from the two reference cases, (1) pinned and (2) rigid connected beams.

6.1.1 Structural shape

The reference building is non-symmetric in plan and irregular in elevation. In plan, the non-symmetry is mainly due to the CLT core placed in the middle of the building not being symmetrically placed, and the angle differences in the global direction of the beams. In elevation, the irregularity is due to the story height of the lowest floor causing a soft story in the left part of the building when viewed in XZ-plane as in Figure 4.4a.

For the case with pinned connected beams, the location of a centrally placed stiff CLT core is unfavorable as these are the only contribution to the lateral stiffness of the building. This leads to large parts of elements providing lateral stiffness having a low radius of gyration R compared to the masses distributed over the whole plan, referred to as inertia masses in Section 3.1.5. This results in small angular stiffness components $k_{x,\theta}, k_{y,\theta}$, and k_θ in Eq. (3.31) compared to the inertia forces, and the torsional mode will be present at a lower frequency mode. For the pinned and bolted case, a modal participation factor of 90% is reached for the main directions at mode 6 with two torsional modes present already at mode 4.

The effect of increasing the rotational stiffness of beam-to-column connections is clearly shown by comparing the results for pinned connected beams in Table 5.1 with the case of rigid connected beams in Table 5.2. The results imply that higher rotational stiffness for the beam-to-column connections will shift the torsional mode to a higher frequency mode. Another important aspect of this shift is that the number of torsional modes contributing when modal participation ratios exceed 90% for the main directions is reduced to only one. This is beneficial as it removes the uncertainties and effects of torsional modes and leads to a more favorable behavior (Flores et al., 2017). Boti et al. (2018) introduce the possibility of including post-yield behavior and energy dissipation in the system when torsional modes are limited. Post-yield behavior of connections can be problematic for rigid, brittle connections, and only elastic structural behavior should be considered. This is because rigid connections attract significant more forces/energy than pinned connections, and if the connection than fails, the behavior of the structural system will change dramatically.

The irregularity in elevation is mainly caused by differences in the lowest floor, where two different column heights support the structure. As seen in Figure 4.4a and Figure 4.4b, the southern part has a floor height of 7695 mm, while the northern part of the building is 4980 mm. Therefore, it was in the early phase of the thesis decided to increase the dimensions of the columns in the left part. Optimizing column dimensions in upper levels may lead to reduced column dimensions and less material used. If the number of stories in the building were to be increased, the column dimensions must be carefully revised to exclude counterproductive effects. In addition to this, the top floor is contracted significantly from floors below. This leads to a lower mass in the top floor and consequently lower dynamic effects, as typically seen from the absolute- and interstory drift results from Section 5.2 MRSA.

6.1.2 Evaluation of modal results

Overall, the periods of the building for all cases are higher than the simplified fundamental period calculation proposed by EC8 4.3.3.2.2(3), as seen in Eq. (3.87). Using the height of the building $H = 34.295$ m and $C_t = 0.05$, the fundamental mode T_1 can be found:

$$T_1 = 0.05 \cdot (34.295)^{3/4} = 0.71\,\mathrm{s} \tag{6.1}$$

Based on the assumption that the model is valid, this shows the weakness of the fundamental period calculation when the building is either long or vulnerable to torsional effects due to irregularity in plan or elevation (Hussein et al., 2020). This can also be caused by the fact that CLT buildings tend to have higher natural periods than considered through the factor C_t (Polastri and Pozza, 2016).

The modes where torsional modes are present at a lower frequency mode differ more from the simplified method. The first mode periods for the pinned and bolted case are higher than the remaining cases, which, based on structural dynamics, show that the mass to stiffness ratio is higher than the remaining cases. These results are as expected as the numerical model is designed so that stiffness of the connections affect the structural behavior.

6.1.3 Connection to foundation

The connection to the foundation is for both the GLT columns and the CLT panels assumed to be rigid, meaning that displacements and rotations are restricted in all directions. From a review of different timber connections by Rebouças et al. (2022), the overall performance of a timber frame was significantly influenced by uplift and rotation at the base. Sandoli et al. (2021) present the traditional connections used for CLT panels as Hold-down (HDB)- and angle-brackets (AB). The HDB restrict the uplift of panels causing tensile forces, while AB are important for restricting shear forces and horizontal sliding.

For the rigid connection-case in Section 5.1.2, the change from rigid to pinned connections of CLT panels to the foundation only showed a negligible increase in the natural periods of the building. Using hinges for columns to foundation increased, on the other hand, the natural period by approximately 30%, from 1.18 s to 1.54 s. Using rigid connection is too advantageous when considering horizontal design load but was implemented to enhance the effect of changing the rotational stiffness of Beam-to-column connections.

6.2 Response spectrum analysis

For modal combination, the CQC method is chosen. This is done to include correlation for modes with approximately equal frequencies. The effect of this is especially relevant when torsional modes and directional modes have approximately the same frequencies.

The importance class of the building is chosen as seismic class IIIa, and from Table 3.5 this may be over-conservative for the reference building, leading to a higher design ground acceleration than necessary. The main reason behind choosing a higher seismic class is the unknown use of the lowest floor.

6.2.1 Structural behaviour

The deformed shapes are displayed only for the load combinations given in Section 4.4, where the average joint displacements in the two global directions for each floor are used to plot AD and ID. For cases where the contour plots show a significant variation in displacement internally in a floor, the displacement should be revised more in detail. Generally, this is not the case when E_{Edx} is the dominant load. For the case where E_{Edy} is dominant, the torsional effects are more prominent.

By comparing the results from the MRSA for all connections with load case 2, the tendency is that the connections that offer lower rotational stiffness create a case where the first torsional mode, with a higher mass participation ratio, is located where the pseudo-acceleration is low. By inserting the first torsional mode and its period for all cases in the design response spectra, as seen in Figure 6.1, the respective design pseudo-accelerations can be compared.

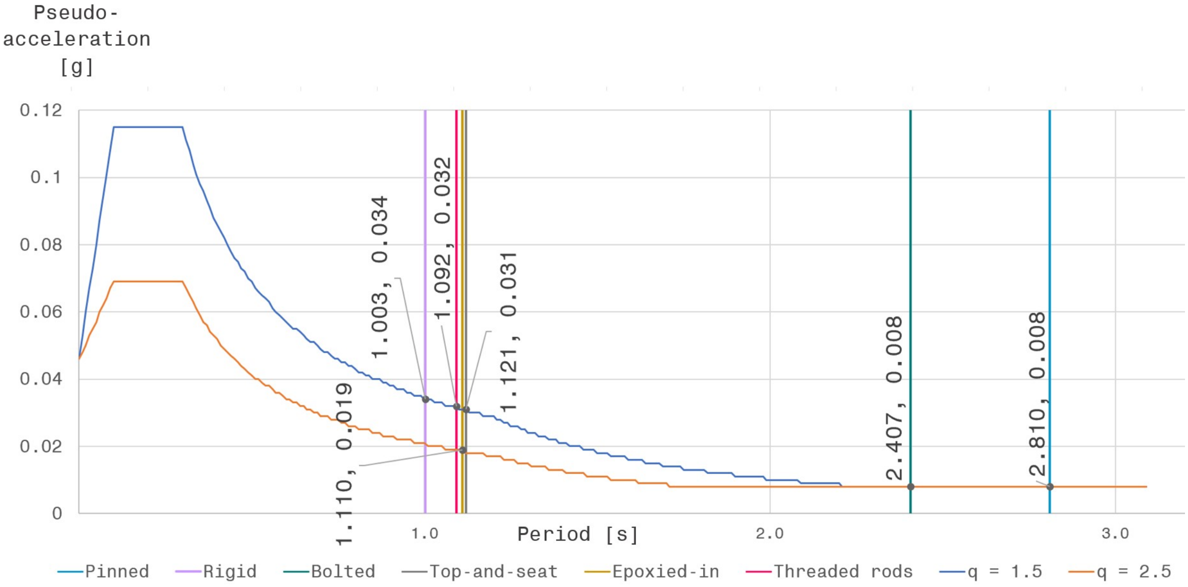

Figure 6.1: First torsional modes with the respective period and design pseudo-acceleration. Labels are *Period, PSA*.

The first observation is that the pseudo-acceleration (PSA) for the bolted and pinned case is equal. This is expected as the bolted connection per EC3 is categorized as a pinned connection. For the rigid case, PSA is 325% higher caused by this mode and its period being closer to the acceleration-based calculation area of a normalized design spectrum seen in Figure 3.13.

The Epoxied-in steel rods connection (Ep-in) is governed by the fact that the ductility of this connection is high. The effect becomes clear both when comparing the first torsional mode to the Top-and-seat steel angles connection (TaS), which has a higher period but yet a higher PSA, and when comparing the absolute drift. For Ep-in, the average top story AD resultant for load cases 1 and 2 are 15.3 mm and 16.68 mm, respectively, while for the remaining cases, the maxima are typically 24-26 mm.

Both TaS and Inclined threaded-rods connection (InTR) have the first torsional mode within the same period range. By comparing the contour plots from the MRSA for these two cases in Figure 6.2, it can be seen that also the 2nd torsional mode provides significant effects and displacements for TaS. This statement is based on the displacement range of the contour plots being approximately equal, even though the 1st torsional mode of TaS only has a Mass Participation Ratio about global Z ($M_{Eff.Rz}$) of 65.2%, compared to 81.2% for InTR. The effect of lower cumulative $M_{Eff.Rz}$ for InTR is also shown as the *change* in displacement resultant in level 6 is higher for TaS than for InTR, meaning that the displacements are more constant internally in each floor.

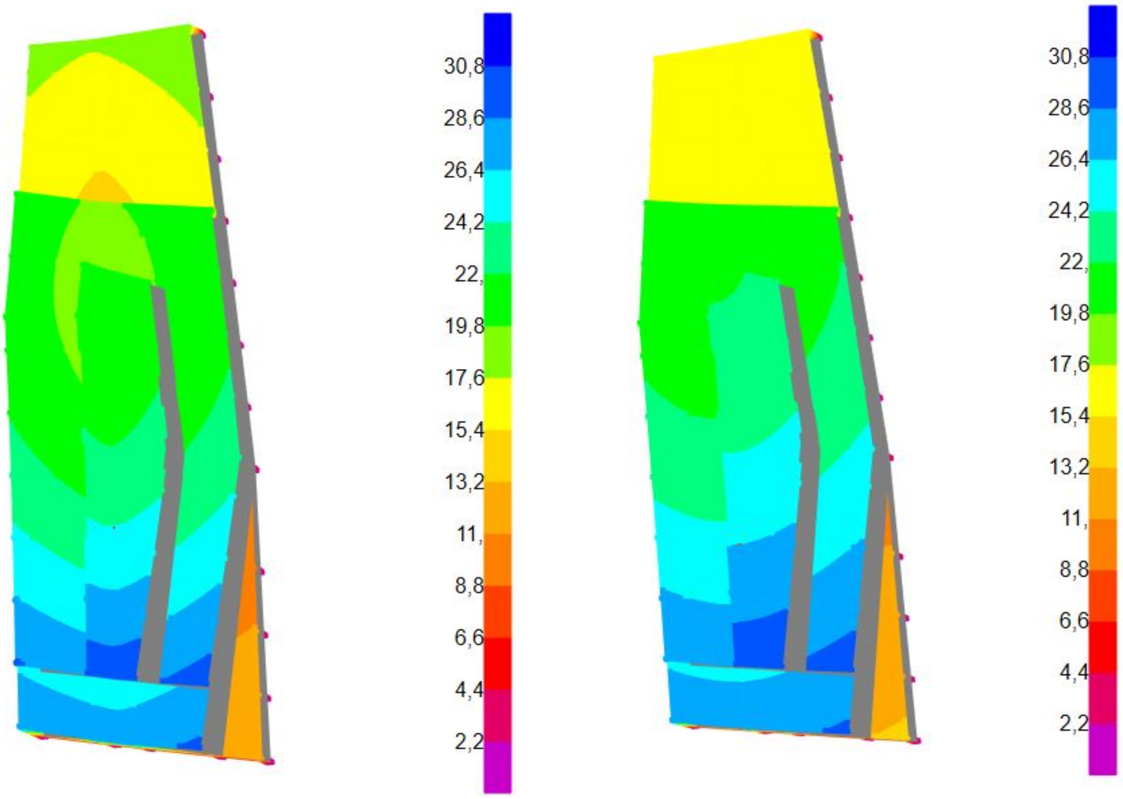

(a) Top-and-seat steel angles (TaS). **(b)** Inclined threaded rods with steel rings (InTR).

Figure 6.2: Top view of contour plot of displacement resultants for $E_{Edy} + 0.3E_{Edx}$.

Table 6.1: 1^{st} torsional modes, mass participation ratio about global Z (MPR_{Rz}) and the corresponding PSA from the respective design spectra.

Connection	1^{st} torsional mode	$M_{Eff.Rz}$	PSA [g]
Pinned	Mode 1 2.994 s	70.4%	0.008
Rigid	Mode 3 1.003 s	81.7%	0.034
Bolted	Mode 1 2.407 s	72.1%	0.008
Top-and-seat steel angles	Mode 3 1.121 s	65.2%	0.031
Epoxied-in steel rods	Mode 3 1.110 s	81.2%	0.019
Inclined threaded rods with steel rings	Mode 3 1.092 s	74.1%	0.032

Table 6.2: 2^{nd} torsional modes, mass participation ratio about global Z (MPR_{Rz}) and the corresponding PSA from the respective design spectra.

Connection	2^{nd} torsional mode	$M_{Eff.Rz}$	PSA [g]
Pinned	Mode 4 0.845 s	17.5%	0.041
Rigid	No 2nd torsional mode before cumulative sum in Ux & Uy exceeds 90%		
Bolted	Mode 4 0.734 s	14.6%	0.047
Top-and-seat steel angles	Mode 5 0.344 s	9.4%	0.101
Epoxied-in steel rods	Mode 5 0.340 s	9.3%	0.061
Inclined threaded rods with steel rings	No 2nd torsional mode before cumulative sum in Ux & Uy exceeds 90%		

In this thesis, the type 2 response spectrum is used, following recommendations from EC8-1 NA.3.2.2.2. If the building was located in an area with significantly higher intensity of earthquakes and surface wave magnitude $M_s \geq 5.5$, Pitilakis et al. (2015)

recommend using Type 1 response spectrum. Type 1 spectrum includes higher period modes, while type 2 has larger normalized spectral amplitudes at short periods. This would lead to the first torsional modes contributing more to the displacements, based on the comparison seen in Figure 6.3. This implies that buildings located in low seismicity areas are more vulnerable to ground acceleration if the fundamental period is lower. This is typically the case for buildings with fewer stories than the reference building.

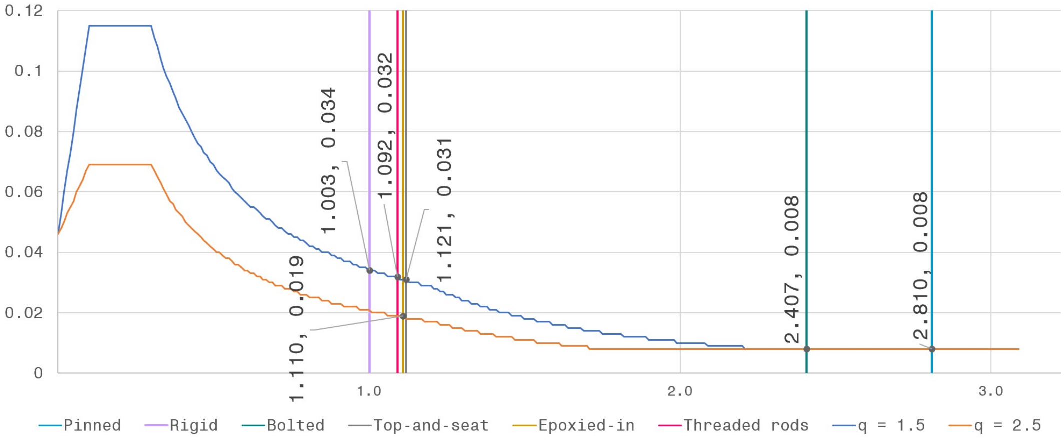

(a) First torsional modes plotted in type 2 spectrum (Low seismicity area).

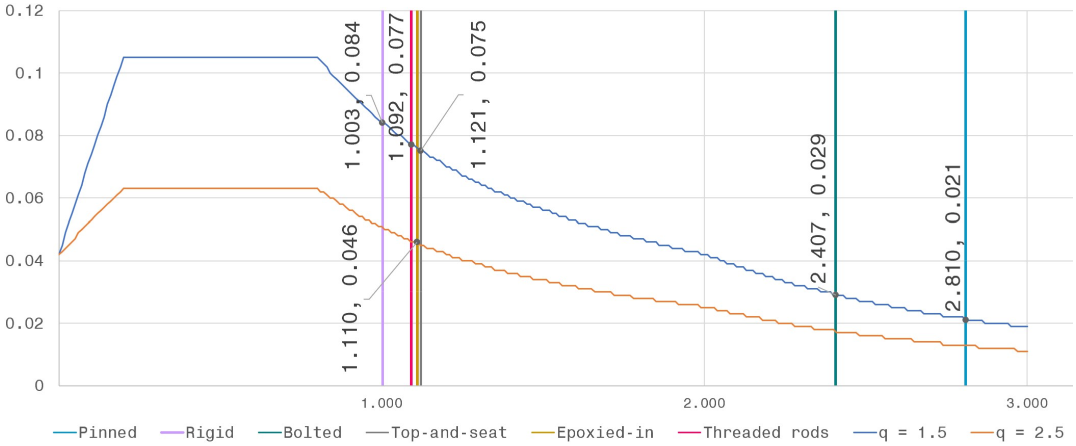

(b) First torsional modes plotted in type 1 spectrum (High seismicity area).

Figure 6.3: Comparison of first torsional modes plotted in type 2 and type 1 response spectrum.

EC8-1 Annex A suggests using a displacement-based spectrum instead of acceleration-based for buildings with long vibration periods, where the Type 1 elastic acceleration design spectrum (S_e) is converted to an elastic *displacement* spectrum (S_{De}):

$$S_{De}(T) = S_e(T)\left[\frac{T}{2\pi}\right]^2 \tag{6.2}$$

6.2.2 Interstory drift

The interstory drifts found for all cases are significantly inside the limits from EC8-1 seen in Table 4.16. This was expected, as the building satisfies requirements from EC8-1 NA.3.2.1(5) allowing seismic analysis to be omitted:

- The building is located where the ground type is A-E and the design ground acceleration satisfy the formula $a_g \leq 0.3\text{m/s}^2$
- The design spectrum satisfies $S_d \leq 0.50\text{m/s}^2$ with behaviour factor $q \leq 1.5$, no stiffness reduction and conservative assumption for the ground (Figure 4.13a)

In addition, based on the modal analysis where the influential modes are presented for each connection-case, the first periods range from 1.18 s (rigid) to 2.81 s (pinned). This corresponds to a frequency range from 0.85 Hz to 0.35 Hz. Based on Figure 6.4 from Holmes (2007), the reference building, with moment-resting timber frames, CLT core, and HCS as flooring, moves closer to the wind-sensitive area than the earthquake domain when the stiffness of the connections decrease.

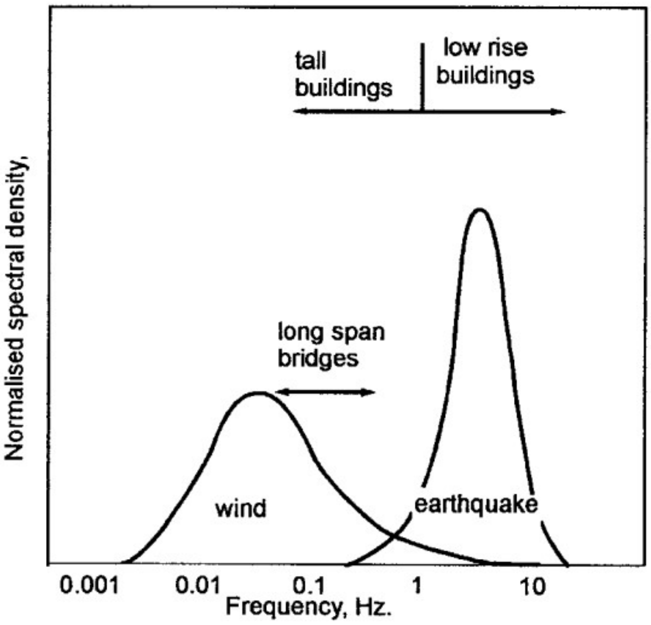

Figure 6.4: Normalized frequency domain of buildings, showing wind-sensitive buildings and earthquake prone range (Holmes, 2007). Logarithmic frequency axis.

6.3 Beam-to-column connections

An evaluation of all connections used for the analysis, the method of calculating the rotational stiffness, and model implementation is necessary. Some advantages and disadvantages of all presented connections with comparison are presented, and the reuse potential of the structural components in each connection is assessed.

6.3.1 Bolted connection

The bolted connection is a commonly used beam-to-column connection with the potential for many variations. The presented geometry of the connection is based on continuous columns with slotted in steel plates and M16 bolts based on the connection by Zhou et al. (2021). This design immediately provides restrictions for the seismic analysis, as the maximum diameter for steel bolts or dowels in EC5 is 12 mm for the connection to be considered energy dissipating. This restriction can be avoided using a high member thickness. A calculation of connection failure mode using cross-sections from this thesis, according to EC5 Eq. (3.80), shows failure in the bolt. This indicates that a behavior factor higher than 1.5 may be used, presumably leading to structural drifts closer to Epoxied-in (Figure 5.19), and was also expected as EC8-1 8.3(4) allows increasing the behavior factor if member thickness is greater than $8 \cdot d$.

The method of calculating the rotational stiffness for this connection is based on EC5 formulation. The radius of gyration for the bolts is based on a symmetrically placed rotation point (COR in Figure 4.7). This may be an appropriate approximation for a centrally/internally placed column with beams in all directions. For side columns, the change in rotation point may be of significance. This change was chosen not to be considered because the number of bolts in the column is significantly higher than the number of bolts in the beam.

The main advantage of the bolted connection is the fast and easy assembly on-site. Steel plates and timber elements can be produced off-site with high precision and ready-for-assemblage. Few components are involved in both the production and assemblage, reducing unexpected errors. This leads to a low amount of man hours necessary when assembling.

The slotted-in steel plates can be more complicated to assemble for a four-way column of large cross-sectional dimensions.. However, good alternatives exist, such as T-stub connectors presented by Salem and Petrycki (2016), shown in Figure 6.5. This removes the problem with intersecting steel plates inside the column, and the same assumptions on rotational stiffness can be made as the T-stub showed no sign of displacement during experimental testing (Salem and Petrycki, 2016).

(a) Connection of T-stub to GLT column. **(b)** T-stub with beam bolted.

Figure 6.5: Bolted connection with T-stub steel connector by Salem and Petrycki (2016).

The reuse potential is high for the column as few components change the structural properties. The beams have to be checked for embedding in the timber from the bolts. This is due to several factors, including the non-linear behavior under initial loads caused by imperfections described by Reynolds et al. (2013). This occurs even for tightly fitted dowels, meaning that this can also be applied for bolts, based on dowels and bolts being treated equally in EC5 when it comes to rotational stiffness. For timber beams with significant embedding in the bolt holes, it may be unsafe to reuse the connection. Parts of the beam with bolt holes should be removed, and down-cycling of removed part must be done. As the bolted connection used in the analysis is designed for failure in connecting elements, the bolts should not be reused. Alternatively, an epoxy resin can be inserted into the holes. The consequences of this should be investigated with numerical and experimental tests.

6.3.2 Top-and-seat steel angles connection

The Top-and-seat steel angles connection (TaS) is an alternative to the traditional bolted connection presented by Zhou et al. (2021). The connection is designed to offer significant rotational stiffness through bolts and steel angles located at the top and the bottom of the beam.

The method of calculating the rotational stiffness in this thesis is based on several researchers, as presented in Section 4.3.2, and only the rotational spring is implemented at the beam ends in the numerical model. The experimental results from Zhou et al. (2021) showed significant lateral displacements, and including this effect may lead to more accurate results. The reasoning behind no lateral springs is based on the assumption that the slab provides lateral stiffness between the spans, and to get comparable results.

The main advantages of TaS are similar to the bolted. Fast and easy on-site assemblage and the low amount of man hours necessary to assemble, due to the possibility for large amounts of preparation done off-site. The connection provides high rotational stiffness, but this is dependent on the stiffness of the column face. Increasing this through reinforcing self-tapping screws perpendicular to grain (Rebouças et al., 2022) can increase the rotational stiffness. A simple horizontal shear capacity calculation of the beam according to EC5 showed failure mode (L) from Figure 3.25, which implies unwanted failure in the wood.

As the connection is based on bolts, disassembling the connection should be relatively easy. The reuse potential for the column in this connection is affected by several things. The holes from the bolts may be embedded from shear gravity loads transferred from the beam. The holes also reduce the flexibility of reusing columns in other projects where story height, beam dimensions, and bolts are different.

The possibility of using epoxy resin or other filling material leads to a potential of regaining the original compressive capacity, but the tensile stress in external columns caused by horizontal loadings should be controlled using the reduced cross-sectional area. The more extensive (and less aesthetic) process of applying FRP to the columns may be a more appropriate way of securing structural integrity, as Raongjant and Jing (2020) found sprayed FRP retrofitted damaged columns to reach up to 98% of its original ultimate bearing capacity.

The reuse potential of the beam and connecting elements for TaS is assumed equal to the bolted case. This is based on the possibility of embedding. It may be theoretically possible to reuse the bolts. However, as the experimental results from Zhou et al. (2021) showed bending of bolts in the beam, this must be evaluated in detail for the relevant beam and column dimensions. This connection is also regarded as the least aesthetic connection based on the visible bottom steel angle. The steel also makes the connection more vulnerable to fire (Rebouças et al., 2022). Bolts connect the steel angles through the cross-section of the columns. As the dimensions of BX and BY are equal, the shanks might intersect. This can be avoided by replacing the bottom bolts with screwed-in rods, inspired by the connection from Kasal et al. (2014), seen in Figure 6.6. The rotational stiffness must then be revised in detail and recalculated.

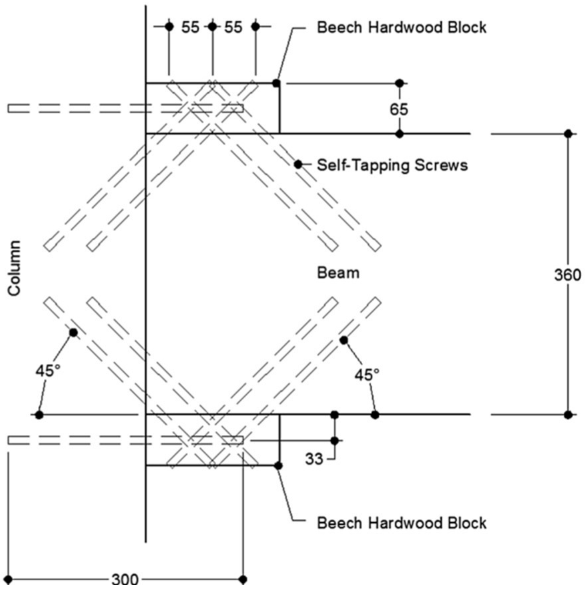

Figure 6.6: Connection with screws from Kasal et al. (2014) reducing the problem of intersecting fasteners in column.

6.3.3 Epoxied-in steel rods connection

The Epoxied-in (or glued-in) connection (Ep-in) is adapted to appropriate dimensions from Fairweather (1992) and designed for ductile failure of the glued-in steel rods.

The connection provides high rotational stiffness, and the rotational spring stiffness $K_{\theta.con}$ is based on elongation of rods, shear stiffness of the epoxy resin and column-face in addition to beam- and column-face compressive stiffness. The face compressive stiffnesses are critical parts, especially in the column. Based on this, the assemblage is considered time-consuming and requires high precision on-site to ensure a tight fit between column and beam. The margin of tolerance both in production and during mounting must be minimized to ensure a tight fit for all parts of the building. This requires a higher amount of man hours.

This connection is, in addition, prone to shear forces from gravity loads, as the transfer of loads is done by the steel rods. This creates tension perpendicular to grain in the beam, which reduces the load-bearing capacity. This implies that this connection should be carefully implemented, especially for buildings with long spans and large gravity forces.

Disassembling this connection without damaging elements is evaluated to be practically impossible based on the rods being glued-in, both in the beam and the column. This will presumably lead to downcycling all parts within 400 mm off the column. Rebouças et al. (2022) claim that the uncontrollable state of the rods and epoxy is a disadvantage of this connection. Some known advantages of this connection are that it can offer fire resistance by the protection of the steel rods from the timber (Rebouças et al., 2022). Furthermore, the visible steel is limited to an absolute minimum.

6.3.4 Inclined threaded rods with steel rings connection

The Inclined Threaded Rods with steel rings connection is adapted from Stamatopoulos et al. (2022) and designed to provide high rotational stiffness to moment resisting timber frames. Experimental results showed no measurable slip (Stamatopoulos et al., 2022), creating immediate stiffness to the structure, in contradiction to what typically is the case for dowel connections (Reynolds et al., 2014). The inclination of the rods is used to exploit the strength of timber parallel to grain compared to perpendicular to grain. The main advantage of this connection is that it can be designed to provide high rotational stiffness, even for small dimensions of structural elements.

The numerical implementation of the connection is done through a rotational spring. The spring stiffness is found using the analytical formulation presented by Stamatopoulos et al. (2022) with the appropriate element dimensions. No detailed research was found regarding the lateral stiffness of this connection, but Vilguts et al. (2021) found through a preliminary parametric study that a rigid constraint for lateral movement resulted in negligible differences compared to lateral releases when using reasonable values for linear spring constants.

The inclined rods are also an important factor in assessing on-site assemblage. The amount of off-site preparation is crucial for reducing man hours and, most importantly, ensuring the correct rotational stiffness. The change of inclination angle of rods in columns showed a significant change in rotational stiffness (Stamatopoulos et al., 2022), and preparation of elements should be done by a CNC machine, not manually. This introduces the possibility of delivering the beams and columns with prethreaded rods to the construction site, leaving only connecting the elements through the steel rings to on-site work.

The failure modes of rods experiencing tensile stress when the beam is subjected to gravity loads were investigated using the forces and transformation matrix in Eq. (3.63). The failure modes typically showed rod failure in long steel rods, while shorter rods failed in withdrawal. The experimental results showed cracking of the timber due to tensile forces, but Adam and Salem (2020) showed enhancement of this property by inserting reinforcing self-tapping screws. The steel rod lengths are determined by geometric properties of the beams and columns, leading to 4-way connections being possible. The behavior and rotational stiffness when some elements are not perfectly orthogonal to one another must be reviewed.

If the off-site preparation is done as described, the disassembly of the connection is done by loosing the bolts inside the steel rings, which is relatively simple. The limitation of reusing elements is due to the rods and the holes for rod insertion. This limits the reuse potential significantly for buildings like the reference building, with large variations in element lengths and not a rectangular, modular-based geometry. Based on this, the reuse potential of structural elements is considered low, and the connecting elements should not be reused as the entire load transfer is the done through these.

6.3.5 Overview of connections

An overview and summarization of the presented connections, with the ease of assembly, disassembly, and reuse potential, is given in Table 6.3. Based on the results from the MRSA, where all connection cases are inside the limits set by EC8, and the discussion, it can be read that the traditional bolted connection offers the highest amount of flexibility and potential for reusing structural components.

More complex connections generally offer higher rotational stiffness by working around the weak properties of timber with regards to tension and compression perpendicular to grain. The consequences are that this can reduce the reuse potential of all structural elements through the need for holes, glue, or high precision placement and increases the man hours related to assembling and disassembling the connection.

From the discussion of the modal analysis and the modal response spectrum analysis, it can be read that further investigation is necessary to guarantee that the bolted connection offers a satisfactory resistant building structure when evaluated for dynamic wind loads and displacement based design spectrum. This is due to the first mode being a torsional mode for connections classified as pinned according to EC3.

Table 6.3: Summarization and overview of connections with comments based on the discussion.

		Ease of assemblage		**Ease of demountability**	**Reuse potential**		
Connection	**Rotational stiffness [kNm/rad]**	**Man hours**	**High precision necessary on-site**		**Column**	**Beam**	**Connecting element**
Bolted	5 629.0	Low	No, pre-drilled holes	High	High	Possible, dependant on embedding	Low
Top-and-seat steel angles	49 960.7 26 683.8 30 190.9	Low	No, pre-drilled holes	High	Possible	Possible, dependant on embedding	Low
Epoxied-in steel rods	53 480.8 33 938.0 50 741.5 38 669.1	High	Yes, thight fit between column- and beam-face to provide rotational stiffness	Low	Low	Possible with length reduction	Low
Inclined threaded rods with steel rings	51 606.0 58 705.4 54 970.0	Dependant on off-site preparation	Yes, but can be reduced significantly	High	Low for different geometry	Low for different geometry	Low

6.4 Hollow core slab and detailing

The use of HCS and the numerical model is discussed in this part to highlight aspects affecting the results and possible sources of error, leading to unrealistic behavior of the building. To ensure that the method of designing a building presented in this thesis is possible, a proposal regarding connection of HCS to a timber frame system is described.

6.4.1 Numerical modeling of slab

The slab is modeled as a thin shell with default material quality concrete C45/55 from SAP2000 (CSI, 2021). As the slab is supposed to represent a HCS, the bending thickness is reduced by a factor of 0.92, following the formulation from Jendzelovsky and Vrablova (2015). The transverse bending modification factor is set to 0.01 to represent the hinged formulation from Lundgren et al. (2004). The preliminary choice of element dimensions was based on diagrams from BEF (2011a), and was controlled, as seen in Appendix A. For the Spectrum Analysis it is assumed that the slab works as a rigid diaphragm. The pre-tension of tendons used in HCS are not included in the model since this was outside the focus of this thesis. Consequently, the stiffness of the building may be underestimated, leading to higher natural periods of the building than what, in reality, is the case. One method to include this could be through a layered model, as done by Feng et al. (2021). The comparison from Jendzelovsky and Vrablova (2015) of numerical models with detailed and simplified models showed that the reduced section modification is not accurate for the natural frequency of the slab. However, for static loading, it shows satisfactory results. As the scope of the dynamic analysis is to investigate the effect of different timber connections, this proved to be a good solution.

6.4.2 Connecting concrete slabs to timber frame

The numerical modeling of the connection from slab to frame is done as pinned connections by releasing bending moments and twisting on all edges. This means that only lateral forces are transmitted from the slab to the beams. In reality, these connections may also transfer moment and torsion, depending on the connection. As connecting HCS to timber beams needs to be further investigated, a proposal is based on the connection of HCS to a flanged steel profile from Buettner et al. (1998) and Brynhildsen et al. (2008).

6.4.2.1 Proposal of connecting hollow core slab to glulam beam

The proposal of connecting HCS to GLT beam can be seen in 3D in Figure 6.7 and 2D in Figure 6.8. It is conceptually designed to transfer horizontal forces acting on the structure, from the HCS to GLT beam, through glued-in rods in the beam and steel hoops. Some research regarding timber-concrete composite (TCC) beams is available, and as this build-up requires on-site casted concrete in selected channels of the HCS, information may be of large value for this proposal.

Ogrin and Hozjan (2021) present several types of connections used for TCC, where dowel connections are categorized as ductile and glued connections as brittle. This means that in addition to checking that the glued-in rods can transfer all critical loads, the properties and dimensions of the glued-in steel rods must ensure ductile failure. Brittle failure of the beam perpendicular to grain caused by transverse horizontal loadings can be the governing load case for deciding beam dimensions. If the rods can transfer loads as designed, a behavior similar to the steel beam in a parametric study by Lam et al. (2000) is expected. This study showed the potential of increasing the bending strength of the beam by 130%. As the shear studs in their study were welded to the beam, this potential is probably not reachable when using glued-in rods, but as the beams in this thesis are preliminarily designed with 70% ULS capacity, the beam dimensions can be reduced.

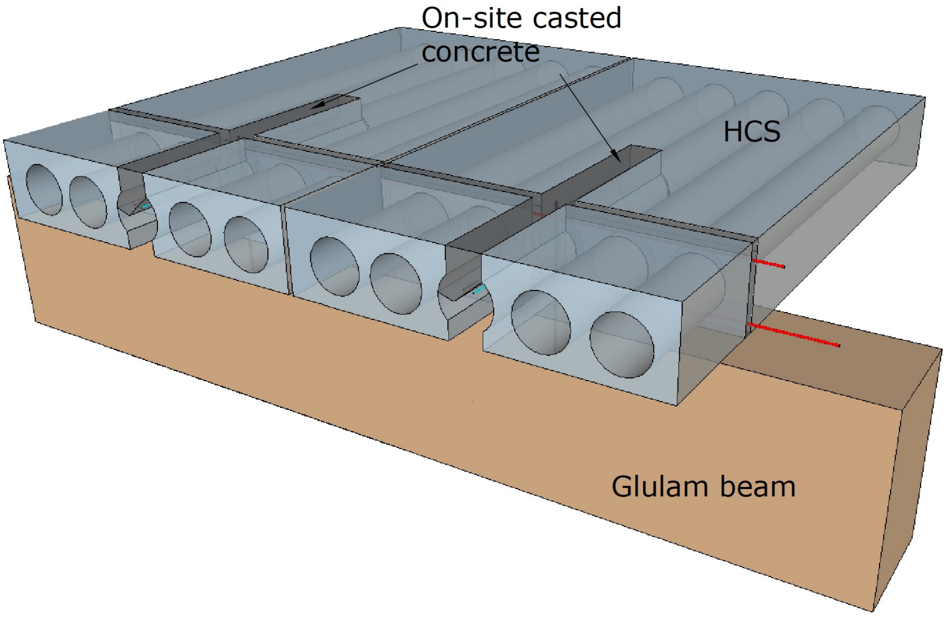

Figure 6.7: 3D view of proposed conceptual design for connection of HCS to a timber frame.

The reusability of this type of connection needs discussion because not only does the on-site casted concrete affect the HCS, but future reuse of the elements is comprehensive, as described by several authors (Naber, 2012; Reppe, 2021; Volkov, 2019). In

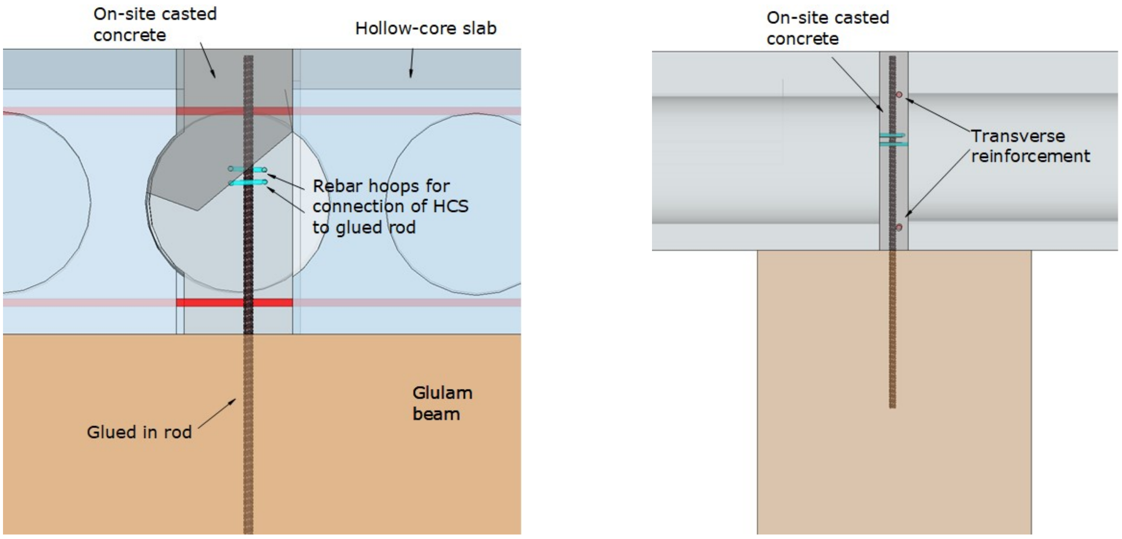

(a) Front view. **(b)** Side view.

Figure 6.8: Details of proposed conceptual design for connection of HCS to a timber frame.

addition, it also lowers the reuse potential of the GLT beam. A thin cover between the beam and the HCS can reduce the amount of damage to the timber elements. Reusability and flexibility of the beams are reduced significantly due to the glued-in rods. This means that this connection can be applicable and valuable for combining reused HCS with timber frames but does not facilitate future reuse of structural components.

6.4.3 Interconnection of slabs

In this thesis, the interconnection of slabs is assumed not to transfer bending moment or torsion. In addition to the reduced transverse bending modification factor, the edges of slabs in each bay are set not to transfer any torsion or bending moment in both the longitudinal and transverse direction to ensure simply-supported behavior of the slab. *Auto-edge constraint* (CSI, 2021) was removed to avoid the slabs transferring bending moment between slabs from different bays. When applying auto-edge constraints, the natural periods decreased by approximately 10%, compared to the results presented in this thesis.

The lack of interconnection in the slab is also visible by investigating the mesh in Figure 4.6a and the discontinuities. These are caused by the *auto-edge constraint* not being active. The areas where the mesh size differs from the maximum size are caused by the shell not being a 4-joint element, as described in section 4.3. This could be avoided by splitting all shells to ensure only 4-joints, but a mesh sensitivity analysis showed no considerable change in the behavior and results.

To simplify future reusability of HCS, Volkov (2019) presents a conceptual design of interconnection between the HCS units seen in Figure 3.26. This concept enables disassembling of units through bolts, but the on-site process is quite demanding. To investigate the behavior of a building where this concept is applied, it should be experimentally examined if the joint can be considered continuous in plan as done in this thesis, or if the link should be regarded as a series of linear springs. Depending on the transverse distance between the bolts, the moment resistance should also be investigated, potentially increasing the transverse bending modification factor considered as hinged in this thesis.

The beam clamp connection proposed by Al-Ghalib and Ghailan (2020) is an applicable solution when using flanged steel profiles, as the clamp teeth need a steel part to connect to. This solution is not possible when using rectangular sections without modification. An alternative could be to screw steel plates to the beam, which could work as a flange. Nevertheless, this system should solely be considered a reasonable solution when producing new elements as installing steel channels requires extra handling of the HCS-units.

7. Conclusions

Based on the results and the discussion of the analyzed reference building with a centrally placed CLT core, moment resisting timber frames, and hollow core slabs as flooring, the following conclusions can be made:

- Higher rotational stiffness of beam-to-column connections shifts the first torsional mode from a lower to higher frequency mode of the building. If the rotational stiffness is classified as semi-rigid according to EC3, the number of considered modes to reach a cumulative mass participation ratio of 90% in each global main direction may, in some cases, include only one torsional mode.
- The lower period modes of the building can lead to the building ending up in a range where the seismic design loads increase significantly. For low-seismicity areas, this will not create critical displacements or drift of the building.
- For connection with lower rotational stiffness, the first mode of the building is torsional, creating unwanted and unpredictable structural behavior. The effect of higher frequency torsional modes must also be regarded in order to achieve a cumulative mass participation ratio of 90% in each global main direction.
- The traditional bolted connection offers high arrangement flexibility, low on-site assemblage time, low disassembly time, and good reusability potential of structural elements. The connection can also be designed as energy dissipating, with a large variation in rotational stiffness, depending on the arrangement and size of the bolts.
- The potential for future reuse of structural elements in timber connections decreases with the increase of connection-complexity, and complex connections require additional man hours and higher precision to fully utilize their potential.
- The seismic performance of the examined building when located in low-seismicity areas satisfy the limits given by the European Standard with regards to element capacity and interstory drift.

8. Future work

In order to continue the research on this topic, the following ideas for future work are presented:

- An analysis of the dynamic behavior from SLS loading should be conducted. As seismic loading is an ALS load case, investigations regarding SLS loadings is necessary. This should be done with wind loads according to EC1-1-4, investigating the acceleration and displacement limits given by *ISO 10137: Bases for design of structures - Serviceability of buildings and walkways against vibrations* (ISO, 2007).
- Experimental testing of HCS to timber can be utilized to investigate if the connection transfer a considerable amount of moment from the slab, creating torsion in the beam. This be combined with numerical modeling.
- The influence of pre-stressed strands can also be investigated through a parametric analysis, varying the dimension, pre-stressing force and number of strands in each HCS unit.
- A detailed Life-Cycle analysis, evaluating the CO_2 reduction of the analyzed building compared to the reference building

References

Ψυχάρης, Γ. Ν. (2016). *ΣΗΜΕΙΩΣΕΙΣ ΑΝΤΙΣΕΙΣΜΙΚΗΣ ΤΕΧΝΟΛΟΓΙΑΣ ΤΕΥΧΟΣ 1*. ΕΜΠ.

Adam, P. and Salem, O. " (Oct. 2020). Structural Integrity of Bolted Glulam Frame Connections Reinforced with Self-Tapping Screws in a Column Removal Scenario. *Journal of Structural Engineering* 146 (10): 04020213. DOI: 10.1061/(ASCE)ST.1943-541X.0002792.

Adesina, A. (2020). Recent advances in the concrete industry to reduce its carbon dioxide emissions. *Environmental Challenges* 1. DOI: 10.1016/J.ENVC.2020.100004.

Aicher, S. and Tapia, C. (2018). Novel internally LVL-reinforced glued laminated timber beams with large holes. DOI: 10.1016/j.conbuildmat.2018.02.178.

Ajdukiewicz, A., Brol, J., Dawczynski, S., and Adamczyk, K. (2013). Reuse of RC and PC precast members as contribution to sustainable construction. In: *fib Symposium TEL-AVIV 2013: Engineering a Concrete Future: Technology, Modeling and Construction, Proceedings*.

Alden, A. (2016). “Reverse, Strike-Slip, Oblique, and Normal Faults.” URL: https://www.thoughtco.com/fault-types-with-diagrams-3879102. *ThoughtCo. Date Accesed: (28/01/2022)*.

Autoretur (2019). Miljø rapport 2019: Slik blir stålet fra norske vrakbiler til armeringsjern. URL: https://autoretur.no/wp-content/uploads/2020/05/Layout_Milj%C3%B8rapport-2019.pdf.

Awad, V., Giresini, L., Koshihara, M., Puppio, M. L., and Sassu, M. (Mar. 2017). Experimental Analyses and Numerical Models of CLT Shear Walls under Cyclic Loading. In: *Wood in Civil Engineering*: 223–240. DOI: 10.5772/65024.

Bağbanci, M. B. and Bağbanci, Ö. K. (2018). The Dynamic Properties of Historic Timber-Framed Masonry Structures in Bursa, Turkey. *Shock and Vibration* 2018. DOI: 10.1155/2018/3257434.

Ballast, D. K. (2007). *Handbook of Construction Tolerances*. 2nd ed. Hoboken, New Jersey: John Wiley & Sons.

Bathe, K. J. (1996). *Finite Element Procedures*. Prentice Hall.

Bathe, K.-J. (2008). Finite Element Method. In: *Wiley Encyclopedia of Computer Science and Engineering*. John Wiley & Sons, Ltd: 1–12. DOI: https://doi.org/10.1002/9780470050118.ecse159.

BEF (2011a). Bind A - Bygging med betongelementer. In: *Betongelementboken*. Oslo: ISBN 82-991880-5-9.

BEF (2011b). Bind H - Dimensjonering for jordskjelv. In: *Betongelementboken*. Oslo: ISBN 82-991880-5-9.

BEF. “Montasje av hulldekker.” URL: https://www.betongelement.no/siteassets/dokumenter/montasje-av-hulldekke-bef-2018.pptx. *Betongelementforeningen. Date Accessed: (02/02/2022)*.

Bernardi, P., Cerioni, R., Leurini, F., and Michelini, E. (Sept. 2016). A design method for the prediction of load distribution in hollow-core floors. *Engineering Structures* 123: 473–481. DOI: `10.1016/J.ENGSTRUCT.2016.06.008`.

Blaß, H. J. and Schädle, P. (2011). Ductility aspects of reinforced and non-reinforced timber joints. *Engineering Structures* 33: 3018–3026. DOI: `10.1016/j.engstruct.2011.02.001`.

Bleuel, D. (2019). *A decision support model for analysing the reuse potential of hollow-core slab floor components*. Tech. rep. (Master thesis) TU Delft. URL: `http://resolver.tudelft.nl/uuid:c34728d8-153c-43aa-8286-0a51a1f768c6`.

Boti, M. F., Cerbu, C., and Shi, H. (2018). Study on the reduction of the general / overall torsion on multi-story, rectangular, reinforced concrete structures. *3rd China-Romania Science and Technology Seminar (CRSTS 2018)*. DOI: `10.1088/1757-899X/399/1/012005`.

Brynhildsen, T., Rotheim, M., Hvidsten, F., Solberg, K., Reiersen, J. E., Myhre, K., and Sygnestveit, A. K. (2008). Hulldekker på bæresystemer av stål. In: Norsk Stålforbund & Betongelementforeningen.

Buchanan, A. H. and Fairweather, R. H. (Feb. 1993). Seismic design of glulam structures. *Bulletin of the New Zealand Society for Earthquake Engineering* 26: 415–436. DOI: `10.5459/bnzsee.26.4.415-436`.

Buettner, D. R., Becker, R. J., Saccoman, J. E., Beerbower, J., Markle, E., Boyle, K., Markle, J., Butler, J., Nimmer, M. J., Collavino, L., Richardson, W. C. E., Gregory, J., Rosenstern, K., Hynes, P., Schrooten, W., Kourajian, P., and Stigler, L. (1998). *PCI Manual for the Design of Hollow Core Slabs*. Tech. rep. CPCI.

CEN (2002). *Eurocode 0: Basis of structural design*. Standard Norge, NS-EN 1990:2002+A1:2005+NA:2016.

CEN (2003). *Eurocode 1: Actions on structures - Part 1-3: General actions - Snow loads*. Standard Norge, NS-EN 1991-1-3:2003+A1:2005+NA:2018.

CEN (2004). *Eurocode 8: Design of structures for earthquake resistance - Part 1: General rules, seismic actions and rules for buildings*. Standard Norge, NS-EN 1998-1:2004+A1:2013+NA:2021.

CEN (2005a). *Eurocode 1: Actions on structures - Part 1-4: General actions - Wind actions*. Standard Norge, NS-EN 1991-1-4:2005+NA:2009.

CEN (2005b). *Eurocode 3: Design of steel structures - Part 1-8: Design of joints*. Standard Norge, NS-EN 1993-1-8:2005+NA:2009.

CEN (2009). *Eurocode 1: Actions on structures - Part 1-1: General actions - Densities, self-weight, imposed loads for buildings*. Standard Norge, NS-EN 1991-1-1:2002+NA:2019.

CEN (2014). *Eurocode 2: Design of concrete structures - Part 1-1: General rules and rules for buildings*. Standard Norge, NS-EN 1992-1-1:2004+A1:2014+NA:2021.

Chang, J., Buchanan, A., Dhakal, R., and Moss, P. (2006). *Simple method for modelling hollowcore concrete slabs under fire*. Tech. rep. University of Canterbury: Departement of Civil Engineering. URL: `https://hdl.handle.net/10092/17651`.

Chopra, A. K. (2012). *Dynamics Of Structures: Theory and applications to earthquake engineering*. 4th ed. Pearson/Prentice Hall.

Cook, R. D., Malkus, D. S., and Plesha, M. E. (2002). *Concepts and application of finite element analysis*. Ed. by W. Anderson. 4th. Hoboken: John Wiley & Sons.

Crocetti, R., Kliger, R., Hansson, E. F., Danielsson, H., Mårtensson, A., Piazza, M., and Serano, E. (2015). *Limtreboka*. Ed. by K. Bell. Vol. 2.

CSI (2004). *Linear and Nonlinear Static and Dynamic Analysis and Design of Three-Dimensional Structures: Basic analysis reference manual*. 9th ed. Berkeley, California: Computers and Structures Inc.

CSI. (2021). "SAP2000 V23 1.0."

de Castilho, V. C., Nicoletti, M. d. C., and El Debs, M. K. (Nov. 2005). An investigation of the use of three selection-based genetic algorithm families when minimizing the production cost of hollow core slabs. *Computer Methods in Applied Mechanics and Engineering* 194 (45-47): 4651–4667. DOI: `10.1016/j.cma.2004.12.008`.

de Silva, C. W. (June 2005). *Vibration and Shock Handbook*. Ed. by C. W. de Silva. CRC Press. DOI: `10.1201/9781420039894`.

Dugdale, J. (2015). *Timber vs. Steel Bridge Superstructure Construction A Simplified Structural, Economic and Environmental Analysis*. UVM Honors College Senior Theses. URL: `https://scholarworks.uvm.edu/hcoltheses/88?utm_source=scholarworks.uvm.edu%2Fhcoltheses%2F88&utm_medium=PDF&utm_campaign=PDFCoverPages`.

Eberhardt, C. L. M., Birgisdóttir, H., and Birkved, M. (2018). Life cycle assessment of a Danish office building designed for disassembly. DOI: `10.1080/09613218.2018.1517458`.

Efterklang. (2021). "A Working Lab, Gothenburg." URL: `https://efterklang.org/projects/a-working-lab-gothenburg/`. *Date accessed: (09/02/2022)*.

Engström et al. (2008). *Structural connections for precast concrete buildings*. Tech. rep. FIB. URL: `https://www.afgc.asso.fr/app/uploads/2010/07/fib_Bull43_NMG.pdf`.

Fairweather, R. H. (1992). *Beam Column Connections for Multi-storey Timber Buildings A Report*. Tech. rep.

Feidaki, E. and Vasdravellis, G. (Sept. 2017). Push out tests of a novel shear connection mechanism for use in demountable precast composite beams. *Eurosteel 2017* 1 (2-3): 2060–2069. DOI: `10.1002/cepa.251`.

Feng, D. C., Xiong, C. Z., Brunesi, E., Parisi, F., and Wu, G. (Jan. 2021). Numerical simulation and parametric analysis of precast concrete beam-slab assembly based on layered shell elements. *Buildings* 11 (1): 1–15. DOI: `10.3390/buildings11010007`.

Ferdous, W., Bai, Y., Ngo, T. D., Manalo, A., and Mendis, P. (Mar. 2019). New advancements, challenges and opportunities of multi-storey modular buildings – A state-of-the-art review. *Engineering Structures* 183: 883–893. DOI: `10.1016/J.ENGSTRUCT.2019.01.061`.

Flores, F. X., Charney, F., and Lopez-Garcia, D. (Jan. 2017). P-Delta effects in the torsional response of structures. *16th World Concerence on Earthquake Engineering 16WCEE 2017*.

Follesa, M., Christovasilis, I. P., Vassallo, D., Fragiacomo, M., and Ceccotti, A. (2013). Seismic design of multi-storey cross laminated timber buildings according to Eurocode 8. *Ingegneria Sismica* 4.

Frenette, C. D. (1997). *The Seismic Response of a Timber Frame with Dowel Type Connections*. Tech. rep. The University of British Columbia: Department of Civil Engineering.

Fugleseth, M., Dahlstrøm, O., Skullestad, J. L., and Borg, A. (Apr. 2020). *Kartlegging av klimagassberegninger for bygg og anlegg i Oslo*. Tech. rep. Oslo kommune Klimaetaten. URL: `https://www.klimaoslo.no/wp-content/uploads/sites/88/2020/09/Kartlegging-av-klimagassberegninger-for-bygg-og-anlegg-i-Oslo_endelig.pdf`.

Gallo, P. Q., Carradine, D. M., and Ramiro Bazaez, ·. (2021). State of the art and practice of seismic-resistant hybrid timber structures. *European Journal of Wood and Wood Products* 79: 5–28. DOI: `10.1007/s00107-020-01556-3`.

Al-Ghalib, A. A. and Ghailan, D. B. (Dec. 2020). Design for Deconstruction: Futuristic Sustainable Solution for Structural Design. *Civil Engineering Beyond Limits* 2 (1): 6–11. DOI: `10.36937/cebel.2021.001.002`.

Ghayeb, H. H., Razak, H. A., and Sulong, N. H. (Jan. 2020). Evaluation of the CO2 emissions of an innovative composite precast concrete structure building frame. *Journal of Cleaner Production* 242: 118567. DOI: `10.1016/J.JCLEPRO.2019.118567`.

Habibullah, A. (2021). "Home - SAP2000 - Computers and Structures, Inc. - Technical Knowledge Base." URL: `https://wiki.csiamerica.com/display/sap2000/Home`.

Hasslacher group. (2021). "Glued Laminated Timber." URL: `https://www.hasslacher.com/data/_dateimanager/broschuere/HNT-Brettschichtholz-EN.pdf`. *HNT PF Brettschichtholz BSH EN. Date Accessed: (31/01/2022).*

Holmes, J. (2007). *Wind Loading of Structures*. 2nd. Taylor & Francis.

Høydahl, V. V. and Walter, H. K. (2020). *Ombruk av byggematerialer og-produkter i et baerekraftperspektiv*. (Master thesis) Norwegian University of Science and Technology. URL: `https://hdl.handle.net/11250/2738114`.

Hradil, P. (Jan. 2014). *Barriers and opportunities of structural elements re-use.*

Hussein, G., Eid, N., and Khaled, H. (Jan. 2020). Torsional Behavior of Irregular Structures during Earthquakes: 40–55. DOI: `10.9790/1684-1605044055`.

Huuhka, S., Kaasalainen, T., Hakanen, J. H., and Lahdensivu, J. (Aug. 2015). Reusing concrete panels from buildings for building: Potential in Finnish 1970s mass housing. *Resources, Conservation and Recycling* 101: 105–121. DOI: `10.1016/J.RESCONREC.2015.05.017`.

Iacovidou, E. and Purnell, P. (July 2016). Mining the physical infrastructure: Opportunities, barriers and interventions in promoting structural components reuse. *Science of The Total Environment* 557-558: 791–807. DOI: `10.1016/J.SCITOTENV.2016.03.098`.

ISO (2007). *ISO 10137: Bases for design of structures - Serviceability of buildings and walkways against vibrations*. 2nd ed. ISO 10137:2007.

Issa, C. A. and Kmeid, Z. (2005). Advanced wood engineering: glulam beams. *Construction and Building Materials* 19 (2): 99–106. DOI: `https://doi.org/10.1016/j.conbuildmat.2004.05.013`.

Jendzelovsky, N. and Vrablova, K. (June 2015). Comparison of Natural Frequencies of Hollow Core Slabs. *Applied Mechanics and Materials* 769: 225–228. DOI: `10.4028/www.scientific.net/amm.769.225`.

Jensen, K. G. and Sommer, J. (2018). *Building a Circular Future*. 3rd ed. Vol. 2.

Joensuu, T., Leino, R., Heinonen, J., and Saari, A. (2022). Developing Buildings' Life Cycle Assessment in Circular Economy-Comparing methods for assessing carbon footprint of reusable components. *Sustainable Cities and Society* 77: 103499. DOI: `10.1016/J.SCS.2021.103499`.

Jorissen, A. and Fragiacomo, M. (2011). General notes on ductility in timber structures. *Engineering Structures* 33 (11). DOI: `10.1016/j.engstruct.2011.07.024`.

Karagiannis, V., Málaga-Chuquitaype, C., and Elghazouli, A. Y. (Jan. 2017). Behaviour of hybrid timber beam-to-tubular steel column moment connections. *Engineering Structures* 131: 243–263. DOI: `10.1016/J.ENGSTRUCT.2016.11.006`.

Kasal, B., Guindos, P., Polocoser, T., Heiduschke, A., Urushadze, S., and Pospisil, S. (Dec. 2014). Heavy Laminated Timber Frames with Rigid Three-Dimensional Beam-to-Column Connections. *Journal of Performance of Constructed Facilities* 28 (6): A4014014. DOI: `10.1061/(ASCE)CF.1943-5509.0000594`.

Lam, D., Elliott, K. S., and Nethercot, D. A. (2000). Parametric study on composite steel beams with precast concrete hollow core floor slabs. *Journal of Constructional Steel Research* 54: 283–304.

Lawson, R. M., Ogden, R. G., and Bergin, R. (June 2012). Application of Modular Construction in High-Rise Buildings. *Journal of Architectural Engineering* 18 (2): 148–154. DOI: `10.1061/(asce)ae.1943-5568.0000057`.

Lindeburg, M. R. and McMullin, K. M. (2014). *Seismic Design of Building Structures: A Professional's Introduction to Earthquake Forces and Design Details*. 11th. Published Works by SJSU Honorees.

Lundgren, K., Broo, H., and Engström, B. (2004). Analyses of hollow core floors subjected to shear and torsion. *Structural Concrete* 5 (4): 161–172. DOI: `10.1680/stco.2004.5.4.161`.

Mahdavifar, V., Barbosa, A. R., and Sinha, A. (2016). Nonlinear layered moddeling approach for cross laminated timber panels subjected to out-of-plane loading. *Sustainability and Innovation for the Future*.

Málaga-Chuquitaype, C. and Elghazouli, A. Y. (Oct. 2010). Component-based mechanical models for blind-bolted angle connections. *Engineering Structures* 32 (10): 3048–3067. DOI: `10.1016/J.ENGSTRUCT.2010.05.024`.

Marzaleh, A. S., Nerbano, S., Croce, A. S., and Steiger, R. (Oct. 2018). OSB sheathed light-frame timber shear walls with strong anchorage subjected to vertical load, bending moment, and monotonic lateral load. *Engineering Structures* 173: 787–799. DOI: `10.1016/J.ENGSTRUCT.2018.05.044`.

Memari, A. and Ramaji, I. J. (2013). Identification of structural issues in design and construction of multi-story modular buildings.

Morino, S. (Apr. 1998). Recent developments in hybrid structures in Japan—research, design and construction. *Engineering Structures* 20 (4-6): 336–346. DOI: `10.1016/S0141-0296(97)00022-9`.

Moustafa, S. E. (1981). Effectiveness of Shear-Friction Reinforcement in Shear Diaphragm Capacity of Hollow-Core Slabs.

Moynihan, M. C. and Allwood, J. M. (Aug. 2014). Viability and performance of demountable composite connectors. *Journal of Constructional Steel Research* 99: 47–56. DOI: `10.1016/J.JCSR.2014.03.008`.

Naber, N. (2012). *Reuse of hollow core slabs from office buildings to residential buildings*. (Master thesis) TU Delft. URL: `http://resolver.tudelft.nl/uuid:a04416b7-e8c0-499d-81c7-48c51b5e7fda`.

Niu, Y., Rasi, K., Hughes, M., Halme, M., and Fink, G. (2021). Prolonging life cycles of construction materials and combating climate change by cascading: The case of reusing timber in Finland. *Resources, Conservation and Recycling* 170. DOI: `10.1016/j.resconrec.2021.105555`.

NOBI Voss. (2016). "Hulldekketyper, tverrsnittsdata." URL: `https://www.nobi.no/wp/wp-content/uploads/2016/01/Tverrsnitt-Hulldekke-NOBI.pdf`. *Date Accessed: (15/02/2022)*.

Ogrin, A. and Hozjan, T. (2021). Timber-Concrete Composite Structural Elements. In: *Engineered Wood Products for Construction*. Ed. by M. Gong. Rijeka: IntechOpen: Ch. 14. DOI: `10.5772/intechopen.99624`.

Okada, T., Kobori, H., Kojima, Y., Suzuki, S., Nishikido, K., Hirose, A., and Takahashi, K. (Jan. 2020). Evaluating the durability of structural glulam bonded with aqueous polymer-isocyanate adhesive by two kinds of accelerated aging treatments. *European Journal of Wood and Wood Products* 78 (1): 113–122. URL: https://eurekamag.com/research/070/984/070984758.php.

Ondrej and Guzman, T. (2017). "Meshing FAQ." URL: https://wiki.csiamerica.com/display/kb/Meshing+FAQ. *Computers and Structures, Inc. - Technical Knowledge Base. Date Accessed: (04/05/2022).*

Pan, Y., Tannert, T., Kaushik, K., Xiong, H., and Ventura, C. E. (2021). Seismic performance of a proposed wood-concrete hybrid system for high-rise buildings. *Engineering Structures* 238: 112194. DOI: https://doi.org/10.1016/j.engstruct.2021.112194.

Peretti, G., Druhmann, C. K., Bleiziffer, S., Brown, J., Campama Pizarro, M., Del Río Merino, R., Gremmelspacher, M., Kontovourkis, J., Nenonen, O., Purs, S., and Villoria Sáez, I. (2019). Working Group Three Report: Regenerative Construction and Operation. *RESTORE - REthinking Sustainability TOwards Regenerative Economy*.

Pitilakis, K., Riga, E., Anastasiadis, A., and Makra, K. (2015). New Elastic Spectra, Site Amplification Factors and Aggravation Factors for Complex Subsurface Geology, Towards the Improvement of Ec8. In: *6th International Conference on Earthquake Geotechnical Engineering*.

Polastri, A. and Pozza, L. (2016). Proposal for a standardized design and modeling procedure of tall CLT buildings. *International Journal for Quality Research* 10 (3): 607–624. DOI: 10.18421/IJQR10.03-12.

Porcu, M. (Jan. 2017). Ductile Behavior of Timber Structures under Strong Dynamic Loads. In: 24. DOI: 10.5772/65894.

Raongjant, W. and Jing, M. (2020). Comparison experimental study on retrofitting methods of partially damaged timber columns. In: *Materials Science Forum*. Vol. 976 MSF. Trans Tech Publications Ltd: 173–179. DOI: 10.4028/www.scientific.net/MSF.976.173.

Rebouças, A., Mehdipour, Z., Branco, J., and Lourenco, P. (Mar. 2022). Ductile Moment-Resisting Timber Connections: A Review. *Buildings* 12. DOI: 10.3390/buildings12020240.

Reppe, I. S. (2021). *Ombruk av betongelementer: Analyse av marked, barrierer, muligheter og potensiale for klimagassreduksjon ved ombruk av hulldekker fra Regjeringskvartalet*. (Master thesis) Norwegian University of Life Sciences. URL: https://hdl.handle.net/11250/2787600.

Reynolds, T., Harris, R., and Chang, W.-S. (2013). In-service dynamic stiffness of dowel-type connections. DOI: 10.13140/2.1.3606.3045.

Reynolds, T., Harris, R., and Chang, W.-S. (2014). Stiffness of dowel-type timber connections under pre-yield oscillating loads. DOI: 10.1016/j.engstruct.2014.01.024.

Romani, M. and Blaß, H. J. (2001). *Design model for FRP reinforced glulam beams*. Tech. rep. Venice, Italy: International Council for Research, Innovation in Building, and Concstruction.

Rose, C. M. and Stegemann, J. A. (2018). From Waste Management to Component Management in the Construction Industry. *Sustainability*. DOI: 10.3390/su10010229.

Salem, S. and Petrycki, A. (Aug. 2016). *Experimental Testing of Wood-Steel-Wood Moment-resisting Bolted Connections*.

Sandoli, A., D'Ambra, C., Ceraldi, C., Calderoni, B., and Prota, A. (2021). "Sustainable cross-laminated timber structures in a seismic area: Overview and future trends." *Applied Sciences (Switzerland)*.

Al-Shaarbaf, I. A., Al-Azzawi, A., and Abdulsattar, R. (Jan. 2018). A state of the art review on hollow core slabs. *ARPN Journal of Engineering and Applied Sciences* 13: 3240–3245.

Stamatopoulos, H., Malo, K. A., and Vilguts, A. (Mar. 2022). Moment-resisting beam-to-column timber connections with inclined threaded rods: Structural concept and analysis by use of the component method. *Construction and Building Materials* 322: 126481. DOI: `10.1016/J.CONBUILDMAT.2022.126481`.

Tesfamariam, S. and Stiemer, S. F. (Dec. 2014). Special Issue on Performance of Timber and Hybrid Structures. *Journal of Performance of Constructed Facilities* 28 (6): A2014001. DOI: `10.1061/(ASCE)CF.1943-5509.0000641`.

Think Wood. (2020). "Demonstrating the viability of mass wood structures." URL: `https://www.thinkwood.com/projects/brock-commons-tallwood-house`. *Brock Commons Tallwood House. Date Accesed: (08/02/2022).*

Tomasi, R., Zandonini, R., Piazza, M., and Andreolli, M. (Aug. 2008). Ductile End Connections for Glulam Beams. *Structural Engineering International* 18: 290–296. DOI: `10.2749/101686608785096595`.

Tsalkatidis, T., Amara, Y., Embaye, S., and Nathan, E. (2018). Numerical investigation of bolted hybrid steel-timber connections. *Frontiers in Built Environment* 4. DOI: `10.3389/FBUIL.2018.00048/FULL`.

Vahedian, A., Shrestha, R., and Crews, K. (May 2019). Experimental and analytical investigation on CFRP strengthened glulam laminated timber beams: Full-scale experiments. *Composites Part B: Engineering* 164: 377–389. DOI: `10.1016/j.compositesb.2018.12.007`.

Velamati, S. (2012). *Feasability, benefits and challenges of modular construction in high rise development in the United States: A developer's perspective*. (Bachelor of Science, Economics) University of Pennsylvania. URL: `https://dspace.mit.edu/bitstream/handle/1721.1/77129/825120099-MIT.pdf?sequence=2&isAllowed=y`.

Vilguts, A., Stamatopoulos, H., and Malo, K. A. (Feb. 2021). Parametric analyses and feasibility study of moment-resisting timber frames under service load. *Engineering Structures* 228: 111583. DOI: `10.1016/J.ENGSTRUCT.2020.111583`.

Volkov, M. (2019). *Structural connections in circular concrete*. (Master thesis) TU Delft. URL: `http://resolver.tudelft.nl/uuid:41bd0462-cac9-4314-9682-06962df42e52`.

Vratuša, S., Kitek Kuzman, M., and Kilar, V. (2011). Structural particulars of glued laminated beams of variable height. *Drewno : prace naukowe, doniesienia, komunikaty* vol. 54, nr 185: 19–38.

Whittaker, M. J., Grigoriadis, K., Soutsos, M., Sha, W., Klinge, A., Paganoni, S., Casado, M., Brander, L., Mousavi, M., Scullin, M., Correia, R., Zerbi, T., Staiano, G., Merli, I., Ingrosso, I., Attanasio, A., and Largo, A. (2019). Novel construction and demolition waste (CDW) treatment and uses to maximize reuse and recycling. DOI: `10.1080/17512549.2019.1702586`.

Wilson, E. L., Der Kiureghian, A., and Bayo, E. P. (Jan. 1981). A replacement for the srss method in seismic analysis. *Earthquake Engineering & Structural Dynamics* 9 (2): 187–192. DOI: `https://doi.org/10.1002/eqe.4290090207`.

Yang, H., Liu, W., and Ren, X. (May 2016). A component method for moment-resistant glulam beam–column connections with glued-in steel rods. *Engineering Structures* 115: 42–54. DOI: `10.1016/J.ENGSTRUCT.2016.02.024`.

Yasumura, M., Kobayashi, K., Okabe, M., Miyake, T., and Matsumoto, K. (Apr. 2016). Full-Scale Tests and Numerical Analysis of Low-Rise CLT Structures under Lateral Loading. *Journal of Structural Engineering* 142 (4): E4015007. DOI: `10.1061/(ASCE)ST.1943-541X.0001348`.

Zhao, X., Zhang, B., Kilpatrick, T., Sanderson, I., and Liu, D. (Aug. 2021). Numerical Analysis on Global Serviceability Behaviours of Tall Glulam Frame Buildings to the Eurocodes and

UK National Annexes. *Journal of Civil Engineering and Construction* 10 (3): 109–122. DOI: `10.32732/jcec.2021.10.3.109`.

Zhou, Q., Gong, M., Chui, Y. H., and Mohammad, M. (Aug. 2014). Measurement of rolling shear modulus and strength of cross laminated timber fabricated with black spruce. *Construction and Building Materials* 64: 379–386. DOI: `10.1016/J.CONBUILDMAT.2014.04.039`.

Zhou, S. R., Li, Z. Y., Feng, S. Y., Zhu, H., and Kang, S. B. (July 2021). Effects of bolted connections on behaviour of timber frames under combined vertical and lateral loads. *Construction and Building Materials* 293: 123542. DOI: `10.1016/J.CONBUILDMAT.2021.123542`.

Appendix A. Control of HCS capacity

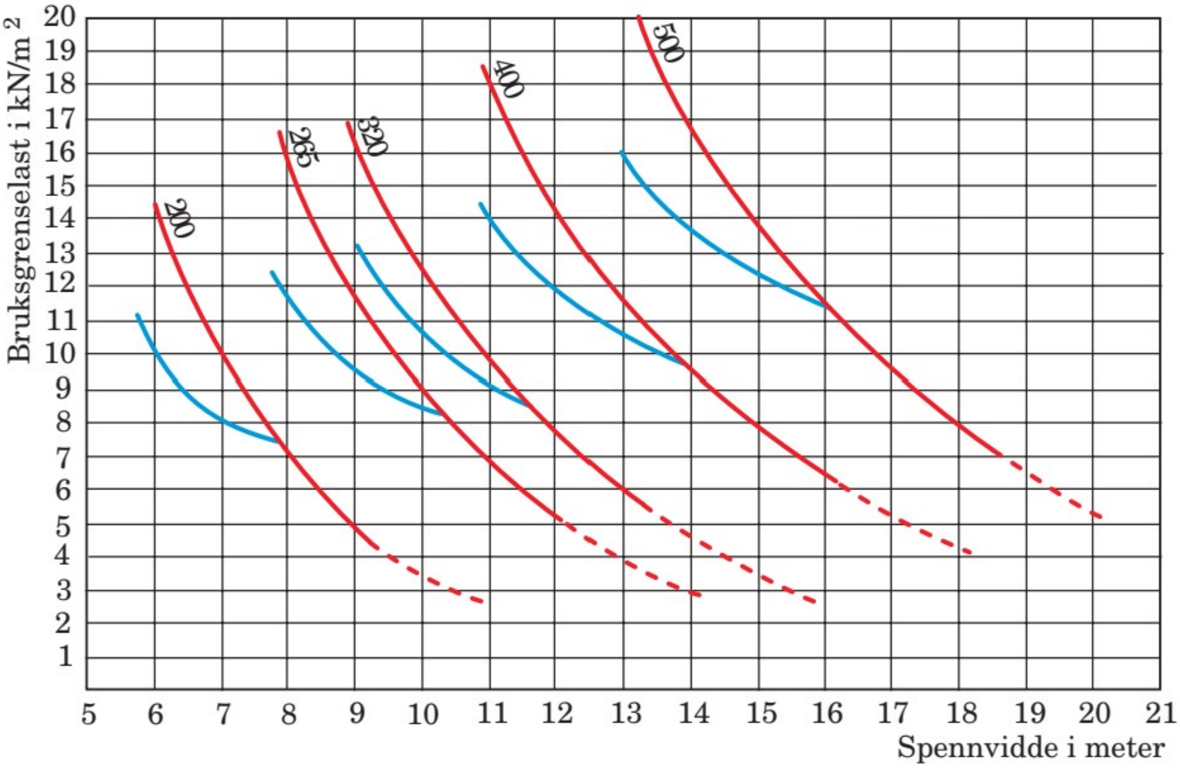

Figure A.1: Preliminary design capacity curves for HCS (BEF, 2011a) (in Norwegian, vertical axis: SLS load [kN/m^2], horizontal axis: Span length [m]).

Indoor HCS

Element dimensions

$B := 1.2\ m$

$h := 200\ mm$

Loads: $l_s := 8.4\ m$

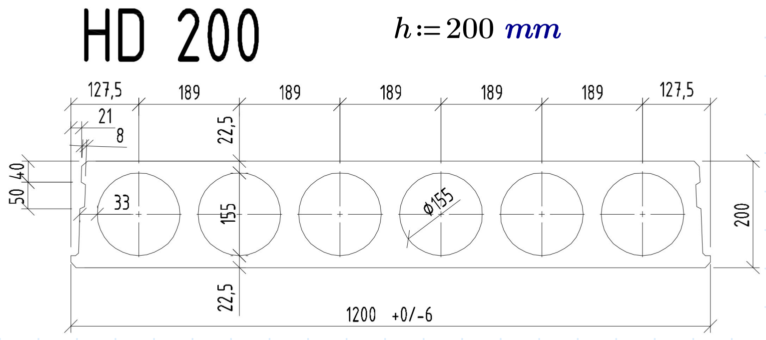

$G_{HD200} := 255\ \frac{kg}{m^2}$

$G_{void} := 16\ \frac{kg}{m^2}$

$G_{flooring} := 1.5\ \frac{kN}{m^2}$

$Q_{cat.B} := 3\ \frac{kN}{m^2}$

$$q_{f.in} := 1.2 \cdot \left(\left(G_{HD200} + G_{void}\right) \cdot g + G_{flooring}\right) + 1.5 \cdot \left(Q_{cat.B}\right) = 9.489\ \frac{kN}{m^2}$$

Simply supported:

$$M_{f.in} := \frac{\left(q_{f.in} \cdot B \cdot {l_s}^2\right)}{8} = 100.433\ kN \cdot m$$

Assuming standard reincforcement depth for strands $a := 40\ mm$

Distance from compressive edge to reinforcement $d := h - a = 160\ mm$

Full utilization of compressive zone, lever arm: $z := 0.835 \cdot d = 133.6\ mm$

$\varnothing_{strand} := 12.7\ mm$ Area of strand $A_p := 100\ mm^2$

Yield force at 0.2 $F_{0.2} := 170\ kN$ $\gamma_s := 1.25$ $f_s := \frac{1700\ MPa}{\gamma_s} = 1360\ MPa$

Tensile capacity:

$$F_{sd} := \frac{F_{0.2}}{\gamma_s} = 136\ kN$$

Necessary number of strands $n_{in} := \left(\frac{M_{f.in}}{f_s \cdot z \cdot A_p}\right) = 5.528$

$n_{in.NOBI} := 7$ $S_{d.in} := n_{in.NOBI} \cdot F_{sd} = 952\ kN$

$M_{d.in} := S_{d.in} \cdot z = 127.187\ kN \cdot m$

$$\left.\begin{array}{l} \text{if } M_{d.in} > M_{f.in} \\ \quad \Vert \text{“OK”} \\ \text{else} \\ \quad \Vert \text{“Not OK”} \end{array}\right| = \text{“OK”}$$

Outdoor HCS

Loads: $l_s := 8.4\ m$

Element dimensions

$B := 1.2\ m$

$h := 320\ mm$

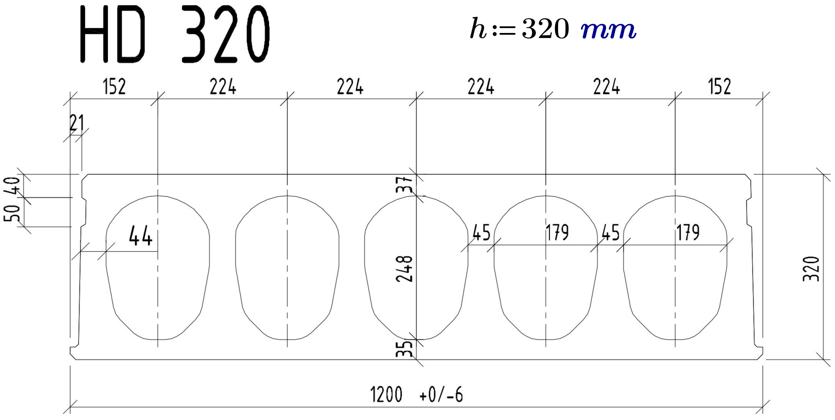

$$G_{HD320} := 400\ \frac{kg}{m^2}$$

$$G_{void} := 25\ \frac{kg}{m^2}$$

$$G_{sedum} := 5\ \frac{kN}{m^2}$$

$$Q_{cat.I} := 3\ \frac{kN}{m^2}$$

$$Q_{snow} := 2.8\ \frac{kN}{m^2}$$

$$q_{f.out} := 1.2 \cdot \left(G_{HD320} + G_{void}\right) \cdot g + G_{sedum} + 1.5 \cdot \left(Q_{cat.I}\right) + 1.05 \cdot Q_{snow} = 17.441\ \frac{kN}{m^2}$$

Simply supported:

$$M_{f.out} := \frac{\left(q_{f.out} \cdot B \cdot l_s^{\ 2}\right)}{8} = 184.6\ kN \cdot m$$

Assuming standard reincforcement depth for strands $a := 40\ mm$

Distance from compressive edge to reinforcement $d := h - a = 280\ mm$

Full utilization of compressive zone, lever arm: $z := 0.835 \cdot d = 233.8\ mm$

$ø_{strand} := 12.7\ mm$ Area of strand $A_p := 100\ mm^2$

Yield force at 0.2 $F_{0.2} := 170\ kN$ $\gamma_s := 1.25$ $f_s := \frac{1700\ MPa}{\gamma_s} = 1360\ MPa$

Tensile capacity:

$$F_{sd} := \frac{F_{0.2}}{\gamma_s} = 136\ kN$$

Necessary number of strands $n_{out} := \left(\frac{M_{f.out}}{f_s \cdot z \cdot A_p}\right) = 5.806$

$n_{out.NOBI} := 7$ $S_{d.out} := n_{out.NOBI} \cdot F_{sd} = 952\ kN$

$M_{d.out} := S_{d.out} \cdot z = 222.578\ kN \cdot m$

if $M_{d.out} > M_{f.out}$ = "OK"
  "OK"
else
  "Not OK"

Norges miljø- og biovitenskapelige universitet
Noregs miljø- og biovitskapelege universitet
Norwegian University of Life Sciences

Postboks 5003
NO-1432 Ås
Norway